

# DISSERTATION

submitted to the

Combined Faculties for the Natural Sciences and for Mathematics  
of the Ruperto-Carola University of Heidelberg, Germany

for the degree of

Doctor of Natural Sciences

Put forward by

Dipl. Phys. Fabian Manuel Bergermann

Born in Stuttgart

Oral examination: November 30, 2016



# MASSIVELY PARALLELIZED STED NANOSCOPY

## REFEREES:

Prof. Dr. Stefan W. Hell

Prof. Dr. Rainer H. A. Fink



## ABSTRACT

---

Fluorescence microscopy constitutes a key method for the virtually non-invasive study of biological structures and processes on a sub-cellular scale. Stimulated Emission Depletion (STED) nanoscopy extends fluorescence imaging to nanometer resolutions. However, this method usually acquires an image by scanning small pixels in a sequential manner, which can lead to long acquisition times of several minutes. This limits the feasibility of many large-scale superresolution experiments, because faster acquisition times imply sacrificing either highest resolution, a good signal-to-noise ratio or a large image size. To unleash the full spatio-temporal resolving power potential of STED nanoscopy on a large imaging region, massively parallelized acquisition is therefore inevitable.

In this thesis, I develop a comprehensive and quantitative description of parallelized STED and validate the derived findings by means of two experimental implementations. Investigating the key technical parameters and their interplay reveals the possibility of reducing the laser power by up to three orders of magnitude below the value required for serially acquiring STED systems. This eliminates a major bottleneck of previously reported attempts to parallelize STED nanoscopy, limiting them to tiny image sizes or inferior resolutions. Moreover, using a rather simple optical arrangement, I was able to enlarge the superresolved image area to 33  $\mu\text{m}$  edge length (roughly the dimensions of a small cell), featuring a resolution down to 30 nm and a 13 000-fold degree of parallelization. While the implementations presented here should be viewed as prototypes, they prove the technical feasibility of massively parallelized STED nanoscopy. The methods developed in this thesis in combination with suitable high-speed detectors bring video-rate STED nanoscopy of whole cells within reach.

## ZUSAMMENFASSUNG

---

Fluoreszenzmikroskopie ist eine Schlüssel­methode zur minimal-invasiven Untersuchung subzellulärer biologischer Strukturen und Prozesse. Die sogenannte Stimulated Emission Depletion (STED) Nanoskopie erweitert das Auflösungsvermögen bis hinein in den Nanometerbereich. Typischerweise wird dabei die Probe Pixel für Pixel abgetastet. Dieser sequentielle Scanprozess kann allerdings zu Bildgestehungszeiten von mehreren Minuten führen und den Einsatz im großen Maßstab erschweren. Um kürzere Aufnahmezeiten zu ermöglichen, muss entweder Auflösungsqualität, Signal-zu-Rausch-Verhältnis oder Bildgröße geopfert werden. Für die Anwendung von STED mit höchster räumlicher und zeitlicher Auflösung auf einer großen Bildfläche führt deshalb kein Weg an Parallelisierung vorbei.

Diese Arbeit bietet eine umfassende, quantitative Darstellung der Theorie parallelisierten STEDs und überprüft die wichtigsten Ergebnisse mithilfe zweier experimenteller Mikroskopieaufbauten. Die Analyse der zentralen Parameter und deren Zusammenwirken zeigt, dass im Vergleich zur sequentiellen STED Variante eine um bis zu drei Größenordnungen geringere Laserleistung notwendig ist. Dies ist insofern wichtig, als bisher publizierte Versuche STED zu parallelisieren aufgrund unzureichender Laserleistungen in Bildfeld und Auflösung stark eingeschränkt waren. In der vorliegenden Arbeit konnte mit einem sogar vergleichsweise einfachen optischen Aufbau eine Auflösung von bis zu 30 nm und eine 13 000-fache Parallelisierung auf einem Bildfeld von 33  $\mu\text{m}$  Kantenlänge erzielt werden. Das entspricht der Größe einer kleinen Zelle. Trotz ihres prototypischen Charakters beweisen die in dieser Arbeit vorgestellten optischen Aufbauten, dass eine hochgradige Parallelisierung der STED-Nanoskopie möglich ist. Mit der in naher Zukunft zu erwartenden Verfügbarkeit von Kameras mit entsprechend hoher Aufnahmegeschwindigkeit rücken Videos lebender Zellen in STED-Auflösungsqualität in greifbare Nähe.

# CONTENTS

---

<b>PREFACE</b>	<b>1</b>
<b>1 INTRODUCTION</b>	<b>3</b>
<b>I FROM BASIC PRINCIPLES TO PARALLELIZED STED</b>	<b>7</b>
<b>2 THEORY OF LIGHT WAVE PROPAGATION</b>	<b>9</b>
2.1 Maxwell equations, solution and implications . . . . .	9
2.2 Plane wave decomposition . . . . .	11
2.2.1 Discussion . . . . .	12
2.2.2 PWD and the resolution limit . . . . .	13
2.3 Wave propagation in the spatial domain . . . . .	15
2.3.1 Huygens' Principle . . . . .	15
2.3.2 Discussion . . . . .	15
<b>3 GEOMETRIC PRINCIPLES OF OPTICAL MICROSCOPY</b>	<b>17</b>
3.1 Overview . . . . .	17
3.2 Diffraction limit . . . . .	18
3.3 Sine condition . . . . .	19
3.4 Intensity law . . . . .	20
3.5 Polarization effects . . . . .	21
3.6 Discussion . . . . .	22
<b>4 FOCUS FIELD IN HIGH-APERTURE MICROSCOPY</b>	<b>23</b>
4.1 Problem definition . . . . .	23
4.2 Solution in spherical coordinates . . . . .	24
4.3 Integration in the principal plane . . . . .	24
4.4 Approximations in focus field calculations . . . . .	25
4.5 Discussion . . . . .	26
4.5.1 The Airy-pattern in high-NA microscopy . . . . .	26
4.5.2 Interpretation of the "obliquity factor" . . . . .	27
<b>5 STED NANOSCOPY</b>	<b>29</b>
5.1 Concepts of STED nanoscopy . . . . .	29
5.2 Resolution scaling in STED nanoscopy . . . . .	30
5.3 Resolution formula for single-point STED . . . . .	31
5.4 Resolution formula for parallelized STED . . . . .	32
5.5 Efficiency comparison of both variants . . . . .	33
5.6 Discussion . . . . .	34
<b>II EXPERIMENTAL IMPLEMENTATION AND RESULTS</b>	<b>37</b>
<b>6 PARALLELIZATION VIA INTERFEROMETRIC FRINGES</b>	<b>39</b>
6.1 Interferometric fringe pattern . . . . .	39
6.2 Setup components . . . . .	40
6.3 Scanning strategy . . . . .	41
6.4 Experimental control . . . . .	42
6.5 Image assembly . . . . .	42

6.5.1	Linear regression versus mask . . . . .	43
6.5.2	Fluorescence signal crosstalk . . . . .	43
6.5.3	Estimation of the fringe period and its phase . .	44
6.5.4	Bleaching correction . . . . .	45
6.5.5	Background subtraction . . . . .	46
6.5.6	De-shearing . . . . .	46
6.6	Results . . . . .	46
6.6.1	Sub-30 nm resolution . . . . .	47
6.6.2	Dual-color imaging on a large field of view . .	48
6.6.3	Sub-70 nm resolution in cellular sample . . . . .	49
6.7	Discussion . . . . .	50
6.7.1	Resolution and field of view . . . . .	50
6.7.2	Polarization bias . . . . .	50
6.7.3	STED efficiency . . . . .	50
6.7.4	Recording speed and gating . . . . .	51
7	PARALLELIZATION BY A DIFFRACTIVE OPTICAL ELEMENT	53
7.1	Motivation and overview . . . . .	53
7.2	Setup components . . . . .	53
7.3	Scanner . . . . .	55
7.4	Measures for improved robustness . . . . .	55
7.5	Results . . . . .	57
7.5.1	Parallelized STED with more than 10 000 zeros	57
7.5.2	30 nm resolution on a large field of view . . . . .	57
7.5.3	Dual-color cell structure imaging . . . . .	58
7.6	Discussion . . . . .	59
7.6.1	100-fold faster image acquisition . . . . .	59
7.6.2	Square-root resolution scaling reconfirmed . . .	59
7.6.3	Energy efficiency advantage validated . . . . .	60
8	CONCLUSION AND OUTLOOK	61
	APPENDIX	65
A	PUBLICATIONS AND CONTRIBUTIONS	67
B	NUMERICAL CONSIDERATIONS AND SAMPLING	69
C	RANGE OF VALIDITY OF THE DEBYE APPROXIMATION	71
D	CODE FOR FOCUS FIELD CALCULATIONS	73
E	DIFFRACTION AT A BINARY PHASE GRATING	77
	BIBLIOGRAPHY	81
	ACKNOWLEDGMENTS	87

## LIST OF FIGURES

---

Figure 1	Fluorescence imaging schematic . . . . .	3
Figure 2	Jablonski diagram and state switching schematic	4
Figure 3	Comparison of dSTED and pSTED . . . . .	5
Figure 4	Arbitrary and plane wave schematic . . . . .	10
Figure 5	The propagator $\mathcal{P}_{\mathbf{k}_\perp}$ as low-pass filter . . . . .	14
Figure 6	Microscope lens arrangement . . . . .	17
Figure 7	Abbe's resolution limit . . . . .	18
Figure 8	Sine condition schematic . . . . .	20
Figure 9	Geometric interpretation of the sine condition	20
Figure 10	Intensity law and polarization mapping . . . . .	21
Figure 11	Geometric construction of high-NA beam path	22
Figure 12	Variable illustration for focus field calculations	23
Figure 13	Oblique incident Gaussian beam . . . . .	27
Figure 14	Resolution comparison . . . . .	29
Figure 15	Efficiency comparison plot . . . . .	35
Figure 16	Implementation details of pSTED . . . . .	40
Figure 17	Scanning strategy . . . . .	42
Figure 18	Photon crosstalk in next-neighbor zero . . . . .	44
Figure 19	Resolution assessment . . . . .	47
Figure 20	Dual-color imaging . . . . .	48
Figure 21	Imaging in a biological context . . . . .	49
Figure 22	DOE-STED implementation . . . . .	54
Figure 23	Resolution assessment in DOE-STED . . . . .	57
Figure 24	Dual-color cytoskeleton staining . . . . .	59
Figure 25	Square-root law reconfirmed . . . . .	60
Figure 26	Diffraction at a binary grating . . . . .	77
Figure 27	DOE diffraction pattern . . . . .	80

## LISTINGS

---

Listing 1	Implementation of <i>Fast focus field calculations</i> .	73
-----------	--	----

## ACRONYMS

---

STED	Stimulated Emission Depletion
RESOLFT	Reversible Saturable/Switchable Optically Linear (Fluorescence) Transitions.
PALM	Photo-Activated Localization Microscopy
fPALM	Fluorescence Photoactivation Localization Microscopy
STORM	Stochastic Optical Reconstruction Microscopy
TIRF	Total Internal Reflection Fluorescence (microscopy)
NA	Numerical Aperture
PWD	Plane Wave Decomposition
RS <sub>1</sub>	Rayleigh-Sommerfeld diffraction integral no 1
FWHM	Full Width at Half Maximum
dSTED	donut-base single-point-scanning STED
pSTED	parallelized STED
DOE	Diffractive Optical Element
DOE-STED	parallelized STED nanoscopy using a DOE
SWP	Segmented Wave Plate
easySTED	STED with eased alignment using an SWP
CCD	Charge-Coupled Device
emCCD	electron-multiplying CCD
iCCD	intensified CCD
sCMOS	scientific Complementary Metal–Oxide–Semiconductor
SPAD	Single-Photon Avalanche Diode
APD	Avalanche Photodiode
MPI BPC	Max Planck Institute for Biophysical Chemistry
MPL	Max Planck Institute for the Science of Light
DKFZ	Deutsches Krebsforschungszentrum (German Cancer Research Center)

## PREFACE

Physicists love to shatter long-held beliefs.

Once the dust has settled, new thoughts emerge quite naturally and fresh crops can blossom on the field of science. Case in point, not long after it had been suggested [34] and shown [39, 40] that ABBE'S century-old resolution limit [1] for lens-based light microscopy would have to yield to an advanced fluorophore excitation switching scheme, a whole family of similar schemes emerged [8, 21, 35, 36, 53]. Ever since, the newly coined STED nanoscopy and its variants have raised the curtain to reveal unprecedented visual insights into sub-cellular structures and dynamics.

Not for a century, but rather for a decade, the subordinate belief has lingered in the scientific community that STED nanoscopy might be bound to a time consuming sequential point-by-point scanning and acquisition scheme. It is the humble intention of the author to report on the progress to give this belief a little toss as well.



## INTRODUCTION

The light microscope is an ubiquitous tool in the life-sciences as it allows direct visual inspection of cells and tissues. Fluorescence microscopy constitutes a prominent modality to add contrast and specificity to the otherwise almost transparent cellular sample as illustrated in Figure 1. To achieve both contrast and specificity, a fluorescent molecule that emits light in the visible range upon excitation is attached specifically to the target structure using a suitable labeling strategy. The fluorescence photons are filtered spectrally and registered by a detector to yield a target-specific, high-contrast image representation of the fluorophore-decorated structure of interest. Being

*Fluorescence microscopy*

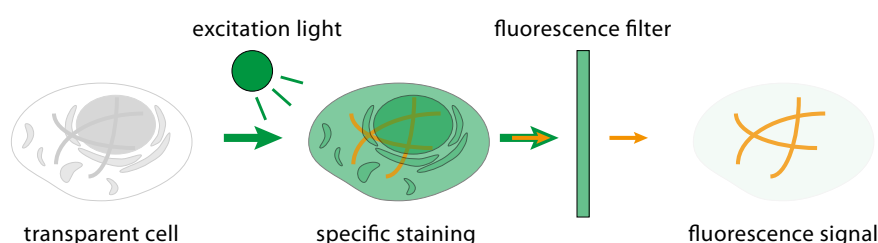


Figure 1: Fluorescence imaging schematic.

a lens-based far-field method, fluorescence microscopy is subject to diffractive blurring in the detection (imaging) path, such that all fluorophores less than 200 nm apart appear as a single blurry spot if they emit photons at the same time. This resolution limit [1], formulated more than a century ago by ERNST ABBE, still holds true as a direct consequence of the wave properties of light.

*Diffraction limit in widefield light microscopy*

Nonetheless, the emerging field of *nanoscopy methods* manages to improve spatial resolution far beyond the diffraction limit by ensuring that close-by fluorescent molecules do not emit light at the same time. These superresolution techniques therefore employ excitation strategies that prepare fluorophores into distinguishable molecular states, for example a fluorescent *ON* state and a dark *OFF* state [30, 31], as exemplified for the case of STED in Figure 2. Switching between the states in a targeted or stochastic fashion allows sequential readout and thus distinction and separation of neighboring molecules [32]. While coordinate-targeted switching and stochastic single-molecule switching methods may differ considerably in many technical aspects, they are two sides of the same coin.

*Superresolution by switching of molecular states*

Stochastic methods including (f)PALM/STORM/GSDIM [8, 21, 35, 53] use a widefield excitation scheme that randomly switches a sparse subset of fluorophores into the *ON*-state. The centroid position of

*Stochastic switching*

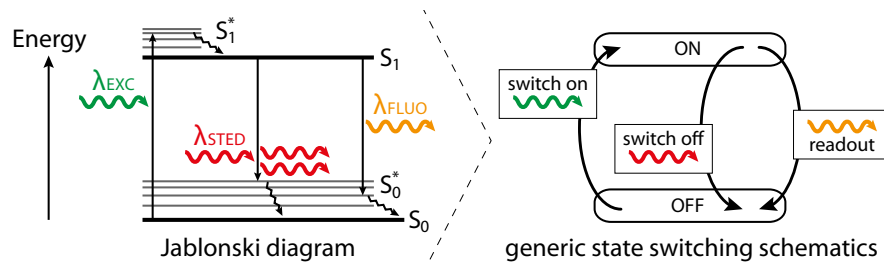


Figure 2: Jablonski diagram of fluorophore state transitions (as discussed in [42]) and corresponding state switching schematic [33] highlighting the generic character of an ON-OFF switching scheme.

these singled-out emitters can be estimated far below the diffractive blur. Repetition of this procedure generates a list of emitter localization coordinates that can be merged to a synthetic high-resolution image. The localization precision depends on the number  $N$  of detected photons per emitter and scales like the inverse square-root of  $N$  [11, 17, 58].

*Coordinate-targeted methods*

Coordinate-targeted approaches of the STED/ RESOLFT [15, 34, 36] family employ a switch-off light field that contains at least one tightly confined area of ideally zero intensity, which reduces the region of allowed fluorescence to a distinct sub-diffraction-sized spot, cf. Figure 3. Scanning of the “zero” across the sample probes the fluorophores sequentially in a controlled, coordinate-targeted fashion. Assignment of all detected fluorescence photons per scanning step to their corresponding pixels gives rise to a superresolved image. The resolution in this case scales like the inverse square-root of the number of photons in the switch-off light field [28].

*Parallelization*

While stochastic single-molecule methods are parallelized by design owing to their widefield detection nature, coordinate-targeted approaches attain parallelization only via a suitably engineered spatial patterning of the state-switching light field. Until now, all commercially available STED nanoscopes use a sequential point-by-point scanning scheme, which can lead to long image acquisition times of up to tens of minutes if a large sample region is recorded. This makes many large-scale superresolution experiments unfeasible, and the observation of dynamic processes in whole living cells virtually impossible. Because the rate of emitted photons is ultimately limited by the fluorescence lifetime, image recording cannot be sped up significantly without sacrificing either field of view [61], signal strength [54] or resolution [7] unless parallel acquisition is introduced.

*Related work*

In 2014, a parallelization of RESOLFT nanoscopy with reversibly switchable fluorescent proteins (RSFPs) attained 50 nm resolution [43]. As switch-off pattern, it used two orthogonally crossed standing light waves, which allows for a tightly packed grid of intensity “zeros” [14]. Typical pixel acquisition times in present RSFP-based RESOLFT implementations are however about one order of magnitude larger than

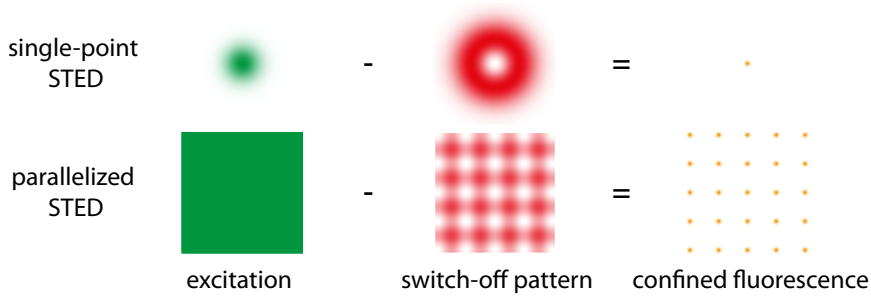


Figure 3: Comparison of single-point and parallelized STED.

for STED (30  $\mu\text{s}$  [23] vs. 300  $\mu\text{s}$  [25, 55]). Because STED nanoscopy has been shown to perform well down to the 20 nm regime with a wide variety of bright and photostable synthetic fluorophores [46, 65], it is still the standard method to achieve the highest spatio-temporal resolution. Its capability to capture highly dynamic processes (e. g. [61]) can be extended to large fields of view by a suitable parallelization strategy. The first parallelized STED design featured four cloned excitation and switch-off beams and four distinct single-pixel detectors [9], but upscaling of the method seems hardly feasible considering implementation complexity and cost. The concept of two orthogonal standing waves that was used to parallelize RESOLFT [14] was recently adopted to attain 100-fold parallelization of STED using a camera as a parallelized detector [66]. The available STED pulse energy limited the resolution to approximately 70 nm and the field of view to less than  $3 \mu\text{m} \times 3 \mu\text{m}$ .

This thesis examines the feasibility, challenges and merits of a massively parallelized STED implementation. In particular, it discusses measures that can reduce the required laser power by more than three orders of magnitude when compared to serial STED implementations. Being the first comprehensive and detailed discussion of the topic, a theory part revisits key aspects of light-field engineering in high-performance microscopy. It is the author's intent to sketch a simple, yet comprehensive and self-contained presentation of the matter. Chapter 2 touches the theory of light propagation. In Chapter 3, key concepts of a high-NA objective lens are presented, followed by a discussion on light field calculations, their numerical implementation and their connection to the Fourier theory in Chapter 4. This background allows a simple, yet complete conceptual derivation of the STED resolution formula in Chapter 5. The important cases of a single-point STED implementation and its parallelized counterpart are discussed separately and then compared on a quantitative level. Chapter 6 presents a first experimental implementation proving that sub-30 nm resolutions and 2000-fold parallelized dual-color imaging are feasible with two orthogonally crossed standing light waves as a parallelized fluorescence inhibition pattern. A considerably simplified redesign is described in Chapter 7. It allows the exploration

*Scope and  
organization of this  
thesis*

of conditions that come closer to the theoretical efficiency limits of this approach to parallelize STED. By these means, it was possible to enlarge the superresolved image area to  $33\ \mu\text{m}$ , featuring a total of 13 000 zeros in parallel. Conclusions and an outlook in Chapter 8 complete this thesis.

## Part I

### FROM BASIC PRINCIPLES TO PARALLELIZED STED NANOSCOPY

The fluorescence-inhibiting pattern used in this work to parallelize STED nanoscopy reveals some pivotal advantages over its single-point scanning counterpart. However, its implications have not yet been reported in full detail in the literature to this date. To put the experimental study conducted here on firm ground and to allow a qualitative as well as a quantitative analysis, Part I of this work introduces the physical principles underlying the optical setup in a self-contained manner. To this end, I start by recapitulating the established theory of wave propagation, with particular focus on polarization effects in Chapter 2. I proceed with a discussion of distinct features of microscopy with high numerical aperture (NA) in Chapter 3. Both are combined to yield a closed-form description of the focal field of high-NA microscopes (Chapter 4). Because the light pattern required to parallelize STED extends over a comparably large size of  $30\ \mu\text{m}$ , the initial formulation goes beyond the usual (Debye) approximations that otherwise restrict the validity of the calculated field to the vicinity of the focal point. It is shown that the approximations still hold for the field size discussed here, which permits returning to a simplified form that allows for a faster calculation and an instructive interpretation of the constituting components. Based on this foundation, the resolution formulae of serial STED and parallelized STED are derived and compared in a simple and conceptual manner in Chapter 5.



*From a long view of the history of mankind – seen from, say, ten thousand years from now – there can be little doubt that the most significant event of the 19th century will be judged as Maxwell’s discovery of the laws of electrodynamics.*

— Richard Feynman

This chapter reviews the theoretical foundation of light wave propagation as a prerequisite for the subsequent chapters. The *Maxwell equations* as the most fundamental equations of classical electrodynamics give rise to a *wave equation* that describes the dynamics of electromagnetic field propagation. A suitable set of solutions to the *wave equation* are the plane waves, which are subject to constraints imposed by the Maxwell equations. Based on these preliminaries, the method of *plane wave decomposition* (PWD) is introduced and its consequences to the diffraction limit are discussed. An equivalent real-space formulation of the PWD is the *Rayleigh-Sommerfeld integral of the first kind* (RS1), from which the quantitative Huygens’ principle will be deduced as basis for the rigorous formulation of light wave propagation in the focus field of high-aperture microscopes.

## 2.1 MAXWELL EQUATIONS, SOLUTION AND IMPLICATIONS

The Maxwell equations within a source-free medium of refractive index  $n$  read [38]:

$$\nabla \cdot \mathbf{E} = 0, \quad (1)$$

$$\nabla \cdot \mathbf{B} = 0, \quad (2)$$

$$\nabla \times \mathbf{E} = -\partial_t \mathbf{B}, \quad (3)$$

$$\nabla \times \mathbf{B} = (n/c)^2 \partial_t \mathbf{E}. \quad (4)$$

The linearity of the differential operators “ $\nabla \cdot$ ” (divergence) and “ $\nabla \times$ ” (curl) in the *Maxwell equations* allows to combine the identities

$$\nabla \times \nabla \times \mathbf{E} = \nabla \nabla \cdot \mathbf{E} - \nabla \cdot \nabla \mathbf{E} = -\Delta \mathbf{E} \quad (5)$$

and

$$\nabla \times \nabla \times \mathbf{E} = \nabla \times (-\partial_t \mathbf{B}) = -\partial_t (\nabla \times \mathbf{B}) = -(n/c)^2 \partial_t^2 \mathbf{E} \quad (6)$$

to the *wave equation*

$$\Delta \mathbf{E}(\mathbf{r}, t) = (n/c)^2 \partial_t^2 \mathbf{E}(\mathbf{r}, t). \quad (7)$$

$\mathbf{E}$  denotes the electric field,  $\mathbf{B}$  the magnetic field.

“ $\nabla$ ” denotes the gradient operator and  $\Delta := (\nabla)^2$  is the Laplacian operator.

Insertion proves that any field of the form  $\mathbf{E}(\mathbf{r}, t) = \mathbf{E}(\mathbf{r} - \mathbf{v} t)$  solves the *wave equation* (7) provided that  $\mathbf{v}^2 = (c/n)^2$ . Because such an electric field  $\mathbf{E}$  travels by design with unchanged shape and uniform velocity  $\mathbf{v}$  (see Figure 4), the constant  $c$  is readily identified with the speed of light in vacuum.

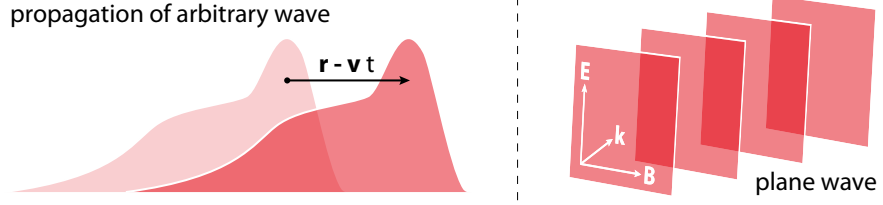


Figure 4: Propagation of an arbitrary wave and plane wave illustration.

A particularly useful set of solutions to the *wave equation* are plane waves of the form

$$\mathbf{E}(\mathbf{r}, t) = \hat{\mathbf{E}} e^{i\mathbf{k} \cdot (\mathbf{r} - \mathbf{v} t)} = \hat{\mathbf{E}} e^{i\mathbf{k} \cdot \mathbf{r} - i\omega t}. \quad (8)$$

Plane waves (illustrated in Figure 4) oscillate in direction of the wave-vector  $\mathbf{k}$  with spatial frequency  $|\mathbf{k}| = k = 2\pi/\lambda_n$  and with angular frequency  $\omega = \mathbf{k} \cdot \mathbf{v}$ .  $\lambda_n = \lambda/n$  is the wavelength in medium of refractive index  $n$  and  $\lambda$  the wavelength in vacuum;  $\hat{\mathbf{E}}$  denotes the complex vector-valued amplitude. Plugging the plane-wave ansatz (8) into the *wave equation* (7) yields the dispersion relation

$$\mathbf{k}^2 = (n/c)^2 \omega^2, \quad (9)$$

which pins down the dependence of the wave vector components on the angular frequency.

The *Maxwell equations* set constraints on the amplitude components  $\hat{\mathbf{E}}$  and  $\hat{\mathbf{B}}$ . The divergence equations (1) and (2) for plane waves:

$$0 = \nabla \cdot \mathbf{E} = \nabla \cdot (\hat{\mathbf{E}} e^{i\mathbf{k} \cdot \mathbf{r} - i\omega t}) = i\mathbf{k} \cdot \mathbf{E} \quad (10)$$

(and similar for the  $\mathbf{B}$ -field) imply

$$\mathbf{k} \cdot \hat{\mathbf{E}} = 0, \quad (11)$$

$$\mathbf{k} \cdot \hat{\mathbf{B}} = 0. \quad (12)$$

Similarly, the curl equation (3)

$$\nabla \times \mathbf{E} = -\partial_t \mathbf{B} \implies i\mathbf{k} \times \mathbf{E} = i\omega \mathbf{B} \quad (13)$$

demands

$$\mathbf{k} \times \hat{\mathbf{E}} = c k \hat{\mathbf{B}}. \quad (14)$$

The amplitude vectors  $\hat{\mathbf{E}}$  and  $\hat{\mathbf{B}}$  along with the wave vector  $\mathbf{k}$  are therefore mutually orthogonal, as illustratively indicated in Figure 4. Furthermore, if  $\hat{\mathbf{E}}$  is known,  $\hat{\mathbf{B}}$  follows from Equation (14) and is thus disregarded in the proceeding discussion.

## 2.2 PLANE WAVE DECOMPOSITION

In a somewhat arbitrary convention the  $z$ -axis is commonly chosen as the principal direction of light propagation. According to the dispersion relation (9),  $k_z$  can be written as a function of the remaining wave-vector components  $\mathbf{k}_\perp := (k_x, k_y)$  and of  $\omega$ :

$$k_z(\mathbf{k}_\perp, \omega) = \sqrt{((n/c)\omega)^2 - \mathbf{k}_\perp^2}. \quad (15)$$

The subscript “ $\perp$ ” will consistently denote both Cartesian vector components that are perpendicular to the respective  $z$ -component. Similarly, the perpendicularity condition for the electric field can be enforced by rewriting Equation (11) as

$$\hat{\mathbf{E}}_z = -\frac{\hat{\mathbf{E}}_\perp \cdot \mathbf{k}_\perp}{k_z} \quad (k_z \neq 0). \quad (16)$$

Hence, the *Maxwell equations* give rise to transverse plane wave solutions which are constrained by conditions (9) and (16) to the form

$$\mathbf{E} = \hat{\mathbf{E}}(\hat{\mathbf{E}}_\perp, \mathbf{k}_\perp, \omega) e^{i(\mathbf{k}_\perp \cdot \mathbf{r}_\perp + k_z(\mathbf{k}_\perp, \omega)z) - i\omega t}. \quad (17)$$

The explicit functional dependencies of the amplitude vector  $\hat{\mathbf{E}}$  and of the  $k_z$ -component that highlight the remaining degrees of freedom will be omitted in the proceeding discussion for the sake of a cleaner notation.

Because the *wave equation* is linear, its general solution is a linear combination of the plane waves in Equation (17). The electric field can hence be written as integral superposition of plane waves:

$$\mathbf{E}(\mathbf{r}, t) = \iint \hat{\mathbf{E}} e^{i(\mathbf{k}_\perp \cdot \mathbf{r}_\perp + k_z z)} d\mathbf{k}_\perp e^{-i\omega t} d\omega. \quad (18)$$

The exponent was already suggestively rearranged to recognize the formal resemblance to the Fourier transform, which shall be defined as

$$\mathcal{F}_\omega[g(\omega)] := \int g(\omega) e^{-i\omega t} d\omega, \quad (19)$$

and the (two-dimensional) inverse Fourier transform as

$$\mathcal{F}_{\mathbf{k}_\perp}[g(\mathbf{k}_\perp)] := \int g(\mathbf{k}_\perp) e^{i\mathbf{k}_\perp \cdot \mathbf{r}_\perp} \frac{d\mathbf{k}_\perp}{(2\pi)^2}, \quad (20)$$

with  $g$  being any square-integrable function. Upon rescaling of  $\hat{\mathbf{E}}$  by  $(2\pi)^2$  to absorb the normalization factor in (20) for sheer convenience, the compact notation of Equation (18) reads

$$\mathbf{E}(\mathbf{r}, t) = \mathcal{F}_\omega[\mathcal{F}_{\mathbf{k}_\perp}[\hat{\mathbf{E}} e^{i k_z z}]]. \quad (21)$$

*The generalization that includes  $k_z < 0$  is discussed in the closing remarks to this section.*

*For  $k_z = 0$ , Equation (11) reduces to  $\hat{\mathbf{E}}_\perp \cdot \mathbf{k}_\perp = 0$  and  $\hat{\mathbf{E}}_z$  remains unconstrained.*

Stationary solution

A stationary solution is obtained by approximating the spectral density with a delta distribution, namely  $\hat{\mathbf{E}} = \hat{\mathbf{E}}(\mathbf{k}_\perp, \omega) \delta(\omega - \omega_0)$  (monochromatic case). The Fourier transform in the angular frequency domain in Equation (18) can be evaluated and gives

$$\mathbf{E}(\mathbf{r}, t) = \mathcal{F}_{\mathbf{k}_\perp}[\hat{\mathbf{E}} e^{i k_z z}] e^{-i \omega_0 t} = \mathbf{E}(\mathbf{r}) e^{-i \omega_0 t}. \quad (22)$$

Hence, the monochromatic field factorizes into an oscillating phase term  $e^{-i \omega_0 t}$ , which contains the time-dependence, and a stationary electric field

$$\mathbf{E}(\mathbf{r}) = \mathcal{F}_{\mathbf{k}_\perp}[\hat{\mathbf{E}} e^{i k_z z}]. \quad (23)$$

Inserting the ansatz (22) into the *wave equation* (7), evaluating its right-hand side and using Equation (9) yields the *Helmholtz equation* for the components of the stationary field

$$\Delta \mathbf{E}(\mathbf{r}) = -k^2 \mathbf{E}(\mathbf{r}). \quad (24)$$

It remains to determine the amplitude components  $\hat{\mathbf{E}}$ . For  $z = 0$  in Equation (23), we identify  $\hat{\mathbf{E}}$  as the (two-dimensional) *forward* Fourier transform of  $\mathbf{E}$ :

$$\hat{\mathbf{E}} = \mathcal{F}_{\mathbf{k}_\perp}[\mathbf{E}(\mathbf{r}_\perp, 0)]. \quad (25)$$

Denoting the propagator term as

$$\mathcal{P}_{\mathbf{k}_\perp}(z) := e^{i k_z z}, \quad (26)$$

the stationary plane wave decomposition (23) can be written as

$$\mathbf{E}(\mathbf{r}_\perp, z) = \mathcal{F}_{\mathbf{k}_\perp}[\mathcal{F}_{\mathbf{r}_\perp}[\mathbf{E}(\mathbf{r}_\perp, 0)] \mathcal{P}_{\mathbf{k}_\perp}(z)], \quad (27)$$

which is the main result of this section.

### 2.2.1 Discussion

**PWD AS BOUNDARY VALUE PROBLEM:** The plane wave decomposition can be regarded a boundary value problem: from the spatial spectrum  $\hat{\mathbf{E}}$  of the electric field  $\mathbf{E}$  in the plane  $z = 0$  as boundary value, the field for arbitrary  $z$  is found as a propagated integral (Fourier transform) of the plane wave amplitudes. As such, the PWD inherits all uniqueness and existence theorems from Fourier theory.

**BACKWARDS TRAVELING WAVES:** We restricted the propagation of plane waves to the positive  $z$ -hemisphere by choosing the positive branch of the square-root in Equation (15). Due to the linearity of the *wave equation*, plane waves traveling into the  $-z$  half-plane (i.e.  $k_z < 0$ ) can be accounted for in a similar manner by adding in (27) a term with a “negative” propagator term

$\mathcal{P}_{-\mathbf{k}_\perp}(z)$ , such that the electric field  $\mathbf{E} = \mathbf{E}_{k_z > 0} + \mathbf{E}_{k_z < 0}$  is a superposition of forwards ( $k_z > 0$ ) and backwards ( $k_z < 0$ ) traveling waves. Owing to this square-root ambiguity, only explicit knowledge of both amplitude vectors  $\mathbf{E}_{k_z > 0}$  and  $\mathbf{E}_{k_z < 0}$  fully determines a unique solution.

**MULTICHROMATIC CASE:** Only the time-independent case was discussed so far. In general, the field  $\mathbf{E}$  is a function of the time  $t$  as well:  $\mathbf{E} = \mathbf{E}(\mathbf{r}, t)$ .  $\hat{\mathbf{E}}$  is accordingly in explicit functional dependence of  $\omega$  and is retrieved through inverting Equation (21) for  $z = 0$  by applying the inverse Fourier transform in the time domain as well:

$$\hat{\mathbf{E}}(\mathbf{k}_\perp, \omega) = \mathcal{F}_t[\mathcal{F}_{\mathbf{r}_\perp}[\mathbf{E}(\mathbf{r}_\perp, z = 0, t)]] . \quad (28)$$

In the context of microscopy, the stationary, monochromatic case is however a legitimate approximation as long as laser pulses are not many orders of magnitude shorter than one nanosecond.

**SHORT LASER PULSES:** A pure monochromatic solution would require that the oscillating electromagnetic wave would have existed unchanged for all times, because the Fourier transform of the delta distribution in frequency space is unity in the time domain. Nonetheless, a light pulse of length  $\Delta t = 1$  ns, which is a common number in STED nanoscopy, is already long enough to constitute quasi-monochromatic conditions: starting from Equation (21), let us presume a Gaussian spectral density distribution  $e^{-\omega^2/\Delta\omega^2}$  instead of a delta distribution. Except for a normalization factor  $b = \sqrt{2}/\Delta\omega$ , its Fourier transform is a Gaussian light pulse in the time domain [3] :

$$\mathcal{F}_\omega\left[b e^{-(\omega/\Delta\omega)^2}\right] = e^{-(t\Delta\omega/2)^2} =: e^{-(t/\Delta t)^2} , \quad (29)$$

where  $\Delta\omega$  is inferred from the pulse length  $\Delta t$  as  $\Delta\omega = 2/\Delta t$ . The spectral width in terms of the wavelength is deduced according to (9) from  $\Delta\omega = \Delta\lambda 2\pi c/\lambda^2$  as  $\Delta\lambda = \lambda^2/(\pi c)\Delta\omega \approx 10^{-3}$  nm as a rough estimate for visible light  $\lambda$  of about 500 nm. Hence, a (laser) light pulse of one nanosecond length exhibits a minimum spectral width of one picometer. For comparison, the STED laser used in this work has a line-width of approximately 0.1 nm, which still complies well with the assumption of monochromatic conditions.

*... in reminiscence  
of the uncertainty  
principle  
 $\Delta\omega \Delta t \geq 2$ .*

### 2.2.2 PWD and the resolution limit

The plane wave decomposition (27) allows to discuss the resolution limit that is imposed by the finite (i. e. non-zero) wavelength of light

alone. Let us consider as a test-case the propagation of a sharply confined emitter with an idealized lateral frequency amplitude spectrum  $\hat{\mathbf{E}} \equiv 1$ . In the propagator term (26) in Equation (27), the wavelength of light itself imposes a low-pass filter upon wave propagation: for  $|\mathbf{k}_\perp| > k$ , the component  $k_z = \sqrt{(k^2 - \mathbf{k}_\perp^2)}$  becomes imaginary. Accordingly, the exponent  $i k_z z$  in Equation (26) becomes real and its amplitude decreases exponentially with  $z$  as evanescent wave. Figure 5 depicts this low-pass behavior for different values for  $z$ . Upon

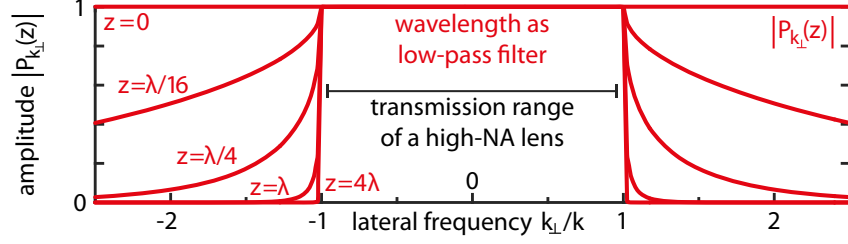


Figure 5: The phase term  $\mathcal{P}_{\mathbf{k}_\perp} = \exp(i k_z z)$  as low-pass filter upon wave propagation into the  $z$ -direction. Amplitude contribution of lateral frequencies  $\mathbf{k}_\perp$  for some values  $z$  relative to the plane  $z = 0$ , where the electric field is known.

propagation of approximately four wavelengths, the propagator term  $\mathcal{P}_{\mathbf{k}_\perp} = \exp(i k_z z)$  closely approaches a (2d) rectangular low-pass function, defined by  $\text{rect}(|\mathbf{k}_\perp|/k < 1) = 1$  and zero else-wise. The high frequency content  $|\mathbf{k}_\perp| > k$  that encodes the exact position of the emitter is clipped solely due to the finite wavelength.

In a microscopy application, it is desirable to recover the original field distribution as accurately as possible by “reversing” the phase propagation effects induced by  $\mathcal{P}_{\mathbf{k}_\perp}$  with a complementary phase-object  $L_{\text{lens}}$  defined as:

$$L_{\text{lens}} = e^{-i k_z f} \text{rect}\left(|\mathbf{k}_\perp|/k^{(\text{max})}\right). \quad (30)$$

*The numerical aperture NA will be discussed in detail in Chapter 3.*

The numerical aperture of the lens restricts the modulus of allowed lateral frequencies  $\mathbf{k}_\perp$  to a range limited by  $k^{(\text{max})} := k \text{NA}/n$ . Inserting  $L_{\text{lens}}$  into Equation (27):

$$\mathbf{E} = \mathcal{F}_{\mathbf{k}_\perp}[\hat{\mathbf{E}} \mathcal{P}_{\mathbf{k}_\perp} L_{\text{lens}}] \stackrel{z=f}{=} \mathcal{F}_{\mathbf{k}_\perp}\left[\hat{\mathbf{E}} \text{rect}\left(|\mathbf{k}_\perp|/k^{(\text{max})}\right)\right] \quad (31)$$

recovers the original, but low-pass-filtered electric field at the position  $z = f$ . Modern objective lenses are close to the limit imposed by the wavelength itself. For comparison, the acceptance range for a numerical aperture (NA) of 1.44 is drawn to scale in Figure (5).

An equivalent real-space formulation of Equation (31) can be derived by employing the fact that a multiplication in Fourier space is equivalent to a convolution in real space:

$$\mathbf{E}(\mathbf{r}_\perp, f) = \mathbf{E}(\mathbf{r}_\perp, 0) * \mathcal{F}_{\mathbf{k}_\perp}\left[\text{rect}\left(|\mathbf{k}_\perp|/k^{(\text{max})}\right)\right]. \quad (32)$$

The Fourier transform of the two-dimensional function  $\text{rect}(\cdot)$  is the so-called jinc-function [10] and its squared magnitude is the ubiquitous Airy pattern. An image is therefore the blurred version of its original intensity distribution; the image of a point-emitter appears convoluted with the Airy pattern.

$jinc(r) := \frac{J_1(\pi r b)}{r/b}$ ,  
with  $b := \kappa^{(\max)}$ .  
 $J_1$  is the first-order  
Bessel function of  
the first kind [24].

### 2.3 WAVE PROPAGATION IN THE SPATIAL DOMAIN

The convolution theorem can generally be employed to express the product in Equation (27) as a convolution in real space [4]:

$$\mathbf{E}(\mathbf{r}_\perp, z) = \mathbf{E}(\mathbf{r}_\perp, 0) * \mathcal{F}_{\mathbf{k}_\perp}[\mathcal{P}_{\mathbf{k}_\perp}(z)] . \quad (33)$$

A derivation by WEYL [62] allows to note the Fourier transform of the propagator in closed form [47]:

$$\mathcal{F}_{\mathbf{k}_\perp}[\mathcal{P}_{\mathbf{k}_\perp}(z)] := \mathcal{P}_{\mathbf{r}_\perp}(z) = \frac{-1}{2\pi} \partial_z \left( \frac{e^{i\mathbf{k}_\perp \mathbf{r}}}{r} \right) = \frac{-1}{2\pi} (i\mathbf{k}_\perp - 1/r) \frac{e^{i\mathbf{k}_\perp \mathbf{r}}}{r} \frac{z}{r} . \quad (34)$$

Inserting Equation (34) into Equation (33) yields

$$\mathbf{E}(\mathbf{r}_\perp, z) = \int \mathbf{E}(\mathbf{r}'_\perp, 0) \mathcal{P}_{\mathbf{r}_\perp}(\mathbf{r}_\perp - \mathbf{r}'_\perp)(z) d\mathbf{r}'_\perp , \quad (35)$$

which is known as ‘‘Rayleigh-Sommerfeld diffraction integral of the first kind’’ (RS1) [24]. We will use it as starting point for calculation of microscope focus fields in Chapter 4.

Equation (35) can  
equivalently be  
derived from the  
Rayleigh-Kirchhoff  
diffraction  
integral [57].

#### 2.3.1 Huygens’ Principle

The RS1 integral (35) is a formal description of Huygens’ principle [37]: Each point on a propagating wavefront serves as a source of secondary wavelets, such that the wavefront at some later time is the superposition of all these wavelets [29]. More precisely, the secondary wavelet as convolution kernel in the RS1 diffraction integral is the normal derivative  $\partial_z$  of a spherical wave  $e^{i\mathbf{k}_\perp \mathbf{r}}/r$  on the integration range  $z = 0$ . Therefore, it defines the amplitude distribution that was not further specified in the heuristic description of the original Huygens’ principle [37]. In particular, the wave has a directive amplitude distribution characteristic – like in Lambert’s cosine law (cf. [57]) – that vanishes in the normal direction to the  $z$ -axis [24].

#### 2.3.2 Discussion

Since RS1 is equivalent to the PWD method, it can be regarded as an exact result. Furthermore, it is a *well-posed* and *consistent* problem: the field for any  $z$  follows from the boundary value in – without loss of generality – the  $z = 0$  plane (well-posed), and the boundary value for

$z = 0$  is indeed assumed (consistent). The latter can be understood as a consequence of the vanishing amplitude of the secondary wavelets in the  $z = 0$  plane.

*boundary value on  
spherical surface*

When the incident field is known on a non-flat surface instead of a plane surface, the situation is slightly different: the boundary value contains contributions from propagated secondary wavelets as well. The problem we will need to solve in the course of the focus field description in Chapter 4 is therefore not a boundary value problem, but rather an *initial value problem*: given the incident light field on the boundary  $E_i(\mathbf{r}')$ , we need to compute the resulting focal field  $E$ , where  $E(\mathbf{r}')$  does not equal  $E_i(\mathbf{r}')$  on the boundary. Note that independently of the exact form of the boundary surface, the solution for  $E$  obeys again the Helmholtz equation (24), because it is a superposition of the normal derivatives of spherical waves that solve the Helmholtz equation individually [5].

## GEOMETRIC PRINCIPLES OF OPTICAL MICROSCOPY

This chapter reviews a collection of key properties and common terminology of an optical microscope as a prerequisite for the subsequent chapter on focus field calculations. Here we approach the topic from a *geometric optics* standpoint, where the electromagnetic field is regarded as an assembly of “pencil rays” with the same general properties as that of plane waves [12]. As such, the pencil rays propagate on straight lines in a homogeneous medium and refract according to Snell’s law [12] at interfaces [45]. This is an instructive simplification for the case when diffraction effects (*wave optics*) play a subordinate role. To a certain degree, geometric optics is related to wave optics like classical mechanics to quantum mechanics [45]: for dimensions that are large compared to the wavelength, the position and the direction of the pencil rays are both exactly determined [45]. Although diffraction effects play indeed a prominent role in the context of microscopy, “geometrical optics furnishes at least a good starting point for more refined investigations” [12].

### 3.1 OVERVIEW

A modern high-performance light microscope is a complex optical and mechanical instrument. Its critical first magnifying stage can however be broken down to a simplistic schematic that consists of two idealized thin lenses, see Figure 6: the objective lens (OL) transforms all

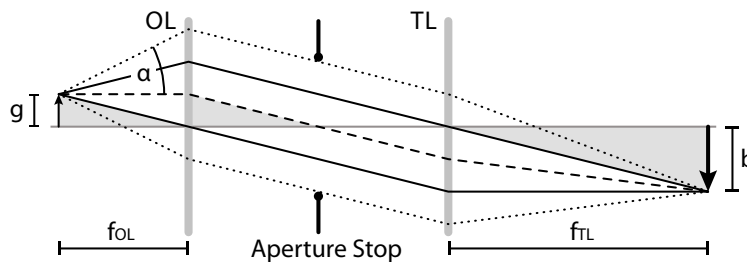


Figure 6: Microscope lens schematic. Objective Lens (OL) and Tube Lens (TL) produce a magnified image.

light rays that emanate from a common point in its focal plane into a set of parallel (*collimated*) rays, which are refocused in the back focal plane of the tube lens (TL). The arrow of length  $g$  as pictorial test-object is mapped onto its (mirrored) image counterpart of length  $b$  that constitutes an *intermediate image*. The set of parallel rays between

In general, thick lenses have got two principal planes. A worthwhile resource for further reading is [45].

This result is a consequence of the sine condition that is discussed in Section 3.3.

both lenses share a common angle in respect to the *optical axis* (horizontal gray line). The angle is geometrically determined by the one ray (drawn in solid black) that remains unrefracted because it goes through the intersect of the *principal plane* of the lens with the optical axis. The same applies in reverse direction at the tube lens. The schematic beam path can be constructed geometrically using these properties, cf. again Figure 6.

The magnification factor  $M$  can readily be deduced by observing that the gray triangles in Figure 6 are similar, hence  $M := b/g = f_{TL}/f_{OL}$ . The dotted lines demarcate the outermost rays (*marginal rays*) that are still accepted by the so-called *aperture stop*. If the aperture stop is situated in the back focal plane of the objective lens (*pupil plane*), *telecentric* conditions are achieved: A point in focus does not move upon slight defocussing; it just appears blurred, but stays centered around the dashed black line in Figure 6. This is a desired property in microscopy because object lengths should not depend on perfect focusing.

The aperture angle  $\alpha$  is defined as the half of the angle enclosed by the marginal rays; the corresponding numerical aperture is defined as  $NA := n \sin \alpha$ . Note also that the numerical aperture is reduced  $M$ -fold in the intermediate image plane, which usually allows to use the paraxial approximation ( $\sin \alpha = \alpha$ ) everywhere except in the “object-side” of the objective lens.

### 3.2 DIFFRACTION LIMIT

The numerical aperture is an appropriate quantity to assess the resolving power of a transmitted light microscope. This review would be incomplete without discussing the famous resolution formula [1] that Ernst Abbe derived 140 years ago along the following lines: consider a transmission diffraction grating of pitch  $d$  with thin slits as in Figure 7. Constructive interference occurs whenever the optical

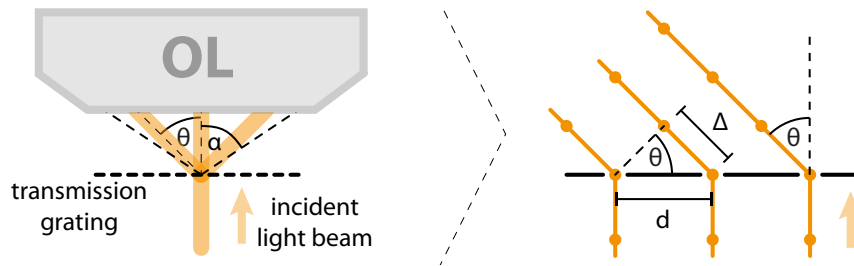


Figure 7: Light transmission and refraction at a periodic diffraction grating structure in the focal plane illustrates the resolution limit.

path length (OPL)  $\Delta_m = d/\sin \theta_m$  of neighboring slits equals an integer multiple  $m$  of the wavelength  $\lambda_n$ . If we decrease  $d$  until  $\theta_1$  becomes larger than the aperture angle  $\alpha$  of the objective lens, only

the diffraction order  $m = 0$  contributes to the image formation, which means that the information of the periodic grating structure is fully lost. Hence,  $d = \lambda_n / \sin \alpha$  is the smallest grating structure that the objective lens can resolve for normally incident light. If oblique incidence is allowed, the smallest grating pitch becomes halved to yield the well-known Abbe resolution formula:

$$d_{\min} = \frac{\lambda}{2n \sin \alpha} = \frac{\lambda}{2 \text{NA}}. \quad (36)$$

Abbe thereby set an end to the at that time common belief that the resolving power of a light microscope was mainly limited by imperfections in the lens-manufacturing process. His formula highlights that, on the one hand, the resolution is tightly linked to the wavelength, and on the other hand, that it increases alongside with the numerical aperture. High aperture angles place however great demands on the imaging optics. In another lasting contribution, Abbe described a requirement to achieve undistorted imaging: the so-called *sine condition*.

*A condenser lens that matches the aperture of the objective lens is widely used to yield isotropic oblique illumination in transmitted light microscopy.*

### 3.3 SINE CONDITION

The Abbe sine condition [2] is a requirement for a high-aperture objective lens to obtain an image free of spherical aberrations and free of coma [12, 42, 45]. To derive the sine condition, we demand a constant lateral magnification  $M$  throughout the whole image plane. Consider a transmission grating with pitch  $d$  in the focal plane. A microscope with  $M$ -fold magnification must generate a correspondingly increased image grating pitch  $d' = M d$ . Inserting  $d = \lambda_n / \sin \theta$  according to Section 3.2 yields:

$$\frac{\lambda_{n'}}{\sin \theta'} = M \frac{\lambda_n}{\sin \theta}, \quad (37)$$

or equivalently, the Abbe sine condition:

$$\frac{\sin \theta}{\sin \theta'} = \frac{n'}{n} M. \quad (38)$$

The sine condition ensures that corresponding angles of light rays are properly mapped to reproduce a grating image with correct phase and magnification.

To gain further insights, we use  $M = f_{\text{TL}}/f_{\text{OL}}$  from Section 3.1 to rearrange Equation (38), and obtain [42]

$$f_{\text{OL}} n \sin \theta = f_{\text{TL}} \sin \theta'. \quad (39)$$

For any given  $\theta$ , the product on the right-hand side is constant because it contains only quantities of the imaged grating. A large value for  $f_{\text{TL}}$  allows to approximate the sine as  $\sin \theta' \approx \tan \theta' = h/f_{\text{TL}}$ , where  $h$  denotes the height  $h$  of the ray above the unrefracted ray

*Without loss of generality, the common case  $n' = 1 \approx n_{\text{air}}$  was chosen to simplify the notation.*

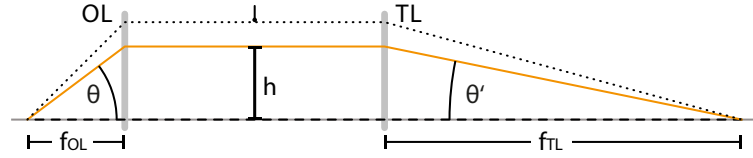


Figure 8: The sine condition defines how an angle  $\theta$  of a ray in object space must be mapped to a height  $h$  in the pupil plane and back to an angle  $\theta'$  in image space to allow for an aberration-free image.

(see Figure 8). Substituting this into Equation (39) and abbreviating  $f_n := n f_{OL}$  leads to an alternate formulation of the sine condition that is also known as *von Bieren condition* [42]:

$$h = f_n \sin \theta. \tag{40}$$

The geometric interpretation of Equation (40) is sketched in Figure 9.

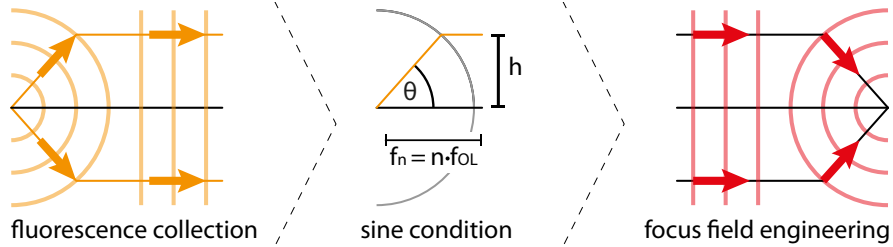


Figure 9: Action of a lens and sine condition, depicted for emanating fluorescence light (left side), as general schematic (middle) and for incident light (right).

*Note that since the principal “plane” is represented by a sphere of radius  $f_n$  in this scope.*

Light rays that leave from the focal point under a certain angle  $\theta$  appear refracted at a sphere of radius  $f_n$  and leave the objective lens assembly at a distance  $h$  to the optical axis. The condition dictates the mapping from an angle  $\theta$  to the “height”  $h$  and vice versa: in the scope of *focus field engineering* discussed in Chapter 4 and Chapter 5, rays from the pupil plane are cast into the focal plane accordingly. The latter perspective will be assumed throughout the remaining Chapter.

### 3.4 INTENSITY LAW

As a further condition, the refraction of the light rays at the principal plane (PP2) must obey energy conservation. Equivalently, the energy fluence  $P = A I$ , expressed as intensity  $I$  on a surface element  $A$  has to be conserved. Let us consider a thin ring-like surface element  $A = dh 2\pi h$  in the back principal plane (PP1) plane that is mapped onto the tilted surface element  $A' = f_n d\theta 2\pi h$  on the spherical principal “plane”, see Figure 10. Using the derivative  $dh/d\theta = f_n \cos \theta$  of the von Bieren condition (40), we get:

$$\frac{A}{A'} = \frac{I'}{I} = \frac{dh 2\pi h}{d\theta 2\pi h f_n} = \cos \theta. \tag{41}$$

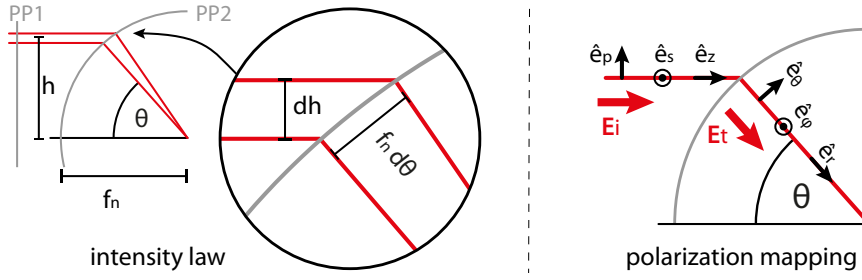


Figure 10: Intensity law and polarization mapping.

Expressing this in terms of the electric field via  $I = |E|^2$  yields

$$E' = E \sqrt{\cos \theta} . \quad (42)$$

The implications of this result will be discussed in Section 4.5.2.

### 3.5 POLARIZATION EFFECTS

Upon refraction at the front principal “plane”, a deflection of the polarization of the electric field vector takes place as well (see Figure 10). Similarly to [44], I propose to express the electric field vector in terms of the cylindrical base vectors  $(\hat{e}_s, \hat{e}_p, \hat{e}_z)$  in the back principal plane. The components are mapped onto a spherical base  $(\hat{e}_\varphi, \hat{e}_\theta, \hat{e}_r)$  to properly account for the rotation of the wave-vector  $\mathbf{k}$  upon refraction. The s-polarized portion of the electric field vector remains untouched  $(\hat{e}_s = \hat{e}_\varphi)$ , while  $\hat{e}_p$  is mapped onto  $\hat{e}_\theta$  and  $\hat{e}_z$  is mapped onto  $\hat{e}_r$ . These base vectors in Cartesian component notation read:

$$\hat{e}_s = \begin{pmatrix} -\sin \varphi \\ \cos \varphi \\ 0 \end{pmatrix}, \quad \hat{e}_p = \begin{pmatrix} \cos \varphi \\ \sin \varphi \\ 0 \end{pmatrix}, \quad \hat{e}_z = \begin{pmatrix} 0 \\ 0 \\ 1 \end{pmatrix} \quad (43)$$

and

$$\hat{e}_\varphi = \hat{e}_s, \quad \hat{e}_\theta = \begin{pmatrix} \cos \varphi \cos \theta \\ \sin \varphi \cos \theta \\ \sin \theta \end{pmatrix}, \quad \hat{e}_r = \begin{pmatrix} -\cos \varphi \sin \theta \\ -\sin \varphi \sin \theta \\ \cos \theta \end{pmatrix}. \quad (44)$$

It can be readily verified that both sets in the first and second row respectively constitute indeed an orthonormal basis. The formal transformation from the incident field  $\mathbf{E}_i(h, \varphi)$  to the transmitted field  $\mathbf{E}_t(\theta, \varphi)$  is given by

$$\mathbf{E}_t(\theta, \varphi) = t_p (\mathbf{E}_i \cdot \hat{e}_p) \hat{e}_\theta + t_s (\mathbf{E}_i \cdot \hat{e}_s) \hat{e}_s + t_z (\mathbf{E}_i \cdot \hat{e}_z) \hat{e}_r. \quad (45)$$

The complex-valued scalar functions  $t_p$ ,  $t_s$  and  $t_z$  are transmission coefficients that can contain empiric factors, such as absorption, apodization, Fresnel reflection losses, phase distortions, or non-zero beam angles (cf. [44]). For an idealized input field and normal incidence, these functions are simply equal to unity.

*In practice,  $E' < E \sqrt{(\cos \theta)}$ , if scattering, reflection and and absorption are taken into account.*

*The polarization vector is expressed in components perpendicular (“s”) and parallel (“p”) to the plane that is defined by the refracting ray.*

*Note that the z-component  $\mathbf{E}_i \cdot \hat{e}_z$  should be small compared to  $|\mathbf{E}_i|$  to maintain a paraxial input field (e.g.  $|\mathbf{E}_{i,z}|/|\mathbf{E}_{i,\perp}| < 1/20$  for a 100x objective lens and a FOV of 200  $\mu\text{m}$  diameter).*

## 3.6 DISCUSSION

Now that all preliminaries are presented, we can summarize: the objective lens transforms a set of focused rays (i.e. a spherical wave), stemming from a point in the focal plane, into a set of collimated rays (i.e. a plane wave) in the pupil plane (cf. Section 3.1). The transformation of distinct light rays appears to take place at a spherical shell with radius  $f_n$  around every point in the focal plane, where three things happen: first, the refraction is described by the sine condition in Equation (40). Second, the polarization vector  $\mathbf{E}_i$  is rotated accordingly in a geometrical consistent manner in Equation (45) and third, the intensity transforms according to the intensity law in Equation (42).

While the sine condition implicitly assumed the special case of rays emanating from the focal point (on the optical axis), the geometric construction (cf. Figure 6) of the beam-path can be expanded to the high-aperture case, which is illustrated in Figure 11.

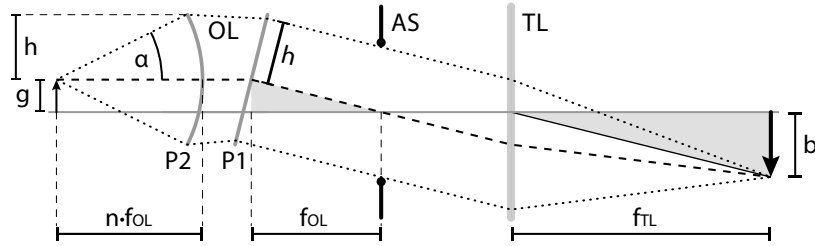


Figure 11: Microscope lens schematic. Geometric construction of the beam path for the high-NA case.

#### Preview of the Debye approximation

From the perspective of focus field engineering, all steps are seen the other way around: A light field propagates from the pupil plane towards the focal plane. According to the Huygens' principle (cf. Section 2.3.1), secondary wavelets that emanate from the principal "plane" propagate as spherical wave with direction-dependent amplitude. In the vicinity of the focus, the spherical wavefront is in good approximation a plane wave, while the amplitude of the spherical wavelets  $u$  has dropped uniformly by  $f_n^2$ . Presuming that these two *ad-hoc* assumptions hold, which means that  $u \approx \exp(i\mathbf{k} \cdot \mathbf{r})/f_n^2$ , we can readily state the focal field in the *Debye approximation* [16]

$$\mathbf{E}(\mathbf{r}_\perp, z) = \frac{1}{f_n^2} \int \frac{\mathbf{E}_t(\theta, \varphi)}{\cos \theta} e^{i\mathbf{k}_\perp(\theta, \varphi) \cdot \mathbf{r}_\perp} e^{ik_z(\theta, \varphi)z} d\Omega. \quad (46)$$

I will derive this result more formally in Chapter 4.

## 4.1 PROBLEM DEFINITION

The goal of this chapter is to present a formalized solution to the time-independent wave equation in the context of high-aperture microscopy. In this scope, the task is seen from a *focus field engineering* perspective: light is cast into the pupil plane of the objective lens and forms a diffraction pattern in the focal plane. The idealized objective lens is considered a “black box” that translates the electric field from the back principal plane (PP1) to its associated points on the front principal surface (PP2), as illustrated in Figure 12. Here I

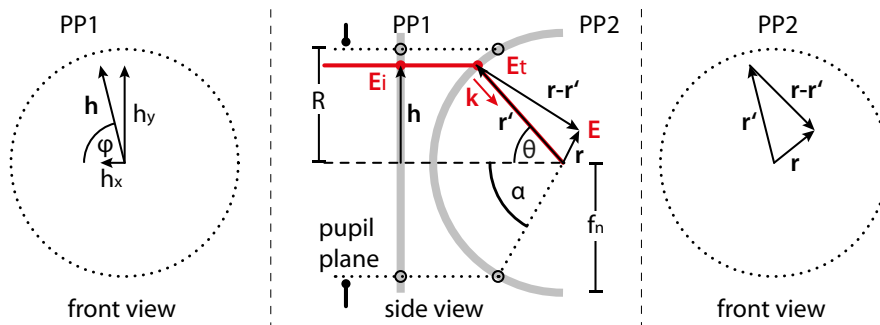


Figure 12: Variables used for focus field calculations.

deviate from the common textbook definition, where the front principal surface is a plane, which is a good approximation only in the paraxial limit. However, for high-aperture systems obeying the sine condition in Equation (40), the principal surface constitutes a sphere of geometrical radius  $f_n$  around the focal point. As detailed in Section 3.6, the wave-vector and polarization vectors become refracted according to Section 3.5, and the amplitude transforms according to the intensity law in Section 3.4. Note that the transition of the light field from the aperture stop in the pupil plane to the back principal PP1 is not considered explicitly. If required, the propagation can be calculated according to the plane wave decomposition discussed in 2.2 (cf. also [44]).

## 4.2 SOLUTION IN SPHERICAL COORDINATES

The Rayleigh-Sommerfeld integral given in Equation (35) generalized to an arbitrary integration surface  $\mathcal{S}$  can be written as

$$\mathbf{E}(\mathbf{r}) = \frac{-1}{2\pi} \int_{\mathcal{S}} \mathbf{E}_t(\mathbf{r}') \partial_{\mathbf{n}} \left( \frac{e^{i\mathbf{k} \cdot (\mathbf{r} - \mathbf{r}')}}{|\mathbf{r} - \mathbf{r}'|} \right) d\mathbf{r}'. \quad (47)$$

The field  $\mathbf{E}_t(\mathbf{r}')$  is assumed to be known on the surface coordinates  $\mathbf{r}' \in \mathcal{S}$ , and  $\partial_{\mathbf{n}} := \mathbf{n} \cdot \nabla$  is the gradient operator in direction of the normal vector  $\mathbf{n}$  on the surface element  $d\mathbf{r}' = \mathbf{n} dS$ .

Specialized on the context of microscopy, the integration spans over a spherical cap with radius  $|\mathbf{r}'| = f_n$  (compare Figures 9 and 10). By transforming to the spherical coordinate measure  $d\mathbf{r}' = \mathbf{n} f_n^2 d\Omega$  with  $\mathbf{n} = \mathbf{r}'/f_n$  and using the abbreviation  $R = |\mathbf{R}| = |\mathbf{r} - \mathbf{r}'|$  we can rewrite the integral (47) as

$$\mathbf{E}(\mathbf{r}) = \frac{-f_n^2}{2\pi} \int_{\Omega} \mathbf{E}_t(\mathbf{r}') \left( ik - \frac{1}{R} \right) \frac{e^{i\mathbf{k} \cdot \mathbf{R}}}{R} \frac{\mathbf{R} \cdot \mathbf{n}}{R} d\Omega. \quad (48)$$

It is convenient to perform the integration in terms of the flat principal plane PP1 in terms of the incident field  $\mathbf{E}_i$ , see Figure 12.

## 4.3 INTEGRATION IN THE PRINCIPAL PLANE PP1

To evaluate the lateral field distribution for general, non-symmetric cases, Cartesian coordinates are the better choice. They allow to express the diffraction integral (48) as a two-dimensional Fourier integral, which can be efficiently computed by means of the *Fast Fourier Transform* (FFT), a particularly efficient numerical algorithm: It performs the integration of an  $N \times N$  grid of sampling points for  $N \times N$  output points in a lateral plane with computational efficiency of order  $\mathcal{O}(N^2 \log N)$ , whereas the “brute force” integration method by means of a two-dimensional Riemann sum would be of order  $\mathcal{O}(N^4)$  [24]. To exploit the FFT, the integration measure  $d\Omega = \sin \theta d\theta d\varphi$  in (48) must be expressed in terms of Cartesian coordinates in the PP1 plane. Combining the von Bieren condition (40) in its differential form  $dh = f_n \cos \theta d\theta$  and the coordinate-transform identity  $h dh d\varphi = dh_x dh_y$ , the integration measure can be written as

$$d\Omega = \frac{1}{f_n^2} \frac{dh_x dh_y}{\cos \theta}. \quad (49)$$

This allows to transform Equation (48) into Cartesian coordinates  $\mathbf{h}_{\perp} = (h_x, h_y)$  in the principal plane

$$\mathbf{E}(\mathbf{r}) = \frac{-1}{2\pi} \int_{|\mathbf{h}_{\perp}| < f \text{ NA}} \frac{\mathbf{E}_t(h_x, h_y)}{\sqrt{\cos \theta}} \left( ik - \frac{1}{R} \right) \frac{e^{i\mathbf{k} \cdot \mathbf{R}}}{R} \frac{\mathbf{R} \cdot \mathbf{n}}{R} d\mathbf{h}_{\perp}, \quad (50)$$

where the intensity law (42) is already taken into account and again  $R = |\mathbf{r} - \mathbf{r}'|$ . Note that  $\mathbf{r}'$  transforms like  $\mathbf{r}' = (\mathbf{h}_\perp, \sqrt{f_n^2 - \mathbf{h}_\perp^2})$ .

To obtain a formal resemblance of Equation (50) with the Fourier Transform given in (20), we further deduce from geometric reasoning that  $\mathbf{r}'/f_n = \mathbf{k}/k$ , and  $\mathbf{h}_\perp/f_n = \mathbf{k}_\perp/k$  (cf. Figure 12). The integration measure  $d\mathbf{k}_\perp$  in Equation (20) in terms of  $d\mathbf{h}_\perp$  is

$$d\mathbf{h}_\perp = f_n^2/k^2 d\mathbf{k}_\perp. \quad (51)$$

The integration range can be expanded to infinity by introducing into Equation (50) a “windowing function”  $W$  that sets all values outside the pupil to zero [44]. The simplest choice is the binary function

$$W = \text{rect}(\mathbf{k}_\perp^2/k_{\text{max}}^2), \quad (52)$$

where  $k^{(\text{max})} := k \text{ NA}/n$ , but a variant with smoother edges can make sense to account for the *apodization* introduced by a real objective lens transmission function. In a numerical implementation, a smoother function reduces *ringing* artifacts from a binary step [44]. Inserting a factor of one (i. e.  $e^{i\mathbf{k}_\perp \cdot \mathbf{r}_\perp} e^{-i\mathbf{k}_\perp \cdot \mathbf{r}_\perp}$ ) into the integrand of Equation (48) and using Equation (51) we get the unapproximated focus field  $\mathbf{E}$  in the notation of the *forward* Fourier integral

$$\mathbf{E}(\mathbf{r}) = \frac{-f_n^2}{2\pi k^2} \int W \frac{\mathbf{E}_t(\mathbf{k}_\perp)}{\sqrt{\cos \theta}} \left( ik - \frac{1}{R} \right) \frac{e^{i(kR + \mathbf{k}_\perp \cdot \mathbf{r}_\perp)}}{R} \frac{\mathbf{R} \cdot \mathbf{n}}{R} e^{-i\mathbf{k}_\perp \cdot \mathbf{r}_\perp} d\mathbf{k}_\perp \quad (53)$$

$$= \frac{-f_n^2}{2\pi k^2} \mathcal{F}_{\mathbf{k}_\perp} \left[ W \frac{\mathbf{E}_t(\mathbf{k}_\perp)}{\sqrt{\cos \theta}} \left( ik - \frac{1}{R} \right) \frac{e^{i(kR + \mathbf{k}_\perp \cdot \mathbf{r}_\perp)}}{R} \frac{\mathbf{R} \cdot \mathbf{n}}{R} \right]. \quad (54)$$

This result is particularly valuable when the conditions deviate from the usual case, which is the evaluation of electric fields with small lateral extend (i. e. few microns) around the focal point. The present study employs a considerably larger beam that extends over a field of view of  $33 \mu\text{m}$  in the focal plane. It is therefore required to evaluate the validity of the approximations assumed in the course of Section 4.4. A detailed assessment in Appendix C suggests that the approximations made in the following Section are valid, provided that the considered field of view is less than  $40 \mu\text{m}$  in diameter.

#### 4.4 APPROXIMATIONS IN FOCUS FIELD CALCULATIONS

The diffraction integral (53) can be considerably simplified in the vicinity of the focal point [16, 64], where the approximations  $r \ll f_n$  and  $\lambda_n \ll f_n$  are presumed to hold. This allows us to use the following implications:

$$1) e^{ikR} \approx e^{ikf_n} e^{-ikr} \quad (\text{see also Appendix C}),$$

- 3)  $R \approx f_n$  in all cases other than the exponent,  
 2)  $ik - 1/R \approx ik$  ,  
 4)  $\frac{\mathbf{R} \cdot \mathbf{n}}{R} = \frac{\mathbf{r} \cdot \mathbf{n} - \mathbf{r}' \cdot \mathbf{n}}{R} \approx \frac{-\mathbf{r}' \cdot \mathbf{n}}{f_n} = -1$  .

Fed into the diffraction integral (53) together with some rearrangements yields the approximated focus field  $\mathbf{E}(\mathbf{r})$  in terms of a Fourier transform (previously derived in a very similar notation [44]):

$$\mathbf{E}(\mathbf{r}) = \frac{if_o \lambda_o}{(2\pi)^2} e^{ik f_n} \mathcal{F}_{\mathbf{k}_\perp} \left[ W \frac{\mathbf{E}_t(\mathbf{k}_\perp)}{\sqrt{\cos \theta}} e^{-ik_z z} \right] . \quad (55)$$

This formulation facilitates the numerical evaluation and allows to interpret the action of an objective lens in terms of a Fourier transformation. Technical details regarding the numerical calculations can be found in [44]. The listing of a minimal working example that is used to calculate the light fields required in Chapter 5 can be found in Appendix D.

#### 4.5 DISCUSSION

Equation (55) deserves some interpretation. The focus field  $\mathbf{E}(\mathbf{r})$  is the scaled Fourier transform of the truncated, weighted (42) and vector-component transformed (45) input field  $\mathbf{E}_i$ . Note that equation (55) constitutes a plane wave decomposition of the focus field at  $z = 0$ , and field values  $z \neq 0$  are retrieved as the propagated field as explained in Section 2.2. As such,  $\mathbf{E}(\mathbf{r})$  is an exact solution to the Helmholtz equation (24).

##### 4.5.1 The Airy-pattern in the light of high-NA microscopy

The lateral bandwidth (resolution limit) is explicitly determined by the windowing function  $W = \text{rect}(|\mathbf{k}_\perp|/k^{(\max)})$ . As in Section 2.2.2, its (squared) Fourier transform is again the well-known Airy-pattern [24]

$$I_{\text{Airy}}(\mathbf{r}) = (\text{jinc}(\mathbf{r}))^2 = \left( k^{(\max)} J_1 \left( \pi r k^{(\max)} \right) / r \right)^2 . \quad (56)$$

According to the convolution theorem, Equation (55) is indeed a convolution of the weighted, transformed and propagated field  $\mathbf{E}_i$  and the jinc-function. A point emitter in the focal plane will not appear any longer as Airy-pattern in the image plane, because it was “distorted” by the mentioned transformations before the convolution is performed. Only in low-NA systems does the approximation  $\mathbf{E}_i \approx \mathbf{E}_t$  hold. In other words, the transformation of the vector-valued electric field upon refraction at the principal plane is negligible in the paraxial (low-NA) approximation. In any case, the convolution with the

jinc-function will clip high spatial frequencies. As in Section 2.2, this finding underscores that the diffraction limit is ultimately caused by the finite  $k$ -vector and correspondingly by the non-zero wavelength of light.

#### 4.5.2 Interpretation of the “obliquity factor”

The amplitude weighting  $1/\sqrt{\cos\theta}$  in Equation (55), that originates from the intensity law (42) in conjunction with the coordinate transform (49), can be interpreted as geometric “obliquity factor”: consider a Gaussian input beam at the rim of the aperture (i. e. oblique illumination). The Fourier transform of a Gaussian function is again a Gaussian function, therefore a (round) beam in the pupil plane must map to a (round) counterpart in the focal plane. Since the beam hits the focal plane under an angle  $\cos\theta$ , its intensity  $|E|^2$  perpendicular to the propagation direction  $\hat{e}_k$  is geometrically squeezed by a factor  $\cos\theta$ . Its elliptical cross-section, projected onto the focal plane, recovers the round shape, see Figure 13. The photon density of the beam,

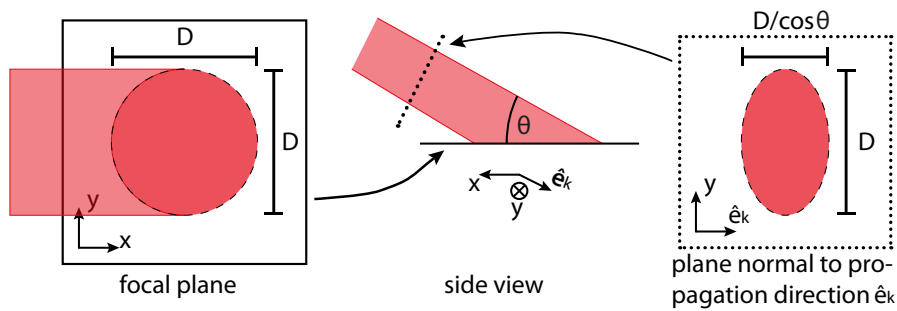


Figure 13: An oblique incident beam that appears round in the focal plane has a “squeezed”, elliptical cross-section and thus a higher intensity.

as experienced by fluorophores in the focal plane, gets enlarged accordingly by a factor of  $1/\cos\theta_0$ . Therefore, oblique incident beams exploit the power of a laser beam more efficiently.



## STED NANOSCOPY

After having derived an appropriate solution to the focus field calculations in the previous Chapter, the present Chapter discusses its implications on the resolution scaling in STED nanoscopy.

## 5.1 CONCEPTS OF STED NANOSCOPY

The key idea underlying STED/RESOLFT nanoscopy is to make use of internal fluorophore state transitions and to drive these transitions in a spatially controlled manner (cf. Chapter 1 and Figure 14). Fluorescent molecules can then be read out sequentially at precisely defined coordinates without signal interference from their immediate neighbors. In the STED concept [34], a suitably engineered light field defines locations in the sample plane where the excited fluorescent state remains allowed but enforces return to the non-fluorescent ground state by stimulated photon emission everywhere except in the close proximity of these locations. It allows to acquire signals with spatial resolutions that lie significantly below the diffraction limit, and to register an image by scanning. An intriguing conceptual consequence is that the fluorescent state can in principle be confined down to arbitrarily small spots [30].

*Major parts of this Chapter are a refinement of the text and the figure that I prepared for a first-author publication [6].*

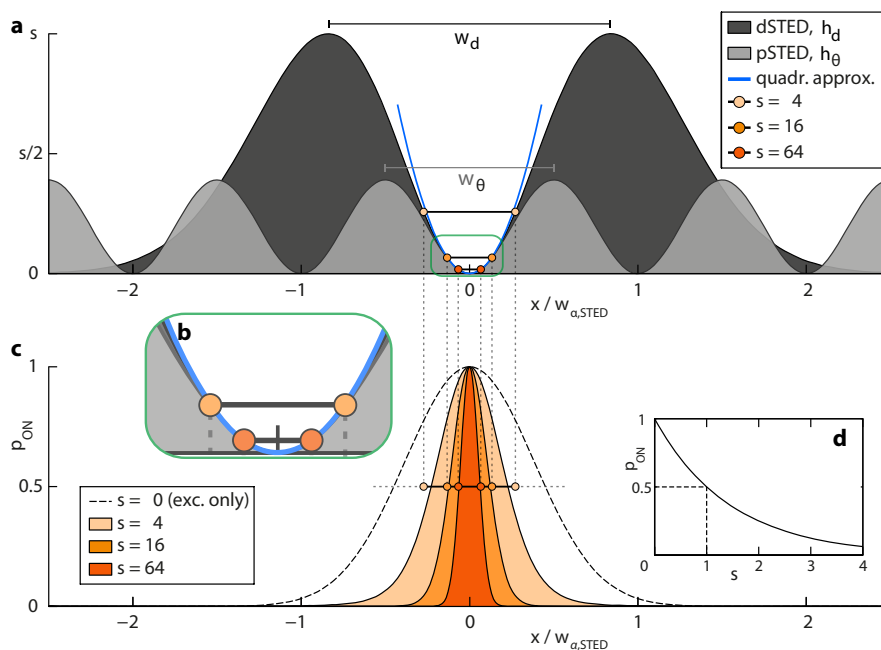


Figure 14: Resolution comparison of the serial (pSTED) and parallelized (dSTED) approach.

## 5.2 RESOLUTION SCALING IN STED NANOSCOPY

This section revisits the well-established expression for resolution enhancement beyond the Abbe limit in STED/RESOLFT-type nanoscopy and compares the cases of classical donut-based STED (dSTED) and parallelized STED (pSTED). To concentrate on the conceptual basis, the discussion in this chapter assumes that the STED pulse duration  $t_{\text{STED}}$  is short enough compared to the fluorescence lifetime  $t_{\text{fl}}$  so that the STED action can be considered an instantaneous process. The orientation of the fluorophore dipole relative to the light-field polarization is also not considered.

*In this thesis,  
 $t_{\text{STED}} \approx 0.7 \text{ ns}$  and  
 $t_{\text{fl}} \approx 3 \text{ ns}$ .*

The STED intensity pattern, depicted in Figure 14 (a), decreases the occupation probability of the fluorescent state according to an exponential decay law [20] (see Figure 14 (d)): the probability that an excited fluorophore is able to reside in the *ON*-state after the STED pulse has left is

$$p_{\text{on}} = \exp(-\ln 2 s) . \quad (57)$$

The saturation parameter  $s = I_{\text{max}}/I_{\text{sat}}$  is the ratio of the maximum light field intensity  $I_{\text{max}}$  and the intensity value  $I_{\text{sat}}$  (*saturation intensity*) at which  $p_{\text{on}}$  is decreased to  $1/2$ , see Figure 14 (c). Notice that the more general but less common definition of the saturation parameter would be  $s = h_{\text{max}}/h_{\text{sat}}$  with  $h$  being proportional to the number of photons per unit area per pulse.

*$h_{\text{sat}} := \ln 2 / \sigma$  is readily related to the cross-section of stimulated emission  $\sigma$  which is of the order of about  $10^{-16} \text{ cm}^2$  [20].*

To produce a spatially targeted switch-off (i. e. inhibition of the fluorescent state occupation), the saturation  $S$  is a function of the lateral coordinate  $x$ , such that

$$S(x) := s h(x) , \quad (58)$$

cf. Figure 14 (a). The spatial intensity function  $h > 0$  is normalized to  $\max_x \{h(x)\} = 1$  to ensure that  $S(x)$  assumes values between zero and  $s$ . The spatial *ON*-state probability then reads

$$p_{\text{on}} = \exp(-\ln 2 S(x)) . \quad (59)$$

In the case of dSTED,  $h(x)$  is the well-known donut-shaped STED light distribution. If we disregard for instance the effects of excitation and detection point spread functions, the resolution can be defined via the full width at half maximum value

$$d = 2 x_{\text{d}} \quad (60)$$

of  $p_{\text{on}}$ . Here,  $x_{\text{d}}$  is given by the solution of  $p_{\text{on}}(x_{\text{d}}) = 1/2$  or, equivalently,

$$S(x_{\text{d}}) = 1 . \quad (61)$$

For relevant saturation values, ( $s \gg 1$ ), the switch-off pattern  $S(x)$  is well approximated around the intensity zero at  $x = 0$  by a second-order Taylor expansion:  $S(x) \simeq s \alpha x^2$ . The parameter  $\alpha$  represents the quadratic term Taylor coefficient and depends on the particular shape of  $h(x)$ . It follows from  $s \alpha x_d^2 = 1$  that the FWHM  $d$  scales according to

$$d \propto s^{-1/2}, \quad (62)$$

which is the famous inverse square-root dependence [28, 30, 60].

**INTERPRETATION OF  $p$ ,  $h$ ,  $s$ :** The switching probability can generally be modeled as  $p_{\text{on}}(x) = f(S(x))$ , with  $p_{\text{on}}$  being the probability that a molecule remains in its original *ON* state.  $f$  is a generic decay law that fulfills  $f(S = 1) = 1/2$ . It comprises the physical properties of the system, including rate equations, timing and background photons. The parameter  $s$  comprises the physical chemistry via  $I_{\text{sat}}$  and the associated state transition cross-section.  $h(x)$  is the spatial intensity function – or photon fluence rate distribution – that is governed by the (diffraction-limited) optics and the associated light-field engineering. The particular shape of  $p_{\text{on}}(x)$  is not important. The resolution  $d = 2x_d$  is readily deduced from the defining equation for  $x_d$ , namely  $h(x_d) = 1/s$ . The curvature of  $h$  around the intensity zero is limited by diffraction. A spatial resolution below the diffraction limit can only be obtained by increasing  $s$ . The resolution increase in dependence of the saturation parameter  $s$  is illustrated in Figure 14 (c).

### 5.3 RESOLUTION FORMULA FOR SINGLE-POINT STED

The quantitative resolution formula for dSTED using the above framework can be derived by considering realistic excitation and STED beam focus fields. These light fields are obtained from numerical calculations based on Listing D that implements Equation (55) in Chapter 4. The numerical implementation follows [44]. The focus field calculation shows that a circularly-polarized donut-shaped STED beam  $h_d$  closely approximates the Laguerre-Gaussian mode (compare Figure 14 (a)):

$$h_d(x) = e^{-\frac{x^2}{(w_d/2)^2}} \exp\left(-\frac{x^2}{(w_d/2)^2}\right). \quad (63)$$

This normalization of  $h_d$  fulfills  $\max_x\{h_d(x)\} = 1$  and the distance of the intensity maxima is  $w_d = 1.68 w_{\alpha, \text{STED}}$ . The characteristic parameter

$$w_{\alpha, i} := \frac{\lambda_i}{2n \sin \alpha}, \quad i \in \{\text{exc}, \text{fl}, \text{STED}\} \quad (64)$$

expresses the width in the according formulae in terms of the Abbe resolution (compare Section 3.2). The numerical factor 1.68 is inferred

*The original publications that virtually all numerical focus field calculations are based on are [63] and [52].*

from the focus field calculation. It indicates that the donut does not exhibit the “steepest” possible confined intensity minimum allowed by diffraction (i. e.  $w_d > w_\theta$  as in Figure 14 (a)). The reason is that the donut shape concurrently confines the STED laser light to a quite localized lateral extent at the expense of a slightly broadened minimum.

The spatial distribution of the excitation beam is well described by a Gaussian function

$$h_{\text{exc}}(x) = \exp(-\ln 2 x^2 / (w_{\text{exc}}/2)^2), \quad (65)$$

The numerical factor 1.15 is inferred from focus field calculation of a Gaussian.

with  $w_{\text{exc}} = 1.15 w_{\alpha, \text{exc}}$ . A moderate, and thus *linear* fluorophore excitation  $p_{\text{exc}} = \varepsilon h_{\text{exc}}$  with  $0 < \varepsilon < 1$  will be presumed in the following. The probability  $p_{\text{fluo}}$  that a fluorophore remains in the fluorescing state after having been exposed to the excitation and STED beam is given by the product  $p_{\text{fluo}} = p_{\text{exc}} p_{\text{on}}$ . The resolution is again defined as the FWHM via  $d = 2 x_d$  of the probability distribution

$$p_{\text{fluo}}(x_d) = p_{\text{exc}}(x_d) p_{\text{on}}(x_d) \stackrel{!}{=} \frac{1}{2} p_{\text{fluo}}(0), \quad (66)$$

and explicitly

$$\exp\left(-\ln 2 \left[ \frac{1}{(w_{\text{exc}}/2)^2} + \frac{se}{(w_d/2)^2} \right] x_d^2\right) \stackrel{!}{=} \frac{1}{2}, \quad (67)$$

where the Taylor expansion of  $h_d(x) \propto e^{-x^2 (w_d/2)^2}$  was used. Simplifying Equation (67) results in

$$\left(1 + \frac{se}{1.86^2}\right) \frac{(2 x_d)^2}{w_{\alpha, \text{fl}}^2} = 1, \quad (68)$$

where  $w_{\alpha, \text{fl}} \approx w_{\text{exc}} = 1.15 w_{\alpha, \text{exc}}$  and  $w_d = 1.68 w_{\alpha, \text{STED}} \approx 1.86 w_{\alpha, \text{fl}}$  was assumed as commonly encountered ratios of excitation, fluorescence and STED wavelengths. Solving Equation (68) for  $2 x_d$  using Equation (64) yields the resolution formula for dSTED:

$$d = \frac{\lambda_{\text{fl}}}{2 \text{NA}} \frac{1}{\sqrt{1 + 0.8 s}}. \quad (69)$$

Note that the assumption  $\lambda_{\text{STED}} = \lambda_{\text{fl}}$  yields the conceptually neat, well-known version  $d = (\lambda/2 \text{NA})/\sqrt{1 + s}$ . The summand “1” in the square-root originates from the Gaussian-shaped excitation spot and can be omitted for large  $s$  to carve out the conceptual dependencies even more.

#### 5.4 RESOLUTION FORMULA FOR PARALLELIZED STED

Similar to the dSTED case, the standing-wave light field for pSTED can be expanded to second order around  $x = 0$ , which reads explicitly:

$$h_\theta(x, y) = \sin^2\left(x \frac{\pi}{w_\theta}\right) + \sin^2\left(y \frac{\pi}{w_\theta}\right) \simeq \left(\frac{\pi}{w_\theta}\right)^2 r^2, \quad (70)$$

where  $r^2 = (x^2 + y^2)$  immediately yields the rotational symmetry of the intensity zero. The coordinate  $y$  can therefore be omitted, and without loss of generality the one-dimensional profile

$$h_\theta(x) := h_\theta(x, 0) \quad (71)$$

is used. The fringe period

$$w_\theta = \frac{\lambda_{\text{STED}}}{2 n \sin \theta} \quad (72)$$

generates steeper intensity zeros than the dSTED donut in case that  $w_\theta < w_d$ . The peak intensity can thus be reduced if the same curvature (respectively, the same resolution) is desired (cf. Figure 14 (a) and (b)). The excitation light field  $h_{\text{exc}}(x)$  can in principle be structured in the same way [66]:

$$h_{\text{exc}}(x) = \cos^2\left(x \frac{\pi}{w_\theta}\right) \simeq \exp(-\ln 2 x^2 / (w_\theta/4)^2). \quad (73)$$

The approximation of  $h_{\text{exc}}(x)$  in terms of the exp-function is used for convenience. In analogy to Equation (66) for the dSTED case discussed in the previous Section, the resolution formula is inferred via

$$\exp\left(-\ln 2 \left[\frac{1}{(w_\theta/4)^2} + s \left(\frac{\pi}{w_\theta}\right)^2\right] x_d^2\right) \stackrel{!}{=} \frac{1}{2} \quad (74)$$

$$\Rightarrow \left(4 + s \left(\frac{\pi}{2}\right)^2\right) \frac{(2 x_d)^2}{w_\theta^2} \frac{w_{\alpha, \text{STED}}^2}{w_{\alpha, \text{STED}}^2} \stackrel{!}{=} 1. \quad (75)$$

A unity factor was inserted to express the subsequent resolution formula in terms of the Abbe limit. Hence, the resolution  $d = 2 x_d$  for the case of parallelized STED is

$$d = \frac{\lambda_{\text{STED}}}{2 \text{NA}} \frac{1}{\sqrt{4 + (\pi/2)^2 s \frac{\sin \theta}{\sin \alpha}}} = \frac{\lambda_{\text{fl}}}{2 \text{NA}} \frac{1}{\sqrt{3.25 + 2 s \frac{\sin \theta}{\sin \alpha}}}. \quad (76)$$

It will be compared to the pSTED case in the next section.

## 5.5 EFFICIENCY COMPARISON OF BOTH VARIANTS

The FWHM-value of the *ON*-state probability  $p_{\text{fluo}}(x)$  that was defined in Equation (66), determines the resolution. In the superresolution regime  $s \gg 1$ , the excitation pattern  $p_{\text{exc}}$  plays a subordinate role and does not contribute significantly to the shape of  $p_{\text{fluo}}$  in the region of allowed fluorescence at  $x = 0$ , see also Figure 14 (c), where a Gaussian excitation pattern is displayed as dashed black line. The resolution gain can therefore be attributed to the probability function  $p_{\text{on}} = \exp(-\ln 2 S(x))$  alone (cf. Section 5.2). Hence, equal Taylor coefficients of quadratic order around  $x = 0$  in the dSTED and pSTED versions of  $S(x)$  imply the same resolution. The condition

$$S_d \stackrel{!}{=} S_p \Leftrightarrow s_d h_d \stackrel{!}{=} s_p h_p \quad (77)$$

thus yields the relation for the saturation factors:

$$\frac{s_d}{s_p} = \frac{(\pi/w_\theta)^2}{e/(w_d/2)^2} = \frac{\pi^2}{e} \left( \frac{1.68}{2} \right)^2 \frac{\sin^2 \theta}{\sin^2 \alpha} = 2.56 \frac{\sin^2 \theta}{\sin^2 \alpha}. \quad (78)$$

Here, Equations (63) and (70) that define  $h_d$  and  $h_p$ , respectively, were used. Therefore, the peak intensity  $I_p/I_d = s_p/s_d$  can be up to 2.5 times lower for pSTED. This can be understood with the non-rigorous argument that excess switch-off intensities (e. g.  $s > 8$ ) add no benefit, but are a byproduct of the high intensities needed to confine the region of allowed fluorescence. The 2d fringe pattern used in pSTED is more efficient in this regard. Note that the second fringe pattern superposes the first one orthogonally such that the intensity doubles in the ‘‘corners’’ of the grid pattern.

Next, let us compare the STED power (or similarly, the pulse energy, or the number of photons) needed to acquire one superresolved pixel. For pSTED, this is the power share of one unit cell

$$P_p = I_p w_\theta^2. \quad (79)$$

For dSTED it is the full power required for the donut:

$$P_d = I_p \pi e (w_d/2)^2, \quad (80)$$

and therefore the power ratio reads

$$\frac{P_d}{P_p} = \frac{I_d}{I_p} \frac{e \pi (w_d/2)^2}{w_\theta^2} = \pi^3 \left( \frac{1.68}{2} \right)^4 \left( \frac{\sin \theta}{\sin \alpha} \right)^4 = 15.4 \frac{\sin^4 \theta}{\sin^4 \alpha}. \quad (81)$$

The ‘‘obliquity factor’’  $1/\cos \theta$  (cf. Section 4.5.2) that appears in the approximated focus field calculation (55) adds a subtlety when input powers in the pupil plane, instead of the sample plane, are compared. The intensity of the ‘‘oblique’’ input beams in pSTED is increased by this inverse cosine factor in the focal plane. The ‘‘oblique’’ portions of the STED donut increases the intensity in dSTED as well, but only by a factor of  $\approx 1.3$  according to focus field calculations (Listing D). To compare the same resolution, the powers in the pupil plane are reduced according to these factors. The power ratio for input beams in the pupil plane is therefore

$$\frac{P_{d,pupil}}{P_{p,pupil}} = 15.4 \frac{\sin^4 \theta}{\sin^4 \alpha} \frac{1/\cos \theta}{1.3}. \quad (82)$$

This is the main result of Part I of this thesis.

## 5.6 DISCUSSION

The efficiency ratios are plotted in Figure 15 for  $I_{\max}$  (Equation (78)) as well as for the power ratios in the focal plane (Equation (81)) and

in the pupil plane (Equation (82)). The peak intensity of both fringe patterns combined is taken into account here. Therefore, pSTED features lower intensity peaks only for beam angles  $\theta > 60^\circ$ . The results for the power (or pulse energy) efficiency comparison are much more pronounced and have two important implications if the angle  $\theta$  comes close to the aperture angle  $\alpha$ . First, the up to 15-fold energy efficiency advantage of parallelized STED over donut-STED translates directly to a correspondingly reduced photon dose that hits the sample. Sec-

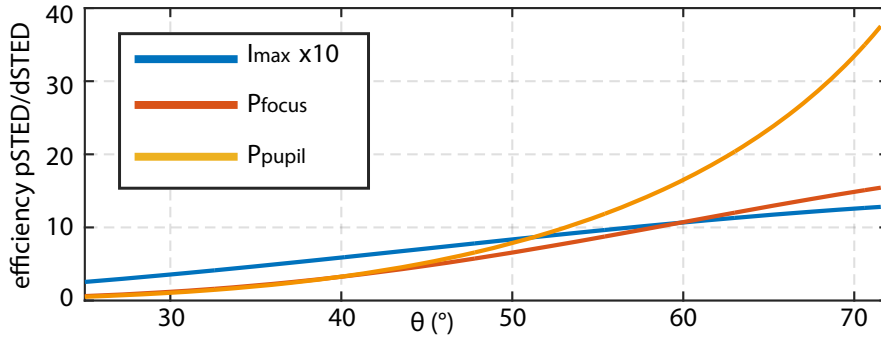


Figure 15: Efficiency comparison of pSTED and dSTED

only, a given laser photon budget (laser power) can be deployed with dramatically increased efficiency in the pSTED case: because the intensity in the obliquely incident STED beams is increased by an additional factor of  $1/\cos\theta/1.3$  up to 2.5-fold in comparison to dSTED, the parallelizing field of zeros can be up to 37-fold larger than a simple scaling of dSTED powers might yield. This is particularly important inasmuch as the available STED pulse energy is still a limiting factor to attain large-scale parallelization.

*To approach the limiting value of the efficiency gain, the STED beams must pass the outer margin of the pupil plane and is subject to apodization.*



## Part II

### EXPERIMENTAL IMPLEMENTATION AND RESULTS

In this experimental Part, I discuss two implementations of massively parallelized STED systems. A first approach proves that sub-30 nm resolutions and 2000-fold parallelized dual-color fluorescence imaging are feasible with two orthogonally crossed standing light waves as a parallelized fluorescence inhibition pattern. A second experimental implementation constitutes a considerably simplified redesign that allows the exploration of conditions that come closer to the theoretical efficiency limits of this approach to parallelize STED. By these means, I was able to enlarge the image area of highest resolution (approx. 30 nm - 40 nm) to 20  $\mu\text{m}$  in diameter (FWHM). As a consequence of the decreasing STED beam intensity towards the periphery of the image size, the resolving power reduces to 50 nm - 60 nm in the "corners" of the full image size of 33  $\mu\text{m}$ . I quantified this resolution dependency and found it in good accordance to the behavior that was expected from the theoretical preliminaries developed in Part I. Closing remarks and an outlook conclude the second Part of this thesis.



## PARALLELIZATION USING AN INTERFEROMETRIC FRINGE PATTERN

---

The present Chapter describes the experimental implementation of a considerably (i. e. 2000-fold) parallelized STED approach. Starting with a discussion of the implementation details, the experimental results are presented and discussed.

*Major parts of this Chapter are a refinement of the text and the figures that I prepared for a first-author publication [6].*

### 6.1 INTERFEROMETRIC FRINGE PATTERN

The key challenge in realizing a parallelized STED setup is to implement a suitable parallelized switch-off beam path. The feasibility study conducted here uses a pair of two-beam interferometers which projects an orthogonal superposition of two sets of interference fringes onto the sample plane of a standard fluorescence microscope (Figure 16). Each of the one-dimensional sinusoidal fringe patterns arises from the plane-wave interference of two beams crossing each other under a certain half-angle  $\theta$ , see Figure 16 (a). In contrast to similar approaches, where gratings [14] or a pair of Wollaston prisms [66] were used, the present approach prepared beams for interference in two separately implemented sets of combined *Michelson* and *Mach-Zehnder*-like arrangements according to Figure 16 (d). Besides high transmission efficiency and full control and flexibility of all four beams, this modality allows to scan the fringe pattern instead of moving the sample. For full modulation depth, the beams must be polarized linearly in direction of the interference fringes (compare the sketch of the pupil plane in Figure 16). Unlike in structured illumination schemes [26, 27, 50], no rotation of the fringe pattern is required. In fact, the created off-switching pattern provides a rotationally uniform resolution (disregarding polarization effects) since the leading term of the Taylor expansion around the intensity nodes is of quadratic order in both lateral dimensions (see Section 5.5). The half-angle  $\theta$  under which the STED beams impinge onto the sample plane governs the fringe period  $w$  (i. e. the separation of adjacent zeros). The defining relation  $w = \lambda / (2 n \sin \theta)$  constitutes a “light grating” that is exactly the inversion of the thought experiment that ERNST ABBE used to derive his resolution formula (Section 3.2). Choosing  $\theta$  close to the aperture angle  $\alpha$  of the objective,  $w$  matches the Abbe resolution limit  $d = \lambda / (2 n \sin \alpha)$  of the widefield microscope. Therefore, this fringe pattern can yield a nearly diffraction-limited density fluorescence inhibition zeros. At the same time, it provides a very efficient means to

generate steeply confined intensity zeros for STED/RESOLFT resolution enhancement (see Section 5.5).

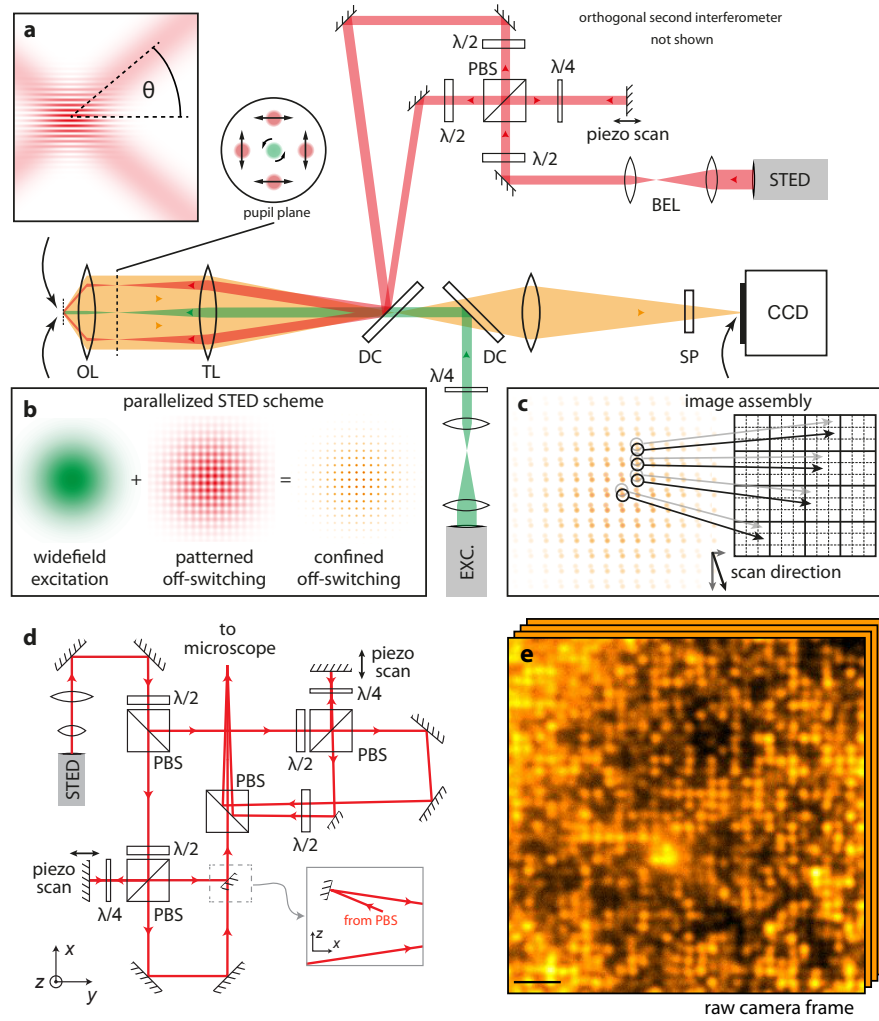


Figure 16: Widefield excitation (green) and patterned off-switching (red) of fluorophores realize the STED concept on a massively parallelized scale. (a) STED off-switching pattern produced as standing wave by interference of crossed beams. (b) Confined fluorescence signals (yellow) stemming from the targeted sample regions are imaged onto the emCCD camera and (c) assigned to their corresponding pixels in the superresolved image. (d) Implementation details of STED beam path. (e) Example of raw data frame detail, scale bar is  $2\ \mu\text{m}$  (in sample plane).

## 6.2 SETUP COMPONENTS

The STED laser used for this study is a frequency-doubled fiber laser prototype (Onefive, Katana HP) with an particularly high pulse energy of  $2000\ \text{nJ}$  at  $1\ \text{MHz}$  repetition rate,  $775\ \text{nm}$  wavelength and a pulse length of  $0.7\ \text{ns}$ . Its beam path is sketched in Figure 16. A Kep-

lerian telescope (BEL: beam expander lenses) expands the STED beam to the desired size. The laser power is balanced between the two interferometers and again between both interferometer arms with a half-wave plate ( $\lambda/2$ ) and a polarizing beam splitter (PBS) in each case as shown in Figure 16 (d). The deflected beams each pass a quarter-wave ( $\lambda/4$ ) plate and are retro-reflected through the plate and through the polarizing beam splitter. The retro-reflecting mirrors are mounted on piezoelectric actuators (Physik Instrumente, P-753.11C with PZT-Servo Controller E-503.C3A), which sit on manual linear stages (Newport, 462-X-M). The linear stages are used to balance the optical path lengths, and the piezo actuators shift the relative phase of the respective beam pair to scan the fringe pattern (“piezo scan”). All four beams are merged with one polarizing beam splitter, reflected off a dichroic (DC) filter (AHF Analysentechnik, F73-746, zt 625-745 rpc) and guided to the microscope (Leica Microsystems, DMI-3000B, APO 100x/1.44 OIL; custom-built sample mount [22] clamped directly onto the objective). Note that the final polarizing beam splitter enforces the correct linear beam polarizations required for full modulation depths.

The excitation source is either a 635 nm laser diode (PicoQuant, LDH-D-C-635), or a supercontinuum laser (Fianium, FemtoPower HP 1060 SC) with two wavelengths (600 nm and 650 nm), selectable via a filter wheel. The excitation light is fed into the common path towards the microscope by reflection off a dichroic beam splitter (Semrock, RazorEdge LP 671) and merged with the switch-off beams at the dichroic band-pass. The pulse trains are coarsely synchronized by cables. Fine tuning is realized via a custom-made electronic delay line (MPI BPC). The STED laser is trigger master when used with the laser diode, and trigger slave when paired with the supercontinuum laser source for excitation. The fluorescence signals are projected onto an electron-multiplying charge-coupled device (emCCD) camera (Andor Technology, iXonEM+ 897). Backscattered STED light is blocked using a short-pass filter (Semrock, BrightLine 750/SP). A camera pixel in a relayed intermediate image plane maps to a 43 nm pixel edge size in the sample plane.

### 6.3 SCANNING STRATEGY

To scan the intensity zeros over the sample, phase differences between the interfering beams are introduced by shifting the retro-reflecting mirrors in the Michelson interferometers with the piezo actuators (denoted “piezo scan” in Figure 16). The unit cell of the fringe pattern, sketched as red square in Figure 17 is sampled on  $n \times n$  grid points (pixels). The first piezo actuator moves  $n$  times faster than the second one, which means that the grid points follow a slightly diagonal path (with slope  $1/n$  relative to the fringe pattern symmetry). This is illustrated in Figure 17, exemplified for  $n = 3$ . By the time  $n$  pixels

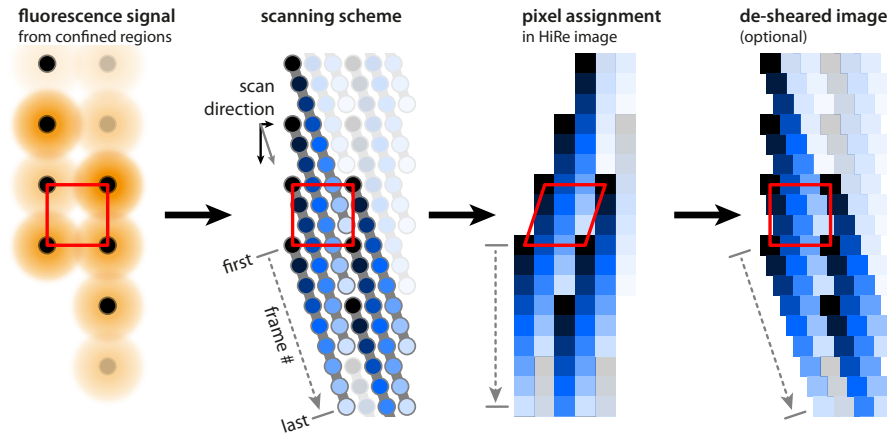


Figure 17: Scanning strategy of the parallelized STED implementation: the unit cell (red) is sampled on a slightly diagonal slope to achieve continuous scanning.

are scanned along the fast axis, the slow-moving piezo has moved one pixel and the next pixel column is scanned. After  $n \times n$  scanning steps, the fringe pattern reaches seamlessly its initial position. This beam-scanning scheme allows for continuous scanning without dead time such as the flyback that is found in galvanometric or object scanners.

#### 6.4 EXPERIMENTAL CONTROL

The experimental control unit consists of an NI USB-6229 multifunction data acquisition module and a self-written LabView control sequence (both products: National Instruments). It triggers the camera as well as the mechanical laser shutters (BRS-3831, Geeplus Europe Ltd, with custom-made driver: MPI BPC) and outputs voltage ramps to move the phase-shifting piezo actuators. Due to the continuous scanning scheme, there is no necessity to synchronize single camera-frames to certain actuator positions. Instead, the time required to scan a full unit cell must accurately match the time to record  $n \times n$  camera frames. An image acquisition sequence comprises a wide-field image (STED laser shutter closed),  $n \times n$  camera frames with high-resolution content, and another widefield image. The mechanical shutters switch rather slowly (within few milliseconds), and transitional camera frames between widefield and STED mode are discarded.

#### 6.5 IMAGE ASSEMBLY

Unlike STED nanoscopy implementations with sequential scanning and a single-pixel detector, the parallelized scheme requires some

considerations to assign the fluorescence photons detected on the camera to the correct superresolved image pixel. At each scanning step, the fluorescence signals from highly confined, fringe-period-spaced sample regions are imaged onto the camera (cf. Figure 16 (b), (c) and (e)). If the period comes close to the diffraction limit  $d$ , the blurred, diffraction-broadened fluorescence spots overlap to a certain degree in the image plane (Figure 16 (e) and Figure 17). (The illustration in Figure 16 (c) and the sketch in Figure 17 do not show this overlap for clarity of display of the concept).

### 6.5.1 Linear regression versus mask followed by crosstalk reassignment

Three conceivable strategies to address this spatial “crosstalk” were examined: first, only the central camera pixels around each emission origin can be considered at the expense of a reduced signal strength. Second, a multi-variate linear regression should yield the most accurate result: because the location and the approximate shape of the fluorescence signal distributions can be determined upfront, only their amplitudes must be fit to the camera frame data. The problem is therefore reduced to a system of linear equations with a unique optimal solution in the least-squares sense. However, the memory requirement of this approach is demanding and scales up unfavorably with the degree of parallelization. Therefore, a third strategy as a compromise between the first two was adopted for the large-scale parallelization: a larger weighted pixel mask (of Gaussian shape) collects a bigger portion of the signal. Subsequently, the “crosstalk” is removed in a linear matrix operation that contains the relative crosstalk in the eight nearest neighbors. Tests on synthetic data have shown only minor differences for strategy two and three, with strategy three demanding a significantly lower processing cost. No knowledge of the exact microscope point spread function is required to implement strategy three. Note that this scheme does not constitute a *deconvolution*. It is simply a linear reassignment of fluorescence counts to its correct image pixel without increasing resolution.

### 6.5.2 Fluorescence signal crosstalk

The photon “crosstalk” into a neighboring zero can be quantified by presuming a (coarsely) Gaussian point-spread function as fluorescence response from the zero region:  $h_{fl}(r) = \exp(-b r^2)$ , where  $b = \ln(2)/(w_{fl}/2)^2$  is just a shorter notation for a Gaussian of width  $w_{fl} = 1.15 \lambda_{fl}/(2 n \sin \alpha)$  just like in Equation (64) in Section 5.3. According to “strategy three” of the previous section, the fluorescence photons are assigned to a superresolved pixel by a multiplicative overlay of a Gaussian mask of the same type:  $h_{mask} = h_{fl}$ . Hence, the collected fluorescence signal is the product  $h_I = h_{fluo} h_{mask}$ . The closest

neighboring zero is the edge length  $w_\theta$  of a unit cell apart, where  $w_\theta = \lambda_{\text{STED}}/(2n \sin \theta)$ , cf. Figure 17. Its signal  $h_{\text{fl},w} = \exp(-b((x - w_\theta)^2 + y^2))$  is collected by the neighboring mask as crosstalk content

$$h_{\text{I,neighb}} = h_{\text{fluo}}(x - w_\theta, y) h_{\text{mask}}(x, y) \quad (83)$$

$$= e^{-b(x^2 + (x - w_\theta)^2 + 2y^2)} \quad (84)$$

$$= e^{-2b(z^2 + y^2)} e^{-2b(w_\theta/2)^2} \quad (85)$$

$$= h_{\text{I}}(z, y) (1/4)^{(w_\theta/w_{\text{fl}})^2} \quad (86)$$

where the substitution  $z := x - w/2$  was made. Except from a lateral shift of  $w/2$ , the collected crosstalk signal  $h_{\text{I,neighb}}$  differs from  $h_{\text{I}}$  only in an amplitude factor, which defines the relative strength of the crosstalk. The relative crosstalk is plotted in Figure 18 in depen-

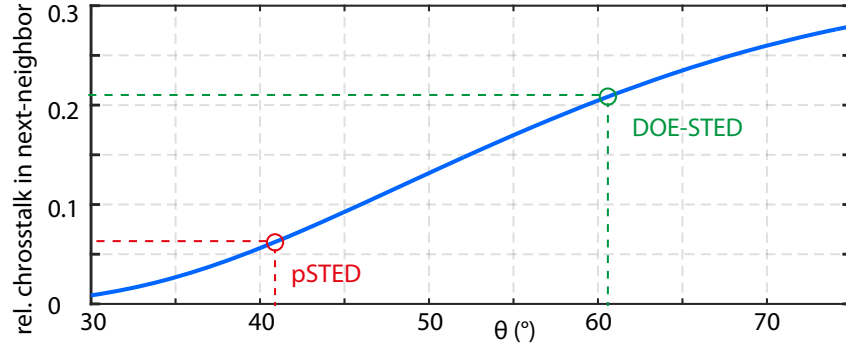


Figure 18: Relative photon crosstalk into the region of a neighboring zero.

dence of the fringe pattern angle  $\theta$ , with the wavelengths  $\lambda_{\text{fl}} = 690$  nm and  $\lambda_{\text{STED}} = 775$  nm inserted into Equation (86). The crosstalk for the present case (denoted as pSTED) and – in anticipation – of the “DOE-STED” implementation described in Chapter 7 are shown. While the spectral crosstalk is a mere 6.5 % at  $41^\circ$ , it increases to 21 % at  $61^\circ$ .

### 6.5.3 Estimation of the fringe period and its phase

In order to implement strategy three discussed in the last section, the exact location of the regions of allowed fluorescence must be known *a priori*. Since the pattern is periodic in the two lateral dimensions, there are five global parameters to estimate: the rotation angle as well as the fringe periods and offsets for both dimensions.

**ROTATION:** The rotation angle of the camera pixel matrix relative to the STED fringe pattern is estimated from a high signal-to-noise pattern image that is recorded from a mirror in the sample plane. This can be achieved by rotating the image of the fringe pattern and then computing its two-dimensional Fourier transform. The correct rotation angle is reached when both lowest frequency bins perpendicular to the one-dimensional fringe pattern are of equal (low) height.

That is, no frequency component on the image axis perpendicular to the one-dimensional fringe pattern remains. The rotation angle will stay constant as long as neither the camera nor the fringe pattern is rotated. It must therefore be estimated only once. Note that the required level of accuracy of the rotation angle scales linearly with the number of used fringe periods in one dimension. For e. g. 100 fringes and 20 sampling steps per dimension, the uncertainty in the rotation angle should be smaller than  $\arctan(1/((100/2) \cdot 20)) \approx 1/1000 \approx 0.16^\circ$  to be less than one sampling step off over the full image range.

**FRINGE PERIOD:** The fringe period is deduced from each stack of fluorescence images: here, the challenge is to deduce the correct fringe pattern from highly noisy fluorescence data. Note that for densely packed unit cells, the fringe pattern is close to the resolution limit. Therefore, the diffractive blurring will reduce the fringe contrast in the fluorescence data. Nonetheless, the dominant frequency will still be present and can be estimated from all combined images in the image stack. Since the spatial fringe frequency will be within a narrow range, the standard Fast Fourier Transform algorithm is not suitable. Instead, two one-dimensional Fourier transforms with dense bins around the true frequency are mimicked: two-dimensional sinusoidal fringe patterns with varying period and offset are multiplied to the image stack, taking the known scanning shift from each image frame into account. The sum of these data gives rise to a heat map, with the true spatial frequency yielding the highest amplitude.

**FRINGE OFFSET:** The fringe offset is retrieved in a similar way, where the fringe period remains fixed and solely the fringe offset is varied.

#### 6.5.4 *Bleaching correction*

As illustrated in Figure 17, image pixel stemming from the fluorescence signal of the first frame are nearest neighbor to the pixels of the last frame. Due to bleaching of the fluorophores in the course of the imaging process, the last image frame will appear dimmer than the first one. Even slight brightness differences become readily visible to the human eye due to the regular fringe pattern symmetry. Therefore, a parallelized scheme requires a thoughtful strategy for bleaching correction. Note that this is not an issue in single-point scanning schemes, because each spot (disregarding image border regions) has experienced the same illumination sequence before being probed.

Two things make the bleaching correction particularly challenging. First, adjacent camera frames may look very different depending on the underlying fluorophore signal strength. Any local fitting scheme must not weaken this local contrast, as it contains the high-resolution

content. Second, the peripheral image region may appear brighter, because the resolution gain decreases and thus larger probing regions are allowed to fluoresce. Therefore, common global bleaching correction strategies (like histogram-based corrections, linear or exponential corrections) do not yield satisfying results in the present case.

Out of many investigated strategies, the following two-step approach yielded the best results: first, a correction based on a global exponential fit was performed. Second, a pixel-wise running median filter along the stack of image frames was subtracted.

#### 6.5.5 *Background subtraction*

To suppress low-resolution background signal, a corresponding scaled widefield background image is subtracted from the superresolved image. Note that while the background signal can be subtracted, its noise contribution remains. The noise contribution is however less pronounced than one might expect, because the reference background image is a (low-noise) mean image of the full high-resolution image stack.

#### 6.5.6 *De-shearing*

The high-resolution image is a slightly sheared image of the original object (cf. Figure 17). For a usual case (e. g.  $n = 20$ ), the shearing angle  $\beta = \arctan(1/n)$  is less than  $3^\circ$  and hence negligible in a biological context. Nevertheless, a numerical de-shearing transformation can ease the comparison with the corresponding widefield image. The de-shearing is an interpolation process that smoothens the image at the cost of a slightly reduced resolution. Alternatively to interpolation, each pixel can be bloated up to  $n \times n$  pixels. Then a lossless de-shearing can be performed by shifting each row of pixel blocks by one pixel relative to its upper neighboring row. While no image information is lost during this procedure, the Fourier spectrum will exhibit an artificial spike at high frequencies due to this step process. Also, an  $n \times n$ -fold increased file size does not seem particularly appealing. Therefore, the sheared original image is preferred.

## 6.6 RESULTS

Having discussed the implementation details, this section presents the experimental results of this part of the project.

## 6.6.1 Sub-30 nm resolution

To assess the highest resolution possible with the available STED laser, the STED pulse energy is concentrated to a narrow Gaussian envelope of  $6.3\ \mu\text{m}$  diameter. The 2d fringe pattern is scanned over the unit cell on  $30 \times 30$  grid points of  $12.5\ \text{nm}$  pixel size each. A unit cell edge size of  $374\ \text{nm}$  yields a roughly 220-fold parallelization within the FWHM region and a 1250-fold parallelization across the full image. Figure 19

*A beam diameter is defined by its full width at half maximum value (FWHM) within this scope.*

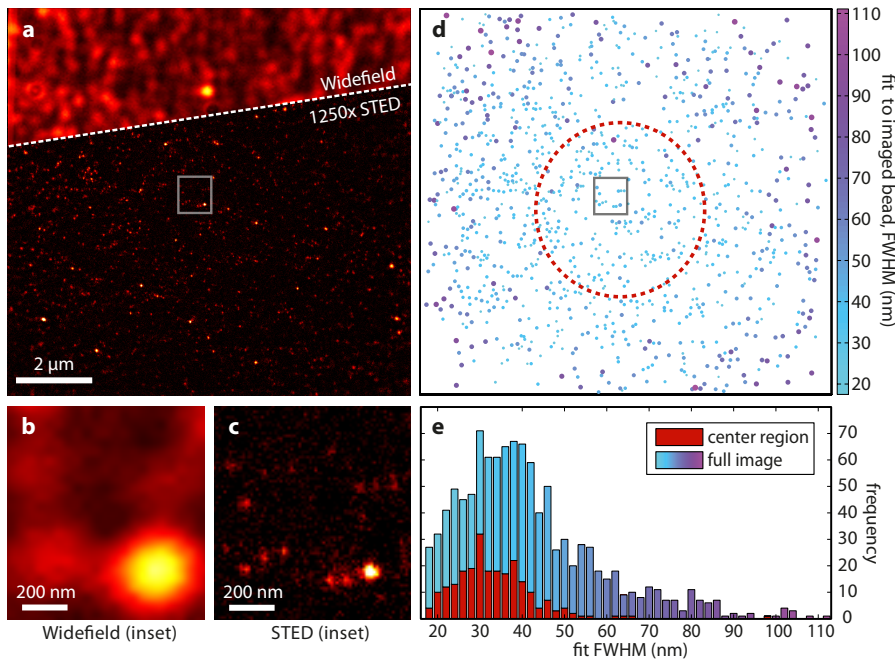


Figure 19: Resolution quantification. (a-c) Parallelized STED vs. widefield image of 20 nm crimson beads with magnified detail view. (d) Fit of the bead diameter, displayed as scatter plot corresponding to (a). (e) Histogram of the FWHM fit values.

shows the superresolved image of dispersed 20 nm-diameter crimson fluorescent microspheres (Thermo Fisher) in comparison to the corresponding widefield microscope image. A magnified view of the boxed region (Figs. 2(b) and 2(c)) reveals the  $\approx 10$ -fold resolution increase.

The image resolution was quantified by fitting the beads with a two-dimensional Gaussian distribution. The results are displayed as a color-coded scatter plot in Figure 19 (d). The resolving power decreases towards the periphery since it scales inversely with the square root of the STED intensity (cf. Section 5.2) and the STED pattern features a Gaussian intensity envelope. The histogram of the fit values in the center region (Figure 16 (e)) peaks at  $\approx 30\ \text{nm}$ . A model calculation treating the bead images as a convolution of the superresolution point spread function with the physical bead size of 20 nm leads to an estimate of the technical resolving power of about 27 nm. The approx-

imate STED pulse energy in the sample plane is 1.5 nJ per unit cell in the center and more than 0.75 nJ per unit cell within the FWHM region.

### 6.6.2 Dual-color imaging on a large field of view

A massively parallelized STED nanoscope poses high demands on the pulse energy output of the STED laser source, because the STED light must illuminate a large area at once for parallel sampling. In the feasibility study conducted here, the STED pulse energy is a limiting factor for simultaneously achieving highest resolution and a large superresolved field of view. Given the Gaussian envelope of the STED intensity, the diameter of the highly resolved field of view scales inversely to the resolution performance as a consequence of the square-root law discussed in Section 5.2. If a lower resolving power of for example  $\approx 55$  nm is sufficient, the STED spot diameter can be doubled accordingly. Figure 20(a) shows crimson (in green) and dark red

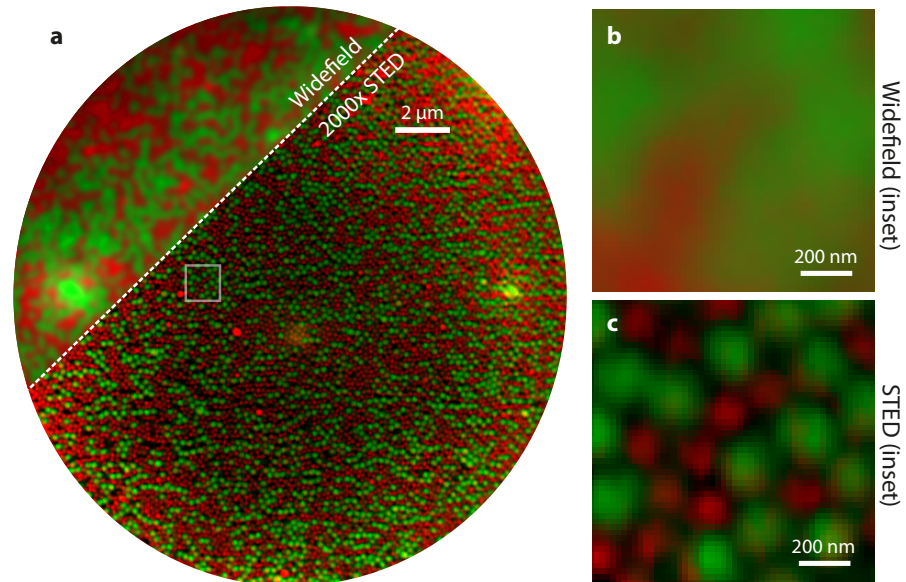


Figure 20: (a) 2000-fold parallelized dual-color STED imaging of 200 nm fluorescent beads. Crimson beads (green color-map) and dark red beads (red color-map). The increased image brightness near the periphery is a consequence of the lower resolution due to fall-off of the STED intensity envelope. (b,c) Magnified view of boxed region in (a).

(in red) fluorescent beads (Thermo Fisher) with nominal diameters of 200 nm dispersed on the cover glass surface. The image pixel size is 20 nm and the (slightly enlarged) 20  $\mu$ m wide circular superresolved region contains  $\approx 2000$  STED zeros. Note that the resolving power gradually decreases to  $\approx 110$  nm towards the edges, which is still well below the diffraction resolution limit. To separate the two

bead-labeling dyes, two images were recorded back-to-back with excitation wavelengths of 600 nm and 650 nm. Since the detection path is unaltered between both consecutive scans, a certain level of cross-excitation of the two dyes in both channels is inevitable. We note that spectral separation as well as colocalization performance could be improved in a straightforward manner by pulse-wise excitation multiplexing and two spectrally filtered detection channels. Both images are merged and colored using a linear un-mixing algorithm similar to the one used in [13]. The magnified view (Figure 20 (b) and (c)) clearly illustrates the information gain of increased resolution. While the widefield image merely distinguishes the presence of both fluorophore colors, the STED image resolves the detailed shape of the beads. For example, the dark red beads appear clearly smaller than specified. The assumption that the imaged size difference indeed traces back to a “real” bead size difference is backed up by the observation that five – and not six – (green) crimson beads surround one (red) dark red bead.

### 6.6.3 *Sub-70 nm resolution in cellular sample*

We next demonstrate the capabilities of parallelized STED imaging on the larger field of view of 20  $\mu\text{m}$  diameter in a biomedical context. An image of a dense Abberior STAR 635P-stained vimentin filament

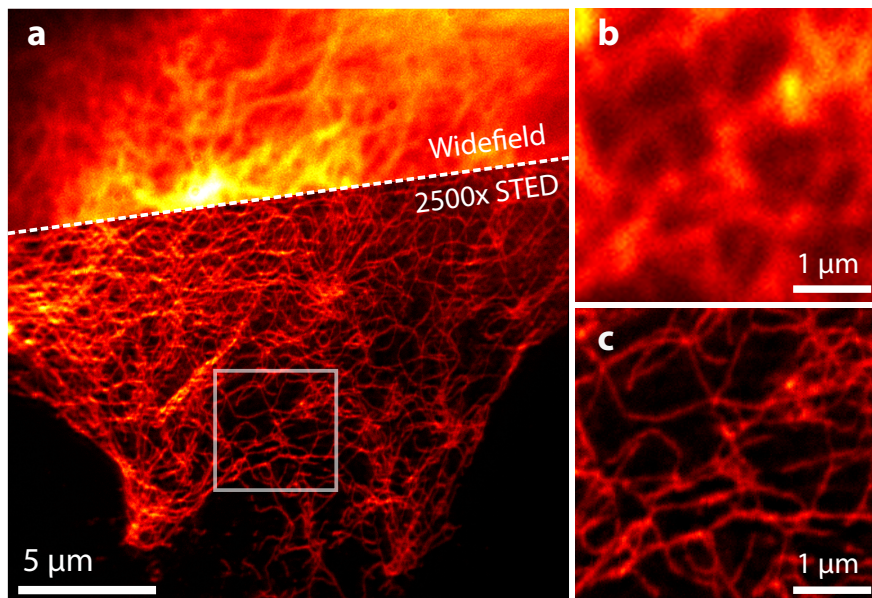


Figure 21: 2500-fold parallelized STED imaging of biological structures. (a) STAR 635P-stained vimentin fibers. Magnified details (b,c) show widefield (top) and STED recordings (bottom) in comparison.

structure in Vero cells is shown in Figure 21 (a). The magnified insets (Figure 21 (b) and (c)) show that the underlying filament structure is

obscured in the widefield image, whereas it is clearly discerned in the STED counterpart.  $N = 28$  fits of elliptical (two-dimensional) Gaussian model functions to highly resolved vimentin fibers in the STED image sets an upper bound for the resolution to  $\approx 69$  nm (mean of fitted FWHM values). In conjunction with the antibody staining (primary and secondary antibodies), the decorated vimentin fibers have a real diameter of  $\approx 45$  nm [22]. The measured profile across the filament is therefore consistent with an estimated instrument resolving power of  $\approx 55$  nm by convolution arguments. The STED energy in this recording was 0.42 nJ per unit cell near the center of the sample plane.

## 6.7 DISCUSSION

### 6.7.1 Resolution and field of view

The main focus of this part of the project was to examine whether parallelized STED nanoscopy using the standing waves as switch-off pattern can attain resolutions comparable to donut-based STED systems. While the area of highest lateral resolution was limited to  $\approx 6$   $\mu$ m, it could be demonstrated that a considerably parallelized STED approach is capable of delivering sub-30 nm resolving power. Moreover, a second configuration with dual-color excitation modality and an enlarged STED beam size allowed for sub-60 nm resolution in the center of a superresolved field of view with 20  $\mu$ m diameter.

### 6.7.2 Polarization bias

Although the applied STED pattern is a superposition of linearly polarized standing waves, no polarization bias in the STED efficiencies could be observed. It appears that sufficient rotational fluorescence depolarization takes place during the comparably long STED pulse length of 0.7 ns [49]. Note however that this effect was found in a context where STED was tuned to detect the molecular orientation of single fluorophore dipole orientations (coined *molecular orientation microscopy* MOM-STED [51]).

### 6.7.3 STED efficiency

Parallelized STED can reduce photobleaching due to its increased power efficiency [66]. As detailed in Chapter 5, parallelized STED based on two orthogonally crossed standing waves can feature steeper intensity gradients around the locations of the zeros compared to the donut-shaped STED variant. In addition, the energy utilized to generate a superresolved spot is inherently shared with neighboring ones. The calculations in Section 5.5 yielded an efficiency advantage

regarding the STED energy density as experienced by the sample of  $15.4 (\sin \theta / \sin \alpha)^4$ . This means that up to 15.4 times reduced photon dose per STED zero is required to achieve the same resolution. For an angle  $\theta \approx 41^\circ$  used in this setup, an efficiency increase close to the predicted factor of three for this angle was indeed observed in the experimental data when compared to reported STED pulse energies and associated resolutions [22, 23]. The efficiency comparison of required *input* laser pulse energy (i. e. in the pupil plane) is left for the general discussion in Chapter 8.

#### 6.7.4 Recording speed and gating

The optimization of imaging time was not further investigated here because the camera use here limits frame rates to 30 ms per full-frame sensor readout. Significant technical progress has recently been made in the field of scientific complementary metal-oxide-semiconductor (sCMOS) cameras and intensified charge coupled device (iCCD), as well in the context of single-photon avalanche diode (SPAD) arrays [48]. While sCMOS technology is boosting available frame-rates and detection efficiency, the use of an iCCD or a SPAD array might additionally enable time-gated parallelized STED in the near future. Most recent STED implementations with serial sampling use a fast point detector that provides time-gated detection [59]. Time-gating is a powerful means to discard spontaneous fluorescence that occurs before the STED pulse has left. It thereby reduces background haze due to early photons, which increases the signal-to-noise ratio in the superresolution image. Besides camera speed, the number of scanning steps to sample the unit cell determines the recording speed. The size of the STED pattern unit cell has as lower limit the (Abbe-) resolution  $d$  of the microscope of  $d \approx 250$  nm. To attain a STED superresolution of 25 nm, the Nyquist-Shannon sampling theorem [56] (see also e. g. [42]), demands at least  $2 \cdot (250/12.5) = 400$  scanning steps, or equivalently 100 steps to attain 50 nm resolution. Thus, pixel-resolution can be traded quadratically against imaging speed.



## PARALLELIZATION BY A DIFFRACTIVE OPTICAL ELEMENT

---

### 7.1 MOTIVATION AND OVERVIEW

The implementation of parallelized STED discussed in the previous chapter served as a promising proof-of principle for the feasibility of high-resolution, massively parallelized STED nanoscopy. Nonetheless, the superresolved field of view was still rather small due to the limitation of available laser power. It therefore remains to investigate regimes of tighter fringe patterns that permit larger fields of view as a consequence of a higher energy efficiency (cf. Section 5.5). It was however not reasonable to choose significantly larger beam angles due to geometric constraints in the interferometric assembly. Overall, the comparably complex optical arrangement required a long beam path, and the alignment proved to be rather involved and unstable. Also bearing in mind that minor polarization degradation can deteriorate the STED zeros, a reduction of optical elements and a shorter beam path is clearly advantageous. Therefore, a complete redesign was undertaken aiming at improving the stability, efficiency and compactness of the setup. At the same time, the number of optical elements was reduced to a minimum. In this implementation, not single mirror is required in the beam path of the STED laser. The core part of the new setup is a diffractive optical element (DOE), a 2d binary phase grating that splits the STED laser beam efficiently into four identical copies. Details on the theory of the diffraction at 1d binary phase grating and its generalization to a 2d DOE can be found in Appendix E. Together with a segmented phase plate to rotate the polarization, the *DOE-STED* approach replaces the interferometer assembly used in the previous setup. Additionally, the emCCD camera detector was replaced by a scientific complementary metal-oxide semiconductor (sCMOS) camera with higher effective quantum efficiency and higher maximum frame rate. Experimental control and post-processing remain in large part identical.

### 7.2 SETUP COMPONENTS

The STED beam-path, using the same laser (Onefive, Katana HP, prototype) as the previous setup, is considerably simplified, see Figure 22. A two-lens (Qioptiq, AC16, AC200) Keplerian telescope, denoted as beam expander lenses (BEL), produces a collimated Gaussian beam of 2.7 mm FWHM diameter. The beam is split into four

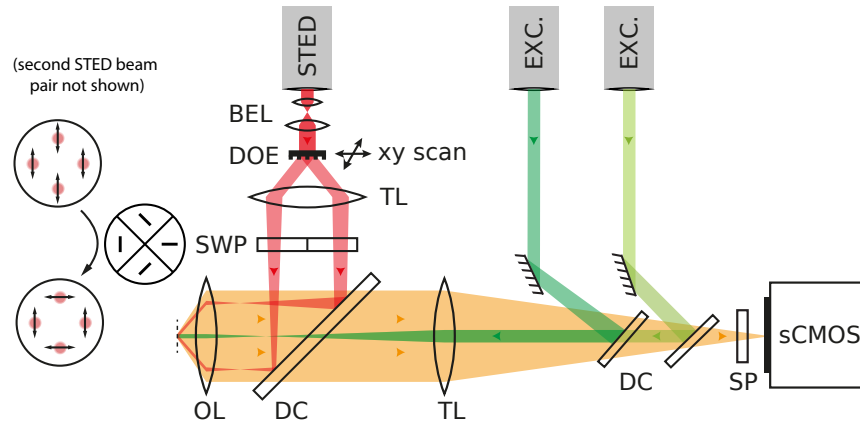


Figure 22: DOE-STED implementation featuring dual-color imaging capability. Note that *all* components in the STED beam path are shown.

identical beam by a two-dimensional diffractive optical element (DOE) (custom made, MPI for the Science of Light). The DOE used in this work has an effective period of  $36.5\ \mu\text{m}$ , which is de-magnified by a factor of  $M = f_{\text{TL}}/f_{\text{OL}} = 125$  to  $291\ \text{nm}$ . The tube lens (TL) was chosen to yield this small fringe period for high switch-off efficiency (cf. Section 5.5). The DOE sits in the focal plane of a simple tube lens substitute (Qioptiq, AC250) that casts the beams, after being reflected off a dichroic (DC) beam splitter (AHF Analysentechnik, custom made  $720\ \text{nm}$  short-pass), into the pupil of an objective lens (OL; Leica Microsystems, APO 100x/1.44 OIL; custom-built sample mount [22] clamped directly onto the objective). Both lenses constitute a stripped-down microscope arrangement in 4f-configuration with the DOE in its intermediate image plane. Correct beam polarization is achieved by a segmented wave plate (SWP) (custom made easySTED phase plate, as reported in [51]). All unwanted diffraction orders are blocked. To implement a scanning mechanism, the DOE is clamped to a two-axis scanning stage: a dynamic short-range ( $40\ \mu\text{m}$ ) piezoelectric actuator (Physik Instrumente, P-845P40) with custom-build driver electronics (DKFZ electronics workshop) and a custom-build flexure hinge to stabilize the one-axis motion are mounted on a long-travel ( $5\ \text{mm}$ ) linear stage with voice coil drive (Physik Instrumente, PIMag V-522 with controller C-413.2G)

The excitation source is – like in the setup described in the previous chapter – a super-continuum laser (Fianium, FemtoPower HP 1060 SC). Two wavelengths of about  $580\ \text{nm}$  and  $640\ \text{nm}$  are extracted from the broadband laser source using spectral filters and coupled into optical single-mode fibers (Thorlabs, P3-488PM-FC-2 and Schäfter+Kirchhoff, two times 60FC-4-M15 and 60FC-4-M20) that clean up the spatial beam profile. The excitation light joins the common beam path on the detection side by reflection off a notch filter (Semrock,  $594\ \text{nm}$  and  $658\ \text{nm}$  StopLine single notch filter). The notch filters are get-

ting abused here as dichroic beam splitters (DC), being angled at around  $15^\circ$  and  $30^\circ$  in order to spectrally align the reflected notch wavelengths to the narrow excitation bands. This minimally invasive configuration maximizes the fluorescence photon transmission to the detector. Note that this simple arrangement suffices mainly because the widefield excitation scheme is uncritical to minor aberrations introduced by the notch filter in reflectance. As in the previous setup, the pulse trains are coarsely synchronized by cables and fine-tuned via a custom-made electronic delay line. The STED laser is trigger master when paired with the laser diode, and trigger slave in conjunction with the super-continuum laser source for excitation. The fluorescence signals are imaged onto an sCMOS camera detector (Hamamatsu, ORCA-Flash 4.0 V2). A camera pixel in the intermediate image plane corresponds to a  $65 \text{ nm} \times 65 \text{ nm}$  square in the sample plane. Finally, the STED light is blocked from the detection using two short-pass (SP) filters (Semrock, BrightLine 775/SP).

### 7.3 SCANNER

The grating structure of the DOE is projected from the intermediate image plane onto the focal plane of the microscope, where it forms an orthogonally crossed sinusoidal fringe pattern. Although being a spatially filtered image, it contains the basic (frequency-doubled) grating features. The fringe pattern can thus be scanned by moving the DOE. According to Fourier theory, a translation of the DOE introduces a relative phase shift in the output beams, which in turn shifts the interference pattern in the focal plane. Thus, the same linear, slightly diagonal scanning scheme as in the implementation presented in Chapter 6 can be applied: a high-force actuator moves the DOE one period ( $36.5 \mu\text{m}$ ) vertically, while the horizontal axis travels 20-30 periods ( $\approx 1 \text{ mm}$ ); both with a precision of better than  $1 \text{ nm}$  (e. g. a quarter of a sampling step). Notice that the DOE needs careful rotational alignment to the scanning axis to avoid axis crosstalk. While a crosstalk compensation could be implemented in the experimental control software that commands the axis actuators, a proper hardware alignment eases the subsequent alignment procedure. Therefore, the DOE is clamped to a custom-made, lightweight rotational mount that connects to the specially designed flexure hinge, which in turn interlinks the actuators.

### 7.4 MEASURES FOR IMPROVED ROBUSTNESS

The microscope performance depends crucially on the stability of the optical assembly. Although some of the measures to improve the stability might appear trivial, they still are noteworthy inasmuch as they collectively contribute to the robustness of the system. As a result,

the optical setup was found to be stable for several weeks without the need for a re-alignment. The main implemented contributors to the increased system stability:

**SAMPLE HOLDER:** The custom-made sample holder, described in [22], clamps directly to the objective lens. Its direct and short mechanical connection from the lens to the microscopy sample reduces the mechanical and thermal drift.

**REDUCED NUMBER OF DEGREES OF FREEDOM:** The beam path of the STED laser is designed with a particularly low number of optical elements. Although this is not a figure of merit in itself, it serves two purposes: first, all optical elements, including mirrors, tend to alter the beam polarization state to some extent, which can have crucial effects on the STED performance. Second, this measure it helps to reduce the number of optical elements, the degrees of freedom and the total beam path length, all of which is beneficial to reduce (thermal) drift for long-term stability. All larger components, including the laser head, are coarsely moved into place by hand and then bolted to the optical table for a sturdy connection. All lenses, including the objective lens, sit in xy-translational mounts for the final adjustment procedure.

**RUGGEDIZED LENS MOUNTS:** Fine alignment of the STED beam is achieved by shifting the lenses, which sit in xy-translational lens mounts (Qioptiq, Centering Mounting Plate/Holder 25). To increase the stability, the mounts are secured with screws from all four sides in the final position.

**OBJECTIVE LENS MOUNT:** The objective lens needs to be secured very firmly, because it experiences all forces and torques transmitted from the sample holder every time the sample is changed. To this end, it sits in a custom modification of a xy-translational mount that allows fine, jaw-reduced adjustment and a robust locking mechanism.

**FIBER COUPLING:** The excitation light sources are fed into single-mode fibers, which clean up the laser mode and keep the subsequent beam path short. Both excitation channels are sourced from the same white-light laser source. The fibers therefore help to decouple the spectral filtering that is realized prior to the fiber from the beam alignment behind the fiber.

**BASEMENT:** The optical arrangement is vibrationally decoupled from the environment by a heavy, air-damped optical table, which stands directly on the concrete floor in the basement, where vibrations are usually low in the first place.

## 7.5 RESULTS

## 7.5.1 Parallelized STED with more than 10 000 zeros

The STED beams interfere at an angle of  $\theta = 61^\circ$ . According to Equation (82), the STED pulse energy is used 18-fold more efficiently than in dSTED and 4.5-fold more efficiently than in the interferometric STED parallelization presented in Chapter 6. Furthermore, the transmission efficiency in the STED beam path from laser head to pupil plane could be increased from 41 % in the interferometric parallelization to 55 % in the simplified DOE approach. The new setup comprises 13 000 STED zeros, of which 4160 are located inside the FWHM of the Gaussian STED-beam envelope (denoted as “inner region”) of 21.2  $\mu\text{m}$ . All results shown are scanned on a  $20 \times 20$  grid with 14.5 nm pixel size in the sample plane. The 400 required camera frames were recorded at 100 frames per second.

## 7.5.2 30 nm resolution on a large field of view

The resolution was assessed by imaging dark red fluorescent microspheres (Thermo Fisher) of 28 nm in diameter as shown in Figure 23. For this purpose, the fluorescent beads were dispersed on a poly-L-lysine-coated cover glass and embedded in Mowiol. The fluorophores

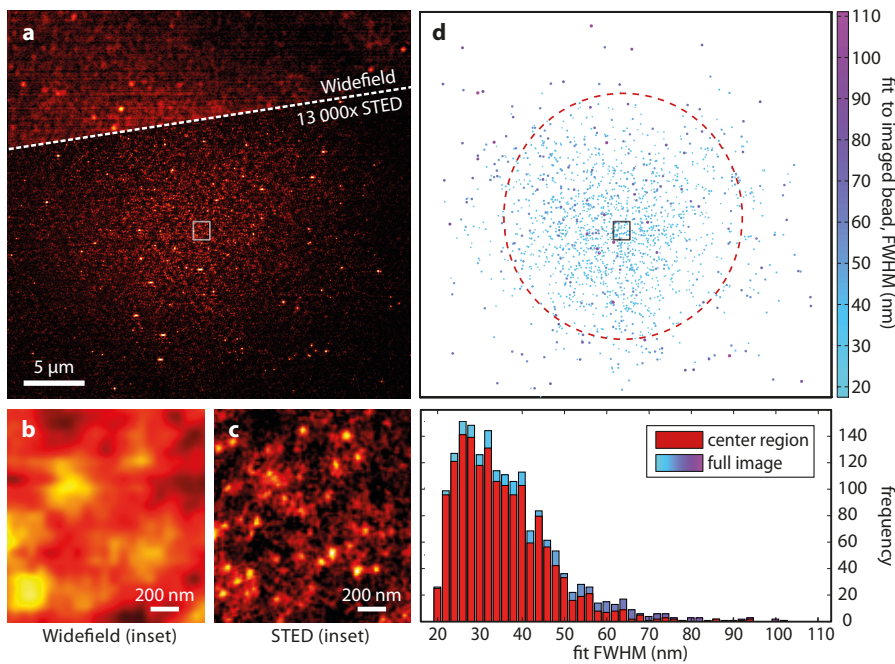


Figure 23: Resolution quantification. (a-c) Parallelized STED image vs. widefield image of 28 nm dark red beads with magnified inset. (d) Result of bead FWHM fit as color-coded scatter plot. (e) Histogram of the fit values in (d).

were excited at 640 nm with a pulse energy of 530 pJ, and the STED pulse energy was 2000 nJ at a pulse repetition rate of 1 MHz. This parameter combination translates to a pulse energy per unit cell of 0.18 nJ in the center. The superresolved bead image and the corresponding widefield image are displayed in Figure 23 (a-c). The superresolved image was modestly convoluted with a 2d Gaussian function of 1.4 pixels FWHM for a smoother display. Note that while single beads exhibit an expectedly round shape, bead clusters show a peculiar asymmetry. It could be speculated that, since peak intensities are not lower than in the dSTED case, an increased dark-state buildup takes place mainly in the scanning direction. Figure 23 (d) shows a scatter plot of a two-dimensional Gaussian fit to the superresolved beads. The bead diameter (FWHM) fit values are condensed to a histogram plot in Figure 23 (e), where the “inner region” in red comprises the 21.3  $\mu\text{m}$ -large (FWHM) diameter area of the Gaussian STED beam envelope. The disjoint “outer region” is added on top with a color-coding that corresponds to the color-map of the scatterplot. In the inner region, the beads averaged to a diameter (FWHM) fit value of 33 nm (median over 2000 different bead fits) and the corresponding FWHM fit value for the outer region was 43 nm. The resolution limit of the present implementation can be deduced from a model calculation that takes the geometrical bead size into account: it is slightly less than 30 nm for the inner region and around 40 nm for the outer region.

### 7.5.3 *Dual-color cell structure imaging*

The DOE-STED setup was further assessed by imaging a cytoskeleton staining in MeOH-fixed Vero cells. Microtubules and vimentin intermediate filaments were immunostained with the STED-compatible dyes STAR600 [41] and STAR635P (Abberior). The former was excited with 840 pJ pulse energy in the “green” 590 nm excitation wavelength channel, the latter with 1700 pJ in the “red” 640 nm channel. The excitation bands of both dyes are well-separated and exhibited negligible spectral crosstalk. The color-channels were imaged back-to-back by excitation-multiplexing in 4 s per channel. The considerable resolution gain is shown in Figure 24. While the filament structures are considerably blurred in the widefield reference image, they are well-separated in the superresolved recording with only minor resolution degradation towards the edges of the 33  $\mu\text{m}$ -sized field of view. The same gentle smoothing filter as in the last section was applied to the superresolved image.

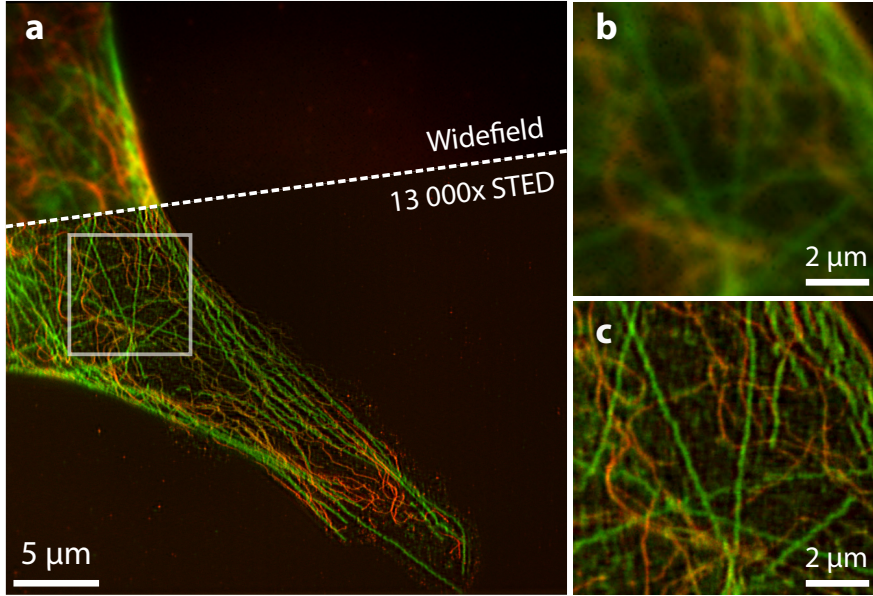


Figure 24: Dual-color recording of immunostained microtubules (green color-map) and vimentin (red color-map) intermediate filaments with magnified insets.

## 7.6 DISCUSSION

### 7.6.1 100-fold faster image acquisition on a large field of view

The STED images in this chapter were recorded with considerably increased imaging speed: 100 frames of 13 000 pixels are recorded per second. A standard dSTED implementation registers 10 000 to 33 000 pixels per second [22, 23]. This amounts to an overall 40- to 130-fold increased image acquisition, which means that video-rate STED on large fields of view seems to come within reach.

### 7.6.2 Square-root resolution scaling reconfirmed

The resolution depends on the local strength  $s(r) = I(r)/I(0)$  of the Gaussian envelope (according to Equation (65)) of the STED beam. Inserted into the square-root dependence (Equation (62)), we can expect a resolution scaling

$$d(r) = d_{\text{Abbe}} s^{-1/2} = d_{\text{SR}} \exp\left(\frac{1}{2} \frac{r^2}{(w/2)^2}\right) = d_{\text{SR}} \exp\left(\frac{r^2}{(\sqrt{2} w/2)^2}\right), \quad (87)$$

where  $r$  is the radial distance from the center of the Gaussian envelope,  $w$  its FWHM value,  $d_{\text{Abbe}}$  the Abbe resolution limit and  $d_{\text{SR}}$  the resolution at  $r = 0$ . Equation (87) illustrates that the resolving capability is almost constant in the center, reduces by a factor of square-root

of two at the FWHM value of the STED envelope, and deteriorates rapidly in the periphery. To illustrate the resolution scaling and to re-confirm the square-root law, the fit values from Figure 23 are grouped in 35 histogram bins according to their radial distance  $r$  in Figure 25. The solid line is not a fit, because the parameter  $d_{SR} = 30$  nm is al-

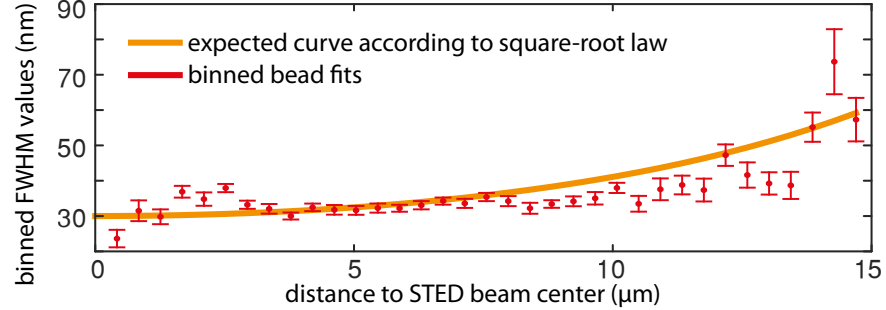


Figure 25: Resolution scaling reconfirms the square-root law.

ready pinned down by the bead fit average value and the STED beam width  $w = 21.3$   $\mu\text{m}$  is a preconfigured constant determined by the chosen STED beam expansion.

### 7.6.3 Energy efficiency advantage validated

The efficiency scaling according to Equation (82) and Figure 15 in Chapter 5 predicts an 18-fold reduced STED pulse energy requirement. Recent publications suggest that 7 nJ pulse energy are needed in dSTED to achieve 20 nm resolution [22, 23], or 3.1 nJ for 30 nm according to the square-root dependence (74). The present study attained 30 nm resolving power with 0.18 nJ pulse energy per central zero. The efficiency increase  $3.1 \text{ nJ}/0.18 \text{ nJ} = 17.2$  deduced from experimental data is in excellent agreement with the predicted value and confirms that the theoretical derivations of Chapter 5 indeed translate into experimental findings.

## CONCLUSION AND OUTLOOK

---

The present study has shown that massively parallelized STED nanoscopy on large fields of view is feasible without sacrificing highest resolution. In particular, a field of view of  $33\ \mu\text{m}$  edge length could be imaged within only four seconds with a resolution in the range of  $30\ \text{nm}$  and more than 13 000 zeros in parallel. While it was not a main objective of the present work, the imaging speed obtained for surpasses pSTED setups approximately 100-fold for a large field of view. Compared to previous attempts to parallelize STED [66], the degree of parallelization was boosted over two orders of magnitude from 100 zeros to 13 000 zeros. This achievement is a major step towards video-rate STED imaging of whole cells.

The high degree of parallelization might surprise at first sight because the proportional upscaling of single-point STED pulse energies would yield prohibitively large laser powers. The present work points out the main factors that account for this large increase:

**LASER REPETITION RATE AND LASER POWER:** The STED pulse energy is the crucial parameter for achieving the desired resolution increase (cf. Section 5.2). The STED laser prototype used in this thesis features an exceptionally high pulse energy. Since it runs at only 1 MHz pulse repetition rate, the pulse energy is 20-fold higher at the same average power when compared to typical STED lasers running at 20 MHz [23]. Additionally, the average laser power was higher than usual, yielding another factor of about four (2 W vs. 500 mW). The slower probing rate increases the acquisition time, but not necessarily in proportion to the slower rate: previous studies suggest that a rather low repetition rate in the range of 1 MHz reduces photobleaching and increase the fluorescence yield per excitation cycle eight-fold to 30-fold due to less triplet or dark state accumulation [18, 19].

**RESOLUTION TRADEOFF:** A state-of-the-art STED configuration typically achieves around 20 nm resolving power [22, 23]. According to the square-root scaling law derived in Section 5.2, the 30 nm resolving power in this study “saves” a factor of four at the expense of highest STED resolutions.

**RESOLUTION IN THE PERIPHERY:** The STED beam intensity envelope and alongside the resolving power decreases towards the edges of the field of view (cf. Section 7.6.2). This is not a desired effect, but rather a consequence of the deliberate choice

to use a Gaussian beam profile. While the resolution degrades only mildly with the square-root of the intensity, the degree of parallelization increases considerably. In many cases, a slightly reduced resolving power in the periphery of the image might be acceptable. If this is not the case, it still adds peripheric information at no cost to a central field of view having the highest resolving power. This property of Gaussian-beam powered parallelization implementations resembles the structure of the human eye with a sharp central spot and lower-resolution peripheral sight.

**BEAM PATH EFFICIENCY:** The STED beam path was designed with the least possible number of elements and high transmission efficiency in mind. I speculate that it is 1.5-fold more efficient than typical single-point scanning systems.

**EFFICIENCY ADVANTAGE OF THE PARALLELIZED STED PATTERN:** A careful analysis of the focus field formation in Chapter 3 and Chapter 5 culminates in Equation (82). It reveals that the parallelized STED pattern used in Chapter 7 uses the pulse energy 18-fold more efficiently than in a serial STED implementation, which is indeed confirmed by the experimental data.

*Explanation of  
energy efficiency  
increase*

The limiting value for the tightest possible grid of zeros (i. e. for  $\theta = \alpha$ ) yields a 37-fold increase in pulse energy efficiency (cf. Equation (82) in Section 5.5). This factor can be broken down into three interlinked contributions. Firstly, neighboring zeros share the intensity peak between them (cf. Figure 14). This accounts coarsely for a factor of six. Secondly, the standing-wave interference pattern allows a steeper zero confinement than a single donut due to the increased content of large lateral spatial frequency (cf. Section 5.3 ). This accounts for a factor of around 2.5. Thirdly, the “obliquity factor” that “squeezes” oblique beams to a higher intensity as illustrated in Section 4.5.2 contributes a factor of up to 2.5. Note that the limiting value of 37 might not be feasible to implement due to clipping of the beam incident on the rim of the aperture stop. The image quality still suffers from three shortcomings of the current camera detector technology compared with single-pixel detectors like an *avalanche photodiode* (APD). A state-of-the-art APD exhibits a thousand-fold lower readout- and dark-count noise (1.5 photons readout-noise per pixel and readout in the case of an sCMOS camera detector versus 0.001 dark-counts and virtually no readout noise for an APD in photon-counting mode). However, promising progress in camera technology within recent years nourish the expectation that the gap will potentially become smaller in the near future.

*Image quality*

*Detector noise*

*Gating*

The second image quality shortcoming is the lack of gating capability. As discussed in Section 6.7, most current STED nanoscopes that

use a single-pixel detector (e. g. an APD) implement gating to discard photons that do not stem from the superresolved region.

Although a time-gated detection on the 100 ps-level is not yet adequately implemented in multi-pixel camera technology, it might become available soon considering recent developments in the field.

The third shortcoming regarding image quality is the absent sectioning capability. Confocal microscope systems that are typically the basis for single-point STED implementations block photons stemming from out-of-focus regions by a pinhole. This is not possible for a massively parallelized STED implementation because all image regions that are cast on the camera sensor contain the superresolved signals and no area can be blocked. Two established microscopy modalities are promising candidates to eliminate this shortcoming when paired with the parallelized STED approach: firstly, *light-sheet microscopy* illuminates solely the focal plane with an excitation light-sheet. However, it typically requires a second, obliquely arranged objective lens to establish the light-sheet, which restricts the numerical aperture of the detection objective for geometric reasons. Secondly, *total internal reflection fluorescence* microscopy (TIRF) employs an oblique excitation beam that penetrates a sample region of lower refractive index as evanescent wave. Therefore, only the first  $\approx 200$  nm behind the refractive index can be excited, which typically results in high-contrast images. Interestingly, the STED beam angle in the DOE-STED setup matches exactly the critical angle of a cover-glas-aqueous-media interface, hence the STED light itself is already in TIRF-mode for this condition. As an implication of the *Fresnel equations*, the evanescent beam intensity is up to four times stronger (for s-polarized light) than the incident intensity. In addition to providing sectioning capability, the STED pulse energy and alongside the superresolved image size is increased by another factor of four. With a minor change in the uncritical excitation beam path to excite the sample in TIRF mode as well, the TIRF modality is readily available in the DOE-STED setup. This scenario heralds a field of view of  $60 \mu\text{m}$  at potentially  $30 \text{ nm}$  resolution, with more than 50 000 zeros in parallel. Consequently, DOE-STED could enable live-cell imaging of features near or at the membrane of whole cells at the nanometer scale in the near future.

*Sectioning capability*

*Light-sheet  
microscopy*

*TIRF*



## APPENDIX





## PUBLICATIONS AND CONTRIBUTIONS

---

### PUBLICATIONS AND POSTER PRESENTATIONS

- [1] F. Bergermann, L. Alber, S. J. Sahl, J. Engelhardt, and S. W. Hell. "2000-Fold Parallelized Dual-Color STED Fluorescence Nanoscopy." In: *Optics Express* 23.1 (2015).
- [2] F. Bergermann, L. Alber, S. J. Sahl, J. Engelhardt, and S. W. Hell. "Parallelized STED Nanoscopy." Poster presented at: Focus on Microscopy. Göttingen, 2015.
- [3] F. Bergermann, L. Alber, S. J. Sahl, J. Engelhardt, and S. W. Hell. "Parallelized STED Nanoscopy." Poster presented at: Seeing is Believing – Imaging the Processes of Life. EMBL Heidelberg, 2015.

### USE OF PUBLISHED MATERIAL

With written consent of *OSA Publishing*, I used material from the first-author publication [6]. The published manuscript as well as its refinement for this thesis was written by myself, with contributions to a first draft of the paper manuscript from Lucas Alber. I acknowledge valuable discussions, proof-reading and annotations by Steffen Sahl, which substantially improved the quality of the final manuscript.

### CONTRIBUTIONS TO THE PUBLISHED ARTICLE

STEFAN HELL conceived the idea and provided guidance. He convinced the company Onefive GmbH to design the custom-built STED laser with exceptionally high pulse energies that was a pivotal element for my thesis.

LUCAS ALBER worked with me in the course of his Master's thesis on implementing the interferometric STED parallelization presented in Chapter 6. I acknowledge his excellent contributions for improving and aligning the optical setup, for bead sample preparation and for imaging test-samples.

JOHANN ENGELHARDT contributed exhaustive lab-expertise to any topic on a daily basis.

STEFFEN SAHL helped me produce a high-quality paper manuscript.

ELLEN ROTHERMEL provided the biological samples.



## NUMERICAL CONSIDERATIONS AND SAMPLING

The term  $R := |\mathbf{r} - \mathbf{r}'|$  requires some extra attention. Large variations over the integration range of  $\mathbf{r}'$  lets the phase  $kR$  in the phase factor  $e^{i k R} = e^{i 2 \pi R / \lambda_n}$  in Equation (53) oscillate rapidly, which requires a fine sampling grid  $\Delta x'$  for the evaluation of the diffraction integral. Here I derive a sampling condition based on the requirement that each full  $(2\pi)$  phase oscillation shall be sampled with at least  $N_s$  points. Therefore, each phase step  $\Delta\varphi$  must fulfill

$$\Delta\varphi := k \Delta R = k \frac{dR}{dx'} \Delta x' \stackrel{!}{\leq} \frac{2\pi}{N}, \quad (88)$$

where the radius of the integration range  $f \text{ NA}$  is divided into  $M$  equidistant steps

$\Delta x' = f \text{ NA} / M$  and  $dR/dx'$  is the total derivative of  $R$  with respect to  $x'$ . Using  $r'^2 = f_n^2$ ,  $\mathbf{r} = (\mathbf{r}_\perp, z)$  and  $\mathbf{r}' = (\mathbf{r}'_\perp, z')$ ,  $R$  can be written as:

$$R = |\mathbf{r} - \mathbf{r}'| = \sqrt{f_n^2 + r^2 + 2(\mathbf{r}_\perp \cdot \mathbf{r}'_\perp + z z')} . \quad (89)$$

Since  $\mathbf{r}'$  is sampled on a sphere,  $z'$  depends on  $\mathbf{r}'_\perp$ . Explicitly,  $z'$  is  $z' = \sqrt{(f_n^2 - \mathbf{r}'_\perp^2)}$ . Hence, the total derivative reads

$$\frac{dR}{dx'} = \frac{\partial R}{\partial x'} + \frac{\partial R}{\partial z'} \frac{dz'}{dx'} = \frac{x - z x' / z'}{R} = \frac{x + z \tan \theta'}{R}, \quad (90)$$

where  $\tan \theta' = -x' / z'$ , and  $|\theta'| < \alpha$  (cf. Figure 12). Equation (90) indicates that the variation of  $R$  scales in the vicinity of the focus (i. e.  $R \approx f_n$ ) linearly with  $x$  and  $z$ . The highest spatial frequency oscillations occur where the term  $z \tan \theta'$  has its largest value. This is the case at the periphery of the integration sphere, furthest away of to the coordinate vector  $\mathbf{r}$ .

A slight undersampling might therefore be uncritical as long as  $|x| \gg z \tan \alpha$ . If field strengths are evenly distributed over the full integration range, the diffraction pattern in the focal region is usually confined to a narrow spatial extent. Therefore, undersampling only occurs at the periphery of the field of view (i. e. for large  $|x|$ ), where the intensity is relatively low anyways. On the other hand, if, for example, a Gaussian beam with small beam waist on the optical axis is under consideration, the effective aperture is small and relaxes the sampling condition as well. Only small Gaussian beams at the periphery of the pupil plane enforce the numerical sampling condition strictly.

The sampling requirement is dictated by the maximum absolute value of the total derivative  $dR/dx'$ , which can be approximated as

$$\left| \frac{dR}{dx'} \right| \leq \max \left\{ \left| \frac{dR}{dx'} \right| \right\} \approx \frac{|x| + |z| \tan \alpha}{f}, \quad (91)$$

*The  $y'$  component is treated in exactly the same manner and thus the abbreviation  $\mathbf{r}'_\perp := (x', y')$  is used.*

for the usual case  $r \ll f_n$  and thus  $R \approx f_n$ . Feeding Equation (91) into Equation (88) and solving for the number of sampling steps  $M$  yields

$$M \geq N_s (|x| + |z| \tan \alpha) \frac{NA}{\lambda_0}, \quad (92)$$

which was previously derived in [44] for  $x = 0$  and  $N_s = 2$ .

## RANGE OF VALIDITY OF THE DEBYE APPROXIMATION

The exponential term  $e^{i k R}$  in the un-approximated diffraction integral 48 in Section 4.2 oscillates rapidly for large optical frequencies  $e^{i k R} = e^{i 2 \pi R / \lambda_n}$  if  $r$  is not very close to the focal point. For  $r / f_n \ll 1$ , we can motivate a Taylor expansion around the focal point value  $R = f_n$ :

$$R = |\mathbf{r} - \mathbf{r}'| = f_n \sqrt{1 - 2 \frac{\mathbf{r}' \cdot \mathbf{r}}{f_n^2} + \frac{\mathbf{r}^2}{f_n^2}}, \quad (93)$$

where  $\mathbf{r}'^2 = f_n^2$  was used. The Taylor expansion  $\sqrt{1 + \varepsilon} = 1 + \varepsilon/2 - \varepsilon^2/8 + \mathcal{O}(\varepsilon^3/16)$  with

$$\varepsilon = -2 \frac{\mathbf{r}' \cdot \mathbf{r}}{f_n^2} + \left(\frac{r}{f_n}\right)^2 \quad (94)$$

yields

$$\frac{R}{f_n} = 1 - \frac{\mathbf{r}' \cdot \mathbf{r}}{f_n^2} + \frac{1}{2} \left(\frac{r}{f_n}\right)^2 - \frac{1}{8} \left(-2 \frac{\mathbf{r}' \cdot \mathbf{r}}{f_n^2} + \left(\frac{r}{f_n}\right)^2\right)^2 + \mathcal{O}\left(\frac{\varepsilon^3}{16}\right) \quad (95)$$

$$= 1 - \frac{\mathbf{r}' \cdot \mathbf{r}}{f_n^2} + \frac{1}{2} \left(\frac{r}{f_n}\right)^2 - \frac{1}{2} \left(\frac{\mathbf{r}' \cdot \mathbf{r}}{f_n^2}\right)^2 + \mathcal{O}\left(\left(\frac{r}{f_n}\right)^3\right). \quad (96)$$

Using  $\mathbf{r}' \cdot \mathbf{r} / f_n^2 = \cos(\mathbf{r}, \mathbf{r}')$  and the identity  $1 - \cos^2(\cdot) = \sin^2(\cdot)$  yields

$$\frac{R}{f_n} = 1 - \frac{\mathbf{r}' \cdot \mathbf{r}}{f_n^2} + \frac{1}{2} \left(\frac{r}{f_n}\right)^2 \sin^2(\mathbf{r}, \mathbf{r}') + \mathcal{O}\left(\left(\frac{r}{f_n}\right)^3\right). \quad (97)$$

Therefore, the approximation is particularly good if  $\sin(\mathbf{r}, \mathbf{r}')$  is small, that is, if  $\mathbf{r}$  and  $\mathbf{r}'$  point in the same (or opposite) direction. In consequence, if  $\mathbf{r}$  points mainly into lateral direction, low spatial frequency content ( $\theta \approx 0$ ; center of pupil plane) shows a higher phase error. If  $\mathbf{r}$ , on the other hand, is directed mainly towards axial points, high frequency content ( $\theta \approx \alpha$ ) shows a larger phase error. In general the further  $\mathbf{r}$  diverges from the focal point, the larger the phase error gets. For a maximum tolerable phase error  $2\pi/N_s$ , the validity of the linear approximation is

$$\varphi_{\text{err}} \approx k f_n \frac{1}{2} \left(\frac{r}{f_n}\right)^2 \stackrel{!}{<} \frac{2\pi}{N_s}, \quad (98)$$

which implies

$$\left(\frac{r}{f_n}\right)^2 \leq \frac{\lambda}{2\pi} \frac{1}{f_n} 2 \frac{2\pi}{N_s} = \frac{2}{N_s} \frac{\lambda}{f_n}, \quad (99)$$

and therefore

$$r \leq \sqrt{2/N \lambda_0 f_0}. \quad (100)$$

For example,  $N = 8$ ,  $\lambda = 0.775 \mu\text{m}$ ,  $f_n = 2000 \mu\text{m}$  the maximum radius with less than  $1/N$  phase error in all integration points is  $r = 20 \mu\text{m}$ . For these values  $r/f_n < 1/100$  holds, indicating the validity of the square-root approximation. Note that this estimation is a conservative limit; points with the largest phase error will in most cases not contribute considerably. These regions usually belong to the highly oscillating portions of the phase exponent in the diffraction integral and therefore sum to almost zero.

## CODE FOR FOCUS FIELD CALCULATIONS

Listing 1: Implementation of *Fast focus field calculations*

```

%% **** Fast focus field calculations ****
% Leutenegger et al., Optics Express 2006,
% dx.doi.org/10.1364/OE.14.011277
% implementation and extension
% This is a minimal working example

%% **** Parameter input ****
% Calculation:
z = 0;
nM = 305; % pupil sampling steps: 2*nN + 1
nN = 2^15;
dx = 0.005; % lateral pixel width in sample plane / (um)

% Setup:
lambda = 0.775; % vacuum wavelength /(um)
nt = 1.518; % refractive index in sample medium
NA = 1.44; % numerical aperture
f = 2000; % focal length /(um)

% Derived:
R = f*NA; % pupil radius R = f*nt*sin(alpha) (sine condition)

%% **** Init grid and derived parameters ****
m = -nM:nM;
[M, N] = meshgrid(m); % sampling grid for pupil plane
[Xi, Yi] = meshgrid(m*R/nM); % sampling in pupil plane

k0 = 2*pi/lambda;
kt = nt*k0;
dk = k0*NA/nM; % = k0*nt*sin('alpha')/nM = kx_max/nM
dh = f*dk/k0; % sampling step in pupil plane

Kx = M*dk;
Ky = N*dk;
Kz = sqrt(max(0, kt^2-Kx.^2-Ky.^2)); % keep it real

Theta = asin(min(dk/kt*sqrt(M.^2+N.^2), NA/nt)); % dito
Phi = atan2(N,M); % Eqn. (11)

%% **** Windowing ****
% W reduces aperture rim discretization ringing artifacts,
% it smooths the binary step over 1/30 th of the full aperture

```

```

W = .5*(1+tanh(1.5/(R/30)*(R-sqrt(Xi.^2+Yi.^2)))); % Eqn. (16)

%% **** Input electric field ****
FWHM = 2*R; % (um) Pupil plane diameter = FWHM of Gaussian beam
vortex = exp(1i*Phi);
Ei = exp(-log(2)*((Xi).^2 + Yi.^2)/(FWHM/2)^2).* ...
(Theta<asin(NA/nt)); % NA/nt = sin(theta)
Ei = Ei.*vortex;
Ei(:,:,2) = 1i*Ei;
Ei(:,:,3) = 0; % note that this is an approximation!

%% **** Translate Ei to Et ****
% Lens action on E-field polarization vector
clear ep es ez etheta ephi er

% ** input base vectors **
ep(:,:,1) = cos(Phi);
ep(:,:,2) = sin(Phi);
ep(:,:,3) = 0;

es(:,:,1) = -sin(Phi);
es(:,:,2) = cos(Phi);
es(:,:,3) = 0;

ez(:,:,1) = zeros(size(Phi));
ez(:,:,2) = zeros(size(Phi));
ez(:,:,3) = ones(size(Phi));

% ** output base vectors **
etheta(:,:,1) = cos(Phi).*cos(Theta); % note that etheta
etheta(:,:,2) = sin(Phi).*cos(Theta); % is called er
etheta(:,:,3) = sin(Theta); % in the paper

ephi = es;

er(:,:,1) = -cos(Phi).*sin(Theta);
er(:,:,2) = -sin(Phi).*sin(Theta);
er(:,:,3) = cos(Theta);

% ** transform E-field vectors **
Et = bsxfun(@times, dot(Ei,ep,3), etheta) + ...
bsxfun(@times, dot(Ei,es,3), ephi) + ...
bsxfun(@times, dot(Ei,ez,3), er); % cf. Eqn. (4)

%% **** Calculate focus field ****
% 2 x 1d FFT is faster and less memory hungry than 1 x FFT2
% decorate with propagator, apodization and windowing function
E = bsxfun(@times, exp(1i*Kz*z)./sqrt(cos(Theta)).*W, Et);

E = fft(E, nN, 1); % FFT with zero-padding
E((nM+2):(end-nM),:,:) = []; % crop zero-padding

```

```

E = fft(E, nN, 2);           % FFT on second dimension
E(:,(nM+2):(end-nM),:) = []; % crop zero-padding

E = fftshift(fftshift(E,1),2);

Iout(:, :) = sum(abs(E).^2,3);
Iout = Iout*(R^2/(lambda*f*nM^2)).^2; % scaling as in Eqn. (12)

%% **** Output ****
figure, imshow(Iout./max(Iout(:)))

%% **** Intensity increase due to 'oblique' beam components
Iin = sum(abs(Ei).^2,3).*W.^2;
disp(['I_out/I_in: ' ...
num2str(sum(Iout(:))*dx^2/(sum(Iin(:))*dh^2),5)])

```

---



## DIFFRACTION AT A BINARY PHASE GRATING

The diffractive optical element used to parallelize STED nanoscopy in Chapter 7 is comparable to an overlay of two one-dimensional binary phase gratings. The following derivation is focused on finding conditions for the highest transmission efficiency in the four  $m = \pm 1$  diffraction orders.

### NORMALLY INCIDENT PLANE WAVE

Consider a binary transmission grating with pitch  $p$ , width of the binary step  $w < p$  and step height  $H$  in a material of refractive index  $n$ , as depicted in Figure 26. Let  $\Delta$  be the optical path length difference

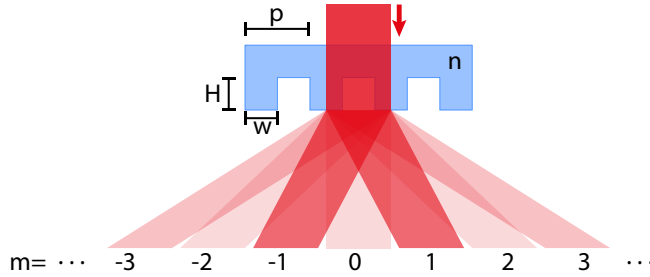


Figure 26: Diffraction at a binary grating.

given by

$$\Delta := (n - 1) H. \quad (101)$$

Let us assume that a plane wave characterized by the wave vector

$$k_\lambda := \frac{2\pi}{\lambda} \quad (102)$$

impinges normally onto the grating. The optical path length difference gives rise to a phase shift of  $e^{ik_\lambda \Delta}$ . Therefore, the grating transmission function on the period  $0 \leq x < p$  is given by:

$$T_p(x) := \begin{cases} e^{ik_\lambda \Delta} & 0 \leq x < w \\ 1 & w \leq x < p \end{cases}. \quad (103)$$

For convenience, let us use the symmetric and periodic version of the full binary grating  $T$ , which is shifted by  $p/2$  and reads:  $T(x) = T_p(x + p/2 \bmod p)$ . Due to its periodicity,  $T(x)$  can be expressed in terms of a Fourier series

$$T(x) = \sum_{m=-\infty}^{\infty} c_m e^{-ik_m x}, \quad (104)$$

with distinct diffraction orders  $m$  and diffraction directions  $k_m$ . The plane wave is thereby split into a series of plane waves with different amplitudes (Fourier coefficients)  $c_m$  that travel into direction  $\mathbf{k} = (k_m, \sqrt{k^2 - k_m^2})$ . The coefficients  $c_m$  are given by

$$c_m := \frac{1}{p} \int_0^p T(x) e^{-ik_m x} dx, \quad (105)$$

where  $k_m$  is defined as

$$k_m := \frac{2\pi}{p} m \quad (m \in \mathbb{Z}). \quad (106)$$

To compute the Fourier coefficients  $c_m$ , we evaluate the integral term in Equation (105). Adding a zero to the first term in Equation (103) (i.e.  $1 + (e^{ik_\lambda \Delta} - 1)$ ) and using the periodicity of  $T(x)$  to shift the integration limits by half a period yields

$$\begin{aligned} \int_0^p T(x) dx &= \int_0^p 1 e^{-ik_m x} dx + \int_{-w/2}^{w/2} (e^{ik_\lambda \Delta} - 1) e^{-ik_m x} dx \quad (107) \\ &= p \delta(m, 0) + (e^{ik_\lambda \Delta} - 1) \frac{1}{ik_m} [e^{ik_m w/2} - e^{-ik_m w/2}]. \end{aligned} \quad (108)$$

where we recognize the first term as Kronecker delta that is denoted by  $\delta(m, 0)$ . After some rearrangement, the second term in Equation (107) can be expressed in terms of the sinc-function that is defined as  $\text{sinc}(0) = 1$  and  $\text{sinc}(x) = \sin(\pi x)/(\pi x)$  otherwise. The Fourier coefficients thus read:

$$c_m = \delta(m, 0) + (e^{ik_\lambda \Delta} - 1) (w/p) \text{sinc}(m w/p). \quad (109)$$

In order to suppress the zero-order amplitude, we require:

$$1 + (e^{ik_\lambda \Delta} - 1) (w/p) \stackrel{!}{=} 0, \quad (110)$$

$$\implies e^{ik_\lambda \Delta} \stackrel{!}{=} 1 - (p/w) \quad (\in \mathbb{R}). \quad (111)$$

The lowest non-trivial solution for the complex exponential to become real is  $e^{ik_\lambda \Delta} = e^{i\pi} \Rightarrow \Delta = \lambda/2$ . Solving for  $H$  in Equation (101) and using Equation (110) one obtains

$$H = \lambda/(2(n-1)), \quad (112)$$

$$w = p/2. \quad (113)$$

Fed back into Equation (109), we obtain for the intensity  $I_m := |c_m|^2$  relative to the incoming intensity  $I_{\text{in}}$

$$\frac{I_m}{I_{\text{in}}} = \frac{4}{\pi^2} \frac{1}{m^2} \approx 0.41 \frac{1}{m^2} \quad (m \text{ uneven}), \quad (114)$$

Notice that Equation (109) implies that sinc-function in Equation (109) vanish for even  $m$ . This means, provided that relations in Equations (112) and (113) hold, 41 percent of the incident energy are distributed into the two lowest ( $m = \pm 1$ ) non-vanishing diffraction orders. A ninth of that value goes in the third orders, and a mere six percent into the fourth ones.

ARBITRARY INPUT WAVE

Let  $g(x)$  be an arbitrary (possibly complex) amplitude distribution incident on the grating. The grating  $T$  will alter the amplitude  $g$  to  $f = gT$ . The combined Fourier transform is

$$F(k) = \int f(x)e^{-ikx} dx = \int g(x) \left( \sum_m c_m e^{-ik_m x} \right) e^{-ikx} dx \quad (115)$$

$$= \sum_m c_m \int g(x) e^{-ik_m x} e^{-ikx} dx. \quad (116)$$

Thus, the Fourier transform is indeed an (infinite) sum of weighted (by  $c_m$ ) Fourier transforms, which are phase-shifted (by  $e^{-ik_m x}$ ) copies of the Fourier transform of  $g$  alone. Using that such a linear phase-shift under the integral equals a coordinate shift (by  $k_m$ ) in Fourier space, we can write Equation (115) as

$$F(k) = \sum_m c_m G(k + k_m), \quad (117)$$

where  $G(k)$  denotes the Fourier transform of  $g(x)$ . Note that this is a general property of any periodic function  $T$  that modulates an arbitrary function  $g$ : the grating splits the incident wave into deflection orders  $m$ , which are an exact copy of the original wave  $g$ , except for an altered amplitude  $c_m$  and propagation angle  $\varphi_m = \arctan(k_m/k_\lambda)$ .

GENERALIZATION TO A TWO-DIMENSIONAL PHASE GRATING

The grating theory for one-dimensional gratings generalizes straightforwardly to the two-dimensional case, because the two-dimensional Fourier analysis factorizes into two one-dimensional Fourier Transforms. Two noteworthy differences exist, however. First, the diffraction efficiency into the first diffraction orders (in two dimensions) reduces from a total of  $2 \times 40.5\% = 81\%$  to  $4 \times 16.4\% = 65\%$ , because the beam experiences diffraction into both spatial dimensions. Its strength is thus the product of the two one-dimensional diffractions according to Formula 114. Second, the fringe pattern in the sample plane is oriented diagonally to the underlying 1d grating structure symmetry. This can be understood by inspecting the symmetries of the real DOE diffraction pattern in Figure 27. While the 1d grating diffraction is oriented along the image axes, the interference fringes of the four first diffraction orders alone exhibits a symmetry diagonal to these axes. As a consequence, the “effective” grating period is enlarged by a factor of  $\sqrt{2}$  as compared to the 1d period.

Note further that since the zeroth diffraction mode is suppressed, the projected grating exhibits a spatial frequency doubling as compared to the a amplitude transmission grating with non-zero undiffracted beam strength.

*From a less formal point of view, a 2d grating is an orthogonal superposition of two 1d grating structures.*

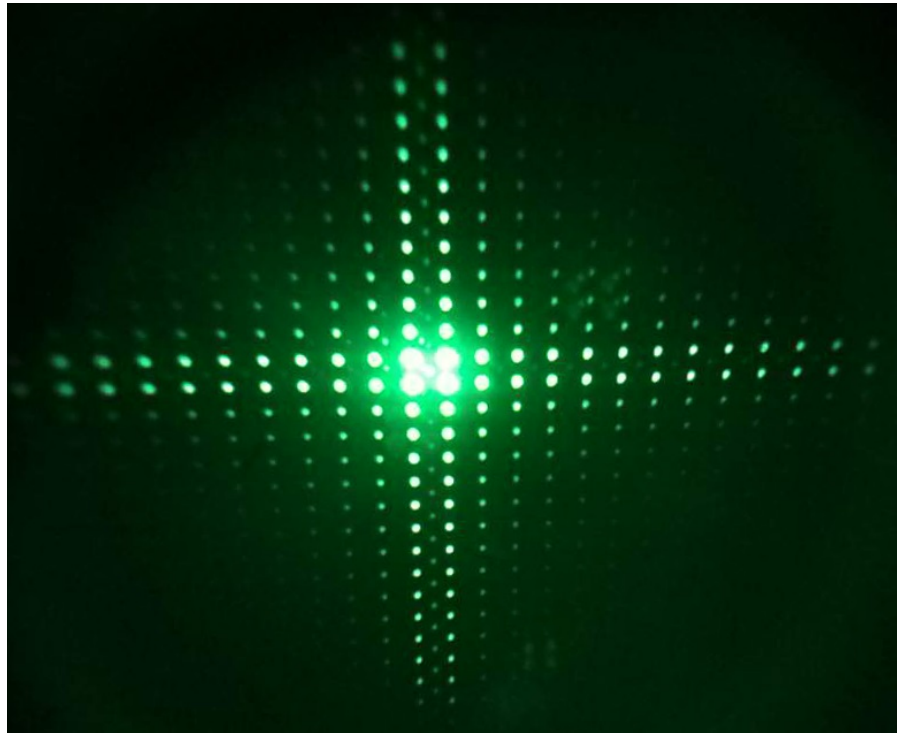


Figure 27: Photograph of the DOE diffraction pattern that was cast onto the ceiling. The picture was taken through an infrared viewer, highly saturating the preferred first diffraction orders to show the higher diffraction orders.

## BIBLIOGRAPHY

---

- [1] E. Abbe. "Beiträge zur Theorie des Mikroskops und der mikroskopischen Wahrnehmung." In: *Archiv für mikroskopische Anatomie* 9.1 (1873). DOI: [10.1007/BF02956173](https://doi.org/10.1007/BF02956173) (cited on pages [1](#), [3](#), [18](#)).
- [2] E. Abbe. "Ueber die Bedingungen des Aplanatismus der Linsensysteme." In: *Sitzungsberichte der Jenaischen Gesellschaft für Medicin und Naturwissenschaft* (1879) (cited on page [19](#)).
- [3] M. Abramowitz and I. A. Stegun, editors. *Handbook of Mathematical Functions: with Formulas, Graphs, and Mathematical Tables*. 9-*Revised* edition. New York: Dover Publications, 1965 (cited on page [13](#)).
- [4] G. Arfken and H. J. Weber. *Mathematical Methods for Physicists*. 6. ed. Amsterdam, Heidelberg [u.a.]: Elsevier Academic Press, 2005 (cited on page [15](#)).
- [5] B. B. Baker and E. T. Copson. *The Mathematical Theory of Huygens' Principle*. 2. ed., reprint. Oxford: Clarendon Pr., 1953 (cited on page [16](#)).
- [6] F. Bergermann, L. Alber, S. J. Sahl, J. Engelhardt, and S. W. Hell. "2000-fold parallelized dual-color STED fluorescence nanoscopy." In: *Optics Express* 23.1 (2015). DOI: [10.1364/OE.23.000211](https://doi.org/10.1364/OE.23.000211) (cited on pages [29](#), [39](#), [67](#), [87](#)).
- [7] S. Berning, K. I. Willig, H. Steffens, P. Dibaj, and S. W. Hell. "Nanoscopy in a living mouse brain." In: *Science* 335.6068 (2012). DOI: [10.1126/science.1215369](https://doi.org/10.1126/science.1215369) (cited on page [4](#)).
- [8] E. Betzig, G. H. Patterson, R. Sougrat, O. W. Lindwasser, S. Olenych, J. S. Bonifacino, M. W. Davidson, J. Lippincott-Schwartz, and H. F. Hess. "Imaging intracellular fluorescent proteins at nanometer resolution." In: *Science* 313.5793 (2006). DOI: [10.1126/science.1127344](https://doi.org/10.1126/science.1127344) (cited on pages [1](#), [3](#)).
- [9] P. Bingen, M. Reuss, J. Engelhardt, and S. W. Hell. "Parallelized STED fluorescence nanoscopy." In: *Optics Express* 19.24 (2011). DOI: [10.1364/oe.19.023716](https://doi.org/10.1364/oe.19.023716) (cited on page [5](#)).
- [10] R. E. Blahut. *Theory of Remote Image Formation*. Cambridge University Press, 2004 (cited on page [15](#)).
- [11] N. Bobroff. "Position measurement with a resolution and noise-limited instrument." In: *Review of Scientific Instruments* 57.6 (1986). DOI: [10.1063/1.1138619](https://doi.org/10.1063/1.1138619) (cited on page [4](#)).

- [12] M. Born and E. Wolf. *Principles of Optics: Electromagnetic Theory of Propagation, Interference and Diffraction of Light*. 6. (corr.) ed. Cambridge: Cambridge University Press, 1997 (cited on pages 17, 19).
- [13] J. Bückers, D. Wildanger, G. Vicidomini, L. Kastrup, and S. W. Hell. "Simultaneous multi-lifetime multi-color STED imaging for colocalization analyses." In: *Optics Express* 19.4 (2011). DOI: [10.1364/OE.19.003130](https://doi.org/10.1364/OE.19.003130) (cited on page 49).
- [14] A. Chmyrov, J. Keller, T. Grotjohann, M. Ratz, E. D'Este, S. Jakobs, C. Eggeling, and S. W. Hell. "Nanoscopy with more than 100,000 'doughnuts'." In: *Nature Methods* 10.8 (2013). DOI: [10.1038/nmeth.2556](https://doi.org/10.1038/nmeth.2556) (cited on pages 4, 5, 39).
- [15] J. G. Danzl, S. C. Sidenstein, C. Gregor, N. T. Urban, P. Ilgen, S. Jakobs, and S. W. Hell. "Coordinate-targeted fluorescence nanoscopy with multiple off states." In: *Nature Photonics* 10.2 (2016). DOI: [10.1038/nphoton.2015.266](https://doi.org/10.1038/nphoton.2015.266) (cited on page 4).
- [16] P. Debye. "Das Verhalten von Lichtwellen in der Nähe eines Brennpunktes oder einer Brennnlinie." In: *Annalen der Physik* 335.14 (1909). DOI: [10.1002/andp.19093351406](https://doi.org/10.1002/andp.19093351406) (cited on pages 22, 25).
- [17] H. Deschout, F. C. Zanacchi, M. Młodzianoski, A. Diaspro, J. Bewersdorf, S. T. Hess, and K. Braeckmans. "Precisely and accurately localizing single emitters in fluorescence microscopy." In: *Nature Methods* 11.3 (2014). DOI: [10.1038/nmeth.2843](https://doi.org/10.1038/nmeth.2843) (cited on page 4).
- [18] G. Donnert, C. Eggeling, and S. W. Hell. "Major signal increase in fluorescence microscopy through dark-state relaxation." In: *Nature Methods* 4.1 (2007). DOI: [10.1038/nmeth986](https://doi.org/10.1038/nmeth986) (cited on page 61).
- [19] G. Donnert, J. Keller, R. Medda, M. A. Andrei, S. O. Rizzoli, R. Lührmann, R. Jahn, C. Eggeling, and S. W. Hell. "Macromolecular-scale resolution in biological fluorescence microscopy." In: *Proceedings of the National Academy of Sciences of the United States of America* 103.31 (2006). DOI: [10.3410/f.1033576.388825](https://doi.org/10.3410/f.1033576.388825) (cited on page 61).
- [20] M. Dyba and S. W. Hell. "Focal spots of size  $\lambda/23$  open up far-field fluorescence microscopy at 33 nm axial resolution." In: *Physical Review Letters* 88.16 (2002). DOI: [10.1103/physrevlett.88.163901](https://doi.org/10.1103/physrevlett.88.163901) (cited on page 30).
- [21] J. Fölling, M. Bossi, H. Bock, R. Medda, C. A. Wurm, B. Hein, S. Jakobs, C. Eggeling, and S. W. Hell. "Fluorescence nanoscopy by ground-state depletion and single-molecule return." In: *Nature Methods* 5.11 (2008). DOI: [10.1038/nmeth.1257](https://doi.org/10.1038/nmeth.1257) (cited on pages 1, 3).

- [22] F. Görlitz, P. Hoyer, H. Falk, L. Kastrup, J. Engelhardt, and S. W. Hell. "A sted microscope designed for routine biomedical applications." In: *Progress In Electromagnetics Research* 147 (2014). DOI: [10.2528/pier14042708](https://doi.org/10.2528/pier14042708) (cited on pages [41](#), [50](#), [51](#), [54](#), [56](#), [59–61](#)).
- [23] F. Göttfert, C. A. Wurm, V. Mueller, S. Berning, V. C. Cordes, A. Honigmann, and S. W. Hell. "Coaligned dual-channel sted nanoscopy and molecular diffusion analysis at 20 nm resolution." In: *Biophysical Journal* 105.1 (2013). DOI: [10.1016/j.bpj.2013.05.029](https://doi.org/10.1016/j.bpj.2013.05.029) (cited on pages [5](#), [51](#), [59–61](#)).
- [24] H. Gross, W. Singer, and M. Totzeck. *Handbook of Optical Systems: Physical Image Formation*. Volume 2. Wiley-VCH, 2005 (cited on pages [15](#), [24](#), [26](#)).
- [25] T. Grotjohann, I. Testa, M. Reuss, T. Brakemann, C. Eggeling, S. W. Hell, and S. Jakobs. "rsEGFP2 enables fast RESOLFT nanoscopy of living cells." In: *eLife* 1 (2012). DOI: [10.7554/eLife.00248](https://doi.org/10.7554/eLife.00248) (cited on page [5](#)).
- [26] M. G. L. Gustafsson. "Surpassing the lateral resolution limit by a factor of two using structured illumination microscopy." In: *Journal of Microscopy* 198.2 (2000). DOI: [10.1046/j.1365-2818.2000.00710.x](https://doi.org/10.1046/j.1365-2818.2000.00710.x) (cited on page [39](#)).
- [27] M. G. Gustafsson. "Nonlinear structured-illumination microscopy: wide-field fluorescence imaging with theoretically unlimited resolution." In: *Proceedings of the National Academy of Sciences of the United States of America* 102.37 (2005). DOI: [10.1073/pnas.0406877102](https://doi.org/10.1073/pnas.0406877102) (cited on page [39](#)).
- [28] B. Harke, J. Keller, C. K. Ullal, V. Westphal, A. Schönle, and S. W. Hell. "Resolution scaling in STED microscopy." In: *Optics Express* 16.6 (2008). DOI: [10.1364/oe.16.004154](https://doi.org/10.1364/oe.16.004154) (cited on pages [4](#), [31](#)).
- [29] E. Hecht. *Optics*. 4 edition. Reading, Mass: Addison-Wesley, 2001 (cited on page [15](#)).
- [30] S. W. Hell. "Toward fluorescence nanoscopy." In: *Nature Biotechnology* 21.11 (2003). DOI: [10.1038/nbt895](https://doi.org/10.1038/nbt895) (cited on pages [3](#), [29](#), [31](#)).
- [31] S. W. Hell. "Far-field optical nanoscopy." In: *Science* 316.5828 (2007). DOI: [10.1126/science.1137395](https://doi.org/10.1126/science.1137395) (cited on page [3](#)).
- [32] S. W. Hell. "Microscopy and its focal switch." In: *Nature methods* 6.1 (2008). DOI: [10.1038/nmeth.1291](https://doi.org/10.1038/nmeth.1291) (cited on page [3](#)).
- [33] S. W. Hell. "Nanoscopy with focused light (Nobel lecture)." In: *Angewandte Chemie International Edition* 54.28 (2015). DOI: [10.1002/anie.201504181](https://doi.org/10.1002/anie.201504181) (cited on page [4](#)).

- [34] S. W. Hell and J. Wichmann. "Breaking the diffraction resolution limit by stimulated emission: stimulated-emission-depletion fluorescence microscopy." In: *Optics Letters* 19.11 (1994). DOI: [10.1364/OL.19.000780](https://doi.org/10.1364/OL.19.000780) (cited on pages 1, 4, 29).
- [35] S. T. Hess, T. P. K. Girirajan, and M. D. Mason. "Ultra-high resolution imaging by fluorescence photoactivation localization microscopy." In: *Biophysical Journal* 91.11 (2006). DOI: [10.1529/biophysj.106.091116](https://doi.org/10.1529/biophysj.106.091116) (cited on pages 1, 3).
- [36] M. Hofmann, C. Eggeling, S. Jakobs, and S. W. Hell. "Breaking the diffraction barrier in fluorescence microscopy at low light intensities by using reversibly photoswitchable proteins." In: *Proceedings of the National Academy of Sciences of the United States of America* 102.49 (2005). DOI: [10.1073/pnas.0506010102](https://doi.org/10.1073/pnas.0506010102) (cited on pages 1, 4).
- [37] C. Huygens. *Traité de la lumière: où sont expliquées les causes de ce qui luy arrive dans la reflexion, & dans la refraction, et particulièrement dans l'etrange refraction du cystal d'Islande*. Chez Pierre vander Aa, 1690 (cited on page 15).
- [38] J. D. Jackson. *Classical electrodynamics*. 2. ed. New York [u.a.]: Wiley, 1975 (cited on page 9).
- [39] T. A. Klar and S. W. Hell. "Subdiffraction resolution in far-field fluorescence microscopy." In: *Optics Letters* 24.14 (1999). DOI: [10.1364/OL.24.000954](https://doi.org/10.1364/OL.24.000954) (cited on page 1).
- [40] T. A. Klar, S. Jakobs, M. Dyba, A. Egner, and S. W. Hell. "Fluorescence microscopy with diffraction resolution barrier broken by stimulated emission." In: *Proceedings of the National Academy of Sciences of the United States of America* 97.15 (2000). DOI: [10.1073/pnas.97.15.8206](https://doi.org/10.1073/pnas.97.15.8206) (cited on page 1).
- [41] K. Kolmakov, V. N. Belov, J. Bierwagen, C. Ringemann, V. Müller, C. Eggeling, and S. W. Hell. "Red-emitting rhodamine dyes for fluorescence microscopy and nanoscopy." In: *Chemistry – A European Journal* 16.1 (2010). DOI: [10.1002/chem.200902309](https://doi.org/10.1002/chem.200902309) (cited on page 58).
- [42] U. Kubitschek, editor. *Fluorescence microscopy: from principles to biological applications*. Wiley-VCH, 2013 (cited on pages 4, 19, 20, 51).
- [43] F. Lavoie-Cardinal, N. A. Jensen, V. Westphal, A. C. Stiel, A. Chmyrov, J. Bierwagen, I. Testa, S. Jakobs, and S. W. Hell. "Two-color resolt nanoscopy with green and red fluorescent photochromic proteins." In: *ChemPhysChem* 15.4 (2014). DOI: [10.1002/cphc.201301016](https://doi.org/10.1002/cphc.201301016) (cited on page 4).
- [44] M. Leutenegger, R. Rao, R. A. Leitgeb, and T. Lasser. "Fast focus field calculations." In: *Optics express* 14.23 (2006). DOI: [10.1364/OE.14.011277](https://doi.org/10.1364/OE.14.011277) (cited on pages 21, 23, 25, 26, 31, 70).

- [45] S. G. Lipson, H. S. Lipson, and D. S. Tannhauser. *Optik*. Springer-Lehrbuch. Berlin ; Heidelberg [u.a.]: Springer, 1997 (cited on pages 17–19).
- [46] G. Lukinavičius et al. “Fluorogenic probes for live-cell imaging of the cytoskeleton.” In: *Nature Methods* 11.7 (2014). DOI: [10.1038/nmeth.2972](https://doi.org/10.1038/nmeth.2972) (cited on page 5).
- [47] L. Mandel and E. Wolf. *Optical Coherence and Quantum Optics*. Cambridge University Press, 1995 (cited on page 15).
- [48] Y. Maruyama and E. Charbon. “A time-gated 128x128 CMOS SPAD array for on-chip fluorescence detection.” In: *Proc. Intl. Image Sensor Workshop (IISW)*. Hokkaido, Japan, 2011. DOI: [10.1109/transducers.2011.5969324](https://doi.org/10.1109/transducers.2011.5969324) (cited on page 51).
- [49] G. Porter, P. J. Sadkowski, and C. J. Tredwell. “Picosecond rotational diffusion in kinetic and steady state fluorescence spectroscopy.” In: *Chemical Physics Letters* 49.3 (1977). DOI: [10.1016/0009-2614\(77\)87005-X](https://doi.org/10.1016/0009-2614(77)87005-X) (cited on page 50).
- [50] E. H. Rego, L. Shao, J. J. Macklin, L. Winoto, G. A. Johansson, N. Kamps-Hughes, M. W. Davidson, and M. G. L. Gustafsson. “Nonlinear structured-illumination microscopy with a photo-switchable protein reveals cellular structures at 50-nm resolution.” In: *Proceedings of the National Academy of Sciences of the United States of America* 109.3 (2012). DOI: [10.1073/pnas.1107547108](https://doi.org/10.1073/pnas.1107547108) (cited on page 39).
- [51] M. Reuss, J. Engelhardt, and S. W. Hell. “Birefringent device converts a standard scanning microscope into a STED microscope that also maps molecular orientation.” In: *Optics Express* 18.2 (2010). DOI: [10.1364/OE.18.001049](https://doi.org/10.1364/OE.18.001049) (cited on pages 50, 54).
- [52] B. Richards and E. Wolf. “Electromagnetic diffraction in optical systems. II. Structure of the image field in an aplanatic system.” In: *Proceedings of the Royal Society of London. Series A. Mathematical and Physical Sciences* 253.1274 (1959) (cited on page 31).
- [53] M. J. Rust, M. Bates, and X. Zhuang. “Sub-diffraction-limit imaging by stochastic optical reconstruction microscopy (STORM).” In: *Nature Methods* 3.10 (2006). DOI: [10.1038/nmeth929](https://doi.org/10.1038/nmeth929) (cited on pages 1, 3).
- [54] J. Schneider, J. Zahn, M. Maglione, S. J. Sigrist, J. Marquard, J. Chojnacki, H.-G. Kräusslich, S. J. Sahl, J. Engelhardt, and S. W. Hell. “Ultrafast, temporally stochastic STED nanoscopy of millisecond dynamics.” In: *Nature Methods* 12.9 (2015). DOI: [10.1038/nmeth.3481](https://doi.org/10.1038/nmeth.3481) (cited on page 4).
- [55] S. Schnorrenberg, T. Grotjohann, G. Vorbrüggen, A. Herzig, S. W. Hell, and S. Jakobs. “In vivo super-resolution RESOLFT microscopy of *Drosophila melanogaster*.” In: *eLife* 5 (2016). DOI: [10.7554/eLife.15567](https://doi.org/10.7554/eLife.15567) (cited on page 5).

- [56] C. E. Shannon. "Communication in the Presence of Noise." In: *Proceedings of the IRE* 37.1 (1949). DOI: [10.1109/JRPROC.1949.232969](https://doi.org/10.1109/JRPROC.1949.232969) (cited on page 51).
- [57] A. Sommerfeld and A. J. W. Sommerfeld. *Vorlesungen über Theoretische Physik: Optik*. 3rd edition. Volume IV. Leipzig: Akademische Verlagsgesellschaft Geest & Portig, 1964 (cited on page 15).
- [58] R. E. Thompson, D. R. Larson, and W. W. Webb. "Precise nanometer localization analysis for individual fluorescent probes." In: *Biophysical Journal* 82.5 (2002). DOI: [10.1016/S0006-3495\(02\)75618-X](https://doi.org/10.1016/S0006-3495(02)75618-X) (cited on page 4).
- [59] G. Vicidomini, A. Schönle, H. Ta, K. Y. Han, G. Moneron, C. Eggeling, and S. W. Hell. "Sted nanoscopy with time-gated detection: theoretical and experimental aspects." In: *PLoS ONE* 8.1 (2013). DOI: [10.1371/journal.pone.0054421](https://doi.org/10.1371/journal.pone.0054421) (cited on page 51).
- [60] V. Westphal and S. W. Hell. "Nanoscale resolution in the focal plane of an optical microscope." In: *Physical Review Letters* 94.14 (2005). DOI: [10.1103/physrevlett.94.143903](https://doi.org/10.1103/physrevlett.94.143903) (cited on page 31).
- [61] V. Westphal, S. O. Rizzoli, M. A. Lauterbach, D. Kamin, R. Jahn, and S. W. Hell. "Video-rate far-field optical nanoscopy dissects synaptic vesicle movement." In: *Science* 320.5873 (2008). DOI: [10.1126/science.1154228](https://doi.org/10.1126/science.1154228) (cited on pages 4, 5).
- [62] H. Weyl. "Ausbreitung elektromagnetischer Wellen über einem ebenen Leiter." In: *Annalen der Physik* 365.21 (1919). DOI: [10.1002/andp.19193652104](https://doi.org/10.1002/andp.19193652104) (cited on page 15).
- [63] E. Wolf. "Electromagnetic diffraction in optical systems. I. An integral representation of the image field." In: *Proceedings of the Royal Society of London. Series A. Mathematical and Physical Sciences* 253.1274 (1959). DOI: [10.1098/rspa.1959.0199](https://doi.org/10.1098/rspa.1959.0199) (cited on page 31).
- [64] E. Wolf and Y. Li. "Conditions for the validity of the Debye integral representation of focused fields." In: *Optics Communications* 39.4 (1981). DOI: [10.1016/0030-4018\(81\)90107-3](https://doi.org/10.1016/0030-4018(81)90107-3) (cited on page 25).
- [65] C. A. Wurm et al. "Novel red fluorophores with superior performance in STED microscopy." In: *Optical Nanoscopy* 1.1 (2012). DOI: [10.1186/2192-2853-1-7](https://doi.org/10.1186/2192-2853-1-7) (cited on page 5).
- [66] B. Yang, F. Przybilla, M. Mestre, J.-B. Trebbia, and B. Lounis. "Large parallelization of STED nanoscopy using optical lattices." In: *Optics Express* 22.5 (2014). DOI: [10.1364/OE.22.005581](https://doi.org/10.1364/OE.22.005581) (cited on pages 5, 33, 39, 50, 61).

## ACKNOWLEDGMENTS

---

It is an honor to express my gratitude to all the people who supported me during my time as a PhD student. After all, scientific progress is nourished by numerous collaborations and fruitful exchange.

First and foremost, I want to thank my thesis advisor Prof. Stefan Hell. You gave me the opportunity, the guidance and the freedom to successfully pursue my academic interests on a newly emerging topic in the exciting field of superresolution microscopy. Likewise, my gratitude goes to my thesis advisory committee members Profs. Wolfgang Petrich, Amir Abdollahi and Stefan Hell for providing input and feedback to my advances over the course of the my PhD project. Furthermore, I cordially thank the members of my examination committee Profs. Selim Jochim, Ulrich Schwarz, Rainer Fink and Stefan Hell. In particular, I want to mention Prof. Rainer Fink for agreeing without hesitation to examine my thesis as the second referee.

*Senior academic  
guidance and  
evaluation*

I want to thank and acknowledge all colleagues who contributed to the publication [6] covering the first part of my thesis. The detailed contributions are listed in Appendix A. Beyond that, I want to thank Lucas Alber. As a PhD student in the Max Planck Institute for the Science of Light (MPL), he kindly provided the diffractive optical element, which allowed me to come up with a considerably simplified and improved redesign of the parallelized STED implementation that was described in Chapter 7. Irina Harder from the MPL optimized the DOE design and also produced it. Thank you very much! For the preparation of test-samples and for advice regarding biology, I want to thank Ellen Rothermel, Jessica Matthias, Janina Hanne, Frauke Mücksch and Tatiana Sergeeva.

*Academic  
contributions*

I am grateful for insightful correspondence with Prof. Karl-Heinz Brenner about the theory of wave propagation, with Marcel Leutenegger about special characteristic and calculation of high-NA focus fields as well as TIRF modalities, with Joachim Fischer about stratified media focus field calculations and many more topics, with Prof. Annette Kopp-Schneider and Tim Holland-Letz about parameter estimation statistics, with Jörg Meinertz about the theory of diffractive gratings and with Sara Abrahamsson about the design and the production of high-efficiency DOEs.

*Academic  
correspondence*

I am highly indebted for proofreading parts of my thesis: David Schnörr, Marcel Leutenegger, Jörg Meinertz, Mitja Kleider, Jessica Matthias, Stefanie Glos, Joachim Fischer, Matthias Henrich, Jonas Marquard, Janina Hanne, Franziska Hentzschel, Johann Engelhardt and Björn Matthias. I appreciate every minute of your efforts that improved my writing considerably. My special thanks in this regard go

*Proofreading*

to David: very patiently, you helped me improve my scientific writing style, and you read it *all!*

*Colleagues* I would like to thank my colleagues at the lab: Jasmin, Jale, Dörte, Franziska, Lucas, Janina, Jonas, Patrick, Matthias, Simon, Frederick, Henning, Tobias, Melanie, Julia, Joachim, Jessica, Rifka, Frank and many more. You made my stint very worthwhile, on an academic as well as on a personal level. This section would be incomplete without expressing my greatest respects to Johann Engelhardt: Your positive attitude, together with your hands-on skills, knowledge and joy concerning the miraculous – as well as the rather profane – aspects of scientific work was a huge source of inspiration for me.

*Colleagues at MPI  
BPC* I appreciate the fruitful exchange with my colleagues from the Max Planck Institute for Biophysical Chemistry in Göttingen. Besides pleasant skiing sessions, karaoke, snowball fights, pingpong and table-top soccer matches, I also want to express my gratitude for very helpful academic discussions and for advice from (not exhaustively) the following people: Steffen, Fabian, Francisco, Marcel, Jan, Volker, Jennifer, Silvia, Ulrike and Elisa.

*Team Assistants* I would like to thank the team assistants Stefanie Kruse, Sara Leonarakis and Alena Stephan for taking care of all administrative tasks in a very friendly, competent and prompt manner.

*Workshop* Wolfram Stroh, Rüdiger Schmidt, Tobias Wipfler and many other helpful and skilled staff-members of the DKFZ mechanical workshop: thank you! Likewise, I would like to thank Wolfgang Kluge and the MPI BPC optics workshop. My thanks go furthermore to Armin Runz (DKFZ) for letting me use the 3d printer.

*Mens sana in  
corpore sano* This thesis would not have been possible without the *AG Hell body-weight workout squad*. Among countless occasional participants, I want to express my sincere recognition to Matthias, Franziska and Jessica, who dared to work out with me on a regular basis.

*Family* Finally, I want to express my deepest gratitude to my parents Norbert and Doris Bergermann as well as to my girlfriend Franziska Hentzschel: I am so grateful for your unlimited support, your enjoyable company and your unconditional love.